Universität Hamburg
DER FORSCHUNG | DER LEHRE | DER BILDUNG

FAKULTÄT
FÜR MATHEMATIK, INFORMATIK
UND NATURWISSENSCHAFTEN

DISSERTATION

First Principles Approach for Optical Excitations in Transition Metal Dichalcogenides

Carl Emil Mørch Nielsen

A.G. Bester
Fachbereich Physik
Fakultät für Mathematik, Informatik und Naturwissenschaften

Universität Hamburg
Hamburg, Deutschland
2025

Dissertation zur Erlangung des Doktorgrades

Doctor rerum naturalium (Dr. rer. nat.)

First Principles Approach for Optical Excitations in Transition Metal Dichalcogenides

Dissertation abgegeben von: Carl Emil Mørch Nielsen

Datum der Abgabe: 15.10.2025
Datum der Disputation: 11.12.2025

Supervisor: Prof. Dr. Gabriel Bester

Gutachter/innen der Dissertation:	Prof. Dr. Gabriel Bester Prof. Dr. Tim Wehling
Zusammensetzung der Prüfungskommission:	Prof. Dr. Gabriel Bester Prof. Dr. Tim Wehling Dr. Marta Prada Prof. Dr. Robert Blick Prof. Dr. Dorota Koziej
Vorsitzende/r der Prüfungskommission:	Prof. Dr. Dorota Koziej
Vorsitzender des Fach-Promotionsausschusses PHYSIK:	Prof. Dr. Wolfgang J. Parak
Leiter des Fachbereichs PHYSIK:	Prof. Dr. Markus Drescher
Dekan der Fakultät MIN:	Prof. Dr.-Ing. Norbert Ritter

Universität Hamburg, Hamburg, Deutschland
Fakultät für Mathematik, Informatik und Naturwissenschaften
Fachbereich Physik

A.G. Bester

Affidavit

Hiermit versichere ich an Eides statt, die vorliegende Dissertationsschrift selbst verfasst und keine anderen als die angegebenen Hilfsmittel und Quellen benutzt zu haben. Sofern im Zuge der Erstellung der vorliegenden Dissertationsschrift generative Künstliche Intelligenz (gKI) basierte elektronische Hilfsmittel verwendet wurden, versichere ich, dass meine eigene Leistung im Vordergrund stand und dass eine vollständige Dokumentation aller verwendeten Hilfsmittel gemäß der Guten wissenschaftlichen Praxis vorliegt. Ich trage die Verantwortung für eventuell durch die gKI generierte fehlerhafte oder verzerrte Inhalte, fehlerhafte Referenzen, Verstöße gegen das Datenschutz- und Urheberrecht oder Plagiate.

I hereby declare and affirm that this doctoral dissertation is my own work and that I have not used any aids and sources other than those indicated. If electronic resources based on generative artificial intelligence (gAI) were used in the course of writing this dissertation, I confirm that my own work was the main and value-adding contribution and that complete documentation of all resources used is available in accordance with good scientific practice. I am responsible for any erroneous or distorted content, incorrect references, violations of data protection and copyright law or plagiarism that may have been generated by the gAI.

15.10.2025

Datum/Date

Unterschrift/Signature

(Carl Emil Mørch Nielsen)

This work is dedicated to Emma.

Acknowledgements

First and foremost, I would like to thank my supervisor and friend, Prof. Dr. Gabriel Bester, for giving me the opportunity to be part of his group. I have enjoyed my time here immensely, largely due to his pleasant company, scientific expertise and laissez-faire supervision style, which helped me mature as a scientist. Additionally, I would like to thank Dr. Marta Prada for the assistance provided in both writing this thesis and related publications, as well as for the fun yoga lessons offered completely free of charge. For supervising me through the very early stages of my PhD, a special thanks must also be given to Dr. Abderrezak Torche, who spent countless hours helping me develop my first project. Next, I would like to thank the secretary staff over the years, including Wasel Alhawani, Angelina Siemon, and the current, very capable Irene Kopf.

To my colleagues—and now close friends—I would like to extend a special thanks as well. Without you, I would not have been able to reach where I am today. This includes Anne Nadine Tewonoue Djota, Dr. Sumanti Patra, Dr. Surender Kumar and Amanda Damaris Hernández Tzorín. Furthermore, Dr. Yasser Saleem, who was part of the group for a short time, was an immense support, both scientifically and as a dear friend.

Another colleague and close friend deserving special mention is Miguel Morales Cócera, who has been under my supervision and from whom I have learned to question even the smallest scientific details to grasp the big picture. More than that, my colleague Tobias Dittmann has become one of my closest friends over the years, and his unique, kind personality ensures he will always be a friend I cherish.

I would like to extend an especially heartfelt thanks to Franz Fischer. If you had not joined the group in the early stages of my PhD, I might not have been able to continue my journey in Hamburg. You were the first true friend I made here and quickly became one of my most treasured friends. Both socially and scientifically, you have been a pillar—thank you.

Another thanks to my friends Emil, Erik, Mads, Jakob, Nanna, Tim, Fu-My, Adisak, Christian, Mygind, and Lars. Staying in contact with all of you has meant more than you know. Your companionship is always appreciated.

To my family—my mom, dad, and two brothers—I thank you for your support over the years. I would not be who I am today without you.

Lastly, to my biggest supporter, Emma, words cannot express how much your support has meant to me over the years. From staying with me in Hamburg during the COVID years to taking care of me during chemotherapy, you have been there for me every single time. It truly means the world to me. Thank you.

Abstract

This cumulative thesis presents a comprehensive *ab initio* framework for investigating many-body excited states in two-dimensional transition metal dichalcogenides and their heterostructures, combining density functional theory and advanced configuration interaction methods. The developed methodology captures subtle fermion-fermion interactions manifesting as excitonic complexes, enabling highly accurate predictions of optical properties.

The first study focuses on monolayer WSe_2, where many-body screened configuration interaction calculations reveal the existence of negatively charged trions involving the **Q**-valley of the conduction band. These **Q**-valley trions are energetically more favorable than their conventional **K**-valley counterparts and exhibit increased singlet-triplet splittings, providing new insights into valley-dependent optical features consistent with experimental observations.

Building on this, the second investigation examines bilayer Janus transition metal dichalcogenide heterostructures, such as MoSSe–WSSe and WSSe–WSSe. The results show that intrinsic structural asymmetry and interface-induced polarization enable spin-allowed interlayer exciton and trion ground states, contrasting with the spin-forbidden states typical of conventional bilayers. Furthermore, the application of external strain offers additional means to tune the optical brightness and properties of these interlayer states, opening pathways for precise control in optoelectronic applications.

Lastly, more complex heterostructures are investigated, which are constructed by introducing a twist in the loosely van der Waals bound bilayers. To this extent, a generalized force-field relaxation scheme tailored for large moiré heterostructures is developed. By optimized parameterization against first principles calculations, this approach accurately reproduces atomic reconstructions for both commensurate and incommensurate systems, especially at small twist angles. These relaxed structures reveal significant modifications of the interlayer potential landscape, emphasizing the importance of in-plane and out-of-plane atomic displacements on excitonic confinement and localization.

Together, these studies establish a versatile and predictive computational platform for exploring and engineering many-body phenomena in 2D materials. The insights gained into valley physics, interlayer excitonics, and structural relaxation underpin future strategies for designing tailored optoelectronic, valleytronic, and quantum devices based on layered two-dimensional heterostructures.

Zusammenfassung

Diese kumulative Dissertation präsentiert ein umfassendes *ab initio*-Framework zur Untersuchung von Vielteilchen-Anregungszuständen in zweidimensionalen Übergangs-metall-Dichalkogeniden und deren Heterostrukturen, durch Kombination von Dichtefunktionaltheorie und Konfigurationswechselwirkungsmethoden. Die entwickelte Methodik erfasst subtile Fermion-Fermion-Wechselwirkungen, die exzitonartige Komplexe verursachen, und ermöglicht hochpräzise Vorhersagen der optischen Eigenschaften zweidimensionaler Materialien.

Die erste Studie konzentriert sich auf Monolayer WSe_2, wobei die Existenz negativ geladener Trionen gezeigt wird, die das **Q**-Valley des Leitungsbands besetzen. Diese **Q**-Valley-Trionen sind energetisch günstiger als ihre herkömmlichen **K**-Valley-Äquivalente und weisen verstärkte Singlet-Triplet-Aufspaltungen auf, was neue Einblicke in die Valley-abhängigen optischen Eigenschaften dieser Materialklasse liefert.

Darauf aufbauend untersucht die zweite Studie zweilagige Janus-Übergangsmetall-Dichalkogenid-Heterostrukturen, wie MoSSe–WSSe und WSSe–WSSe. Die Ergebnisse zeigen, dass durch die intrinsische strukturelle Asymmetrie und Grenzflächen-induzierte Polarisation die Bildung spin-erlaubter Interlagen-Exzitonen und Trionen im Grundzustand ermöglichen. Im Gegensatz dazu liegen in konventionellen Bilagen spin-verbotene Zustände vor. Darüber hinaus bieten externe Dehnung und Kompression zusätzliche Möglichkeiten, die optische Helligkeit und Eigenschaften dieser Interlagen-Zustände gezielt zu steuern, wodurch eine präzise Kontrolle der Optoelektronik möglich wird.

Abschließend werden komplexere Heterostrukturen untersucht, indem die schwach van-der-Waals gebundenen Bilagen gegeneinander verdreht werden, wodurch ein Moire-Muster entsteht. Zur Untersuchung selbiger Strukturen wurde ein verallgemeinertes Kraftfeld entwickelt, das die optimale Geometrie des Systems findet. Durch optimierte Parameterisierung via ab initio Methoden reproduziert dieser Ansatz die atomare Rekonstruktion insbesondere bei kleinen Drehwinkeln. Diese relaxierten Strukturen zeigen signifikante Veränderungen der Potentiallandschaft zwischen den Schichten, was die Bedeutung von Atomverschiebungen innerhalb der Lage und zwischen beiden Lagen für die Exzitonenlokalisierung unterstreicht.

Gemeinsam bilden diese theoretischen Studien eine vielseitige Plattform zur Erforschung und Steuerung von Vielteilchen-Phänomenen in 2D-Materialien. Die gewonnenen Erkenntnisse zu Valley-Physik, Interlagen-Exzitonen und struktureller Relaxation bilden die Grundlage für zukünftige Strategien zur Gestaltung maßgeschneiderter optoelektronischer, Valleytronik- und Quantengeräten auf Basis von geschichteten zweidimensionalen Heterostrukturen.

Contents

List of Publications

Dissertation Related Publications

[E1] **C. E. Mørch Nielsen, F. Fischer, and G. Bester** Beyond the K-valley: exploring unique trion states in indirect band gap monolayer WSe_2. *npj 2D Mater Appl* **9**, 11 (2025).

[E2] **C. E. Mørch Nielsen, F. Fischer, M. Prada, and G. Bester** From dark to bright: first-principles prediction of ground state excitons and trions in Janus transition metal dichalcogenide bilayers. *2D Mater* **12**, 045015 (2025).

[E3] **C. E. M. Nielsen, M. da Cruz, A. Torche, and G. Bester** Accurate force-field methodology capturing atomic reconstructions in transition metal dichalcogenide moiré system. *Phys. Rev. B* **108**, 045402 (2023).

Other Publications

[E4] **F. Fischer, C. E. M. Nielsen, M. Prada, and G. Bester** Unconventional bright ground-state excitons in monolayer TiI_2 from first-principles calculations. *npj 2D Mater Appl* **(submitted, draft on arXiv)** (2025).

List of Figures

List of Abbreviations

2D, 3D	Two- or three-dimensional
BSE	Bethe-Salpeter Equation
BZ	Brilloiun Zone
CBM	Condunction Band Minimum
CI	Configuration Interaction
CIS	Configuration Interaction Singles
CID	Configuration Interaction Doubles
CISD	Configuration Interaction Singles and Doubles
DFT	Density-Functional theory
ED	Excited Slater Determinant
FFT	Fast Fourier Transform
GGA	Generalized Gradient Approximation
IBZ	Irreducible Brillouin Zone
LDA	Local Density Approximation
PBE	Exchange-correlation functional parametrization of Perdew, Burke and Ernzerhof
QE	Quantum ESPRESSO
RIM	Random Integration Method
TMD	Transition Metal Dichalcogenide
VBM	Valence Band Maximum
vdW	Van der Waals

1 Introduction

Two-dimensional (2D) materials have revolutionized the landscape of modern condensed matter physics, opening pathways to a new era of electronic, photonic, and quantum technologies. Extending periodically along two spatial dimensions but not in the third, these atomically thin layers possess extraordinary properties that challenge our understanding of matter itself. Over the past few decades, the field of 2D materials has garnered immense scientific interest, a momentum that largely began with the groundbreaking isolation of graphene — the first truly atomically thin material — using nothing more than tape and a labor of ingenuity [1]. Later, this technique was extended to transition metal dichalcogenides (TMDs), specifically MoS_2 [2], which as opposed to the semimetallic graphene monolayer, features a sizable direct bandgap, broken inversion symmetry, and strong valence band spin-orbit coupling effects in the single layer limit [3, 4].

Pioneering research has uncovered the unique potential of TMDs reflected in their remarkable flexibility [5], large exciton binding energies [6, 7] and potential for valley polarized phenomena [8–10]. These properties make TMD monolayers prime candidates for the next generation of ultra-efficient transistors [11–14], electrochemical sensors [15–17], thin-film dry lubricants [18, 19], photodetectors [20–22], etc., and fuels ongoing research to identify and develop the underlying fundamental physics.

While the potential of monolayer TMDs continues to inspire numerous research directions, the story becomes truly fascinating when these monolayers are combined either laterally [23–27] via chemical bonds or vertically through van der Waals (vdW) forces into heterostructures [28, 29]. This flexibility in synthesis allows researches to study and design materials with system-specific properties, such as tunable bandgaps [30–32], long lived interlayer excitons [33, 34], ultra-high carrier mobility [35], etc. Vertically stacked bilayer heterostructures with a relative twist — known as moiré heterostructures — have been shown to host nearly flat electronic bands [36–38], opening pathways to emergent phenomena such as correlated states and unconventional superconductivity [39–41]. Yet, unlocking these properties requires a deep understanding of many-body interactions, spin-valley physics, and the complex interplay of structural, electronic, and optical effects.

TMDs have the chemical composition MX_2, consisting of a transition metal, $M \in \{Mo, W\}$, and two chalcogens, $X \in \{S, Se\}$, in the primitive cell. Typically, they crystallize in the stable 1H-phase forming a honeycomb-like atomic structure of exceptional mechanical strength [42], shown in Fig. 1.1(a,b). Consequently, the

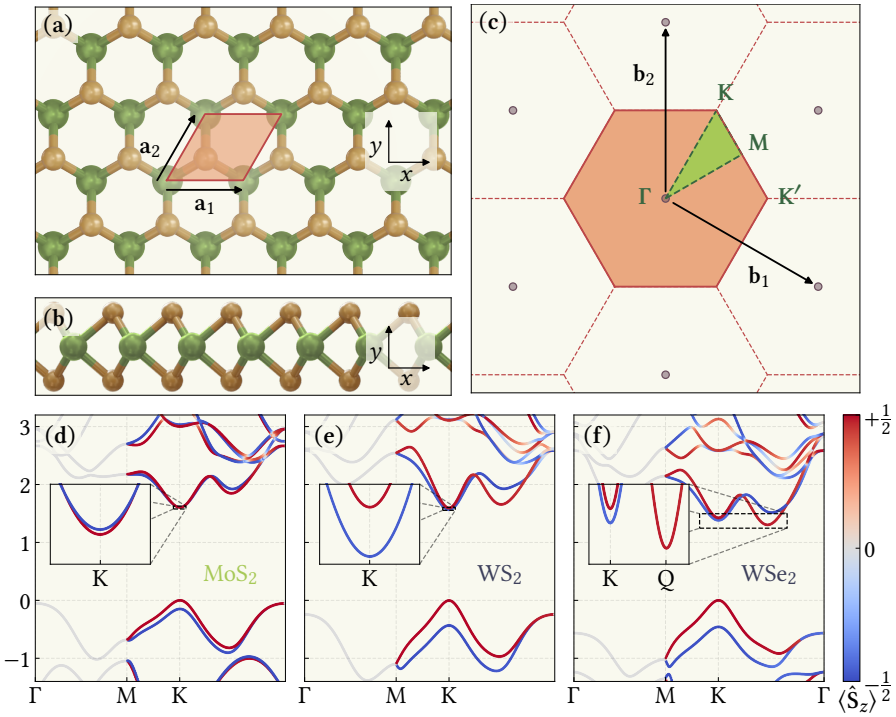

Figure 1.1: (a) Topdown view of MX_2 with the primitive cell depicted in orange and corresponding primitive vectors, $\mathbf{a}_1$ and $\mathbf{a}_2$. Green spheres represent the metals, M, while beige spheres represent the chalgogens, X. (b) Sideview. (c) The first Brillouin zone depicted in orange. The reciprocal lattice and the primitive reciprocal vectors, $\mathbf{b}_1$ and $\mathbf{b}_2$, are presented in dark purple. Lastly, the high-symmetry points of the Brillouin zone are marked in green, as well as the irreducible Brillouin zone. (d) The band structure of MoS_2 at the PBE level. The spin texture is encoded in the color of the bands, where red denotes spin up and blue spin down. The inset show the energetic ordering near the conduction band minimum. (e) Same as (d), but for WS_2. (f) Same as (d), but for WSe_2.

reciprocal lattice vectors span a hexagonal Brillouin zone, which is depicted in Fig. 1.1(c) along with the high-symmetry points. As exemplified in Fig. 1.1(d,e,f) for MoS_2, WS_2 and WSe_2, the monolayer TMDs posses a direct, sizable bandgap at the **K**-point (except in the case of WSe_2 [43, 44]), and exhibit polarized spin-split bands, which allows for well-defined many-body fine structures, thus making TMDs especially suitable for optoelectronic applications.

To this extent, this thesis aims to systematically enhance the theoretical understanding of advanced many-body effects in TMDs with an emphasis on optical properties. To illuminate these intricate physics, an *ab initio* many-body approach based on configuration interaction in the electron-hole formalism has been developed for 2D materials, inspired by previous works [45–47]. The first two chapters, namely Chapter 2 and Chapter 3, are dedicated to introducing the theoretical background and its implementation. This powerful, many-body approach captures the subtle correlations that govern excitons, trions, and more complex compounds in 2D materials.

The results (Chapter 4) are structured in three separate parts going from monolayer to bilayer, and finally to the complex moiré heterostructures. As this thesis is cumulative, the results consist of publications from peer-reviewed magazines preceded by a relevant introduction to the subject matter. The journey begins with an in-depth exploration of excitonic physics in monolayer WSe_2 [E1], which establishes a detailed picture of bound many-body states including their binding energies, fine-structure splitting, and oscillator strengths. By analyzing the excitonic states in the single layer a priori, the stage is set for understanding how more complex structures influence the excited states.

Progressing further, this analysis is extended to bilayer heterostructures, specifically the Janus-structured MoSSe-WSSe system [E2], where interlayer excitons and trions form across the bilayer interface. Stacking configurations, interfacial alignment and interlayer coupling modify the oscillator strengths, spin configurations, and energetic ordering of the excitonic complexes. Specifically, it is revealed that the asymmetry in the Janus structure can enable spin-allowed ground states that were traditionally considered optically dark in regular TMD heterostructures, opening avenues for designing efficient quantum light sources and valleytronic devices.

Finally, the intriguing structural optimization effects in moiré heterostructures [E3] are explored, which are formed by stacking two monolayers with a relative twist angle or lattice mismatch. Through the parametrization of established force-fields [48–51] based on *ab initio* calculations, a model is developed to accurately capture crucial relaxation effects. An example is the in-plane atomic reconstructions, which significantly alter the potential landscapes of such systems. This part of the thesis lays the groundwork for future theoretical endeavors into the many-body effects of moiré heterostructures.

The goal of this work is to provide a comprehensive, predictive understanding of structural, spin, and many-body effects in 2D materials. This research not only clarifies fundamental physics but also pushes the boundaries toward practical applications—be it valleytronics, quantum information, or next-generation opto-electronic devices—by enabling precise control over excitonic and electronic states.

By advancing computational tools and broadening our understanding, the hope is that this work catalyzes new technological breakthroughs and inspires future explorations into the captivating physics of 2D quantum materials.

2
Theory

This chapter presents key theoretical concepts in electronic structure calculations, starting from the many-body Hamiltonian in the Born-Oppenheimer approximation. From here, the theory and concepts behind density-functional theory (DFT) are introduced - a powerful tool that describes the electron structure of complex systems such as molecules and solids through the electron density. Extending beyond DFT, the chapter explores configuration interaction (CI) in the electron-hole picture - a highly accurate, yet numerically demanding, method for modeling many-body excited states and energies. To mitigate the complexity of CI, the chapter concludes with a brief discussion on how to truncate the CI basis by restricting it to specific excitation subspaces.

Contents

2.1 The Many-body Hamiltonian

The starting point for access to the electronic structure of atoms, molecules and solids is the many-body Hamiltonian, $\widehat{\mathcal{H}}_{\text{MB}}$. For a system of electrons and nuclei interacting through Coulomb forces, $\widehat{\mathcal{H}}_{\text{MB}}$ can (disregarding spin terms), in atomic units, be described as

$$\widehat{\mathcal{H}}_{\text{MB}} = -\sum_{A} \frac{1}{2M_A}\nabla_A^2 + \frac{1}{2}\sum_{A\neq B}\frac{Z_A Z_B}{r_{AB}} - \sum_{i}\frac{1}{2}\nabla_i^2 + \frac{1}{2}\sum_{i\neq j}\frac{1}{r_{ij}} - \sum_{i,A}\frac{Z_A}{r_{iA}}, \tag{2.1}$$

where A, B are nuclear indices, and i, j the electronic analogues. Moreover, M_A denotes the mass of nucleus A in units of the electron mass, and likewise, Z_A is the charge of nucleus A in units of the electron charge, e. For brevity, the notation $r_{12} = |r_1 - r_2|$ has been used. Lastly, the double sums of the second and fourth term are restricted to avoid self-interaction, while the factor $\frac{1}{2}$ accounts for double counting.

The first and third terms of Eq. (2.1) describe the kinetic energy of the nuclei and electrons, respectively, whereas the second and fourth terms represent the repulsive nucleus-nucleus and electron-electron interactions, respectively, and, finally, the last term describes the attractive nucleus-electron interaction. From here, the full many-body Schrödinger equation reads

$$\widehat{\mathcal{H}}_{\mathrm{MB}}\Psi_{\mathrm{MB}}(r,R) = E_{\mathrm{MB}}\Psi_{\mathrm{MB}}(r,R), \tag{2.2}$$

where r encompasses all electronic coordinates, and R all nuclear ones. The eigenstates $\Psi_{\mathrm{MB}}(r,R)$ are the many-body wavefunctions with corresponding energies E_{MB}.

As a first step to reducing the infeasible task of solving Eq. (2.2), M. Born and J. R. Oppenheimer proposed an approach [52]. Since the masses of the electrons are much smaller than those of the nuclei, the electronic motion adjusts almost instantaneously to the nuclear one. The adiabatic response of the electron to the ions allow the eigenstates to be of the form

$$\Psi_{\mathrm{MB}}(r,R) = \Psi_{\mathrm{e}}(r;R)\Psi_{\mathrm{n}}(R). \tag{2.3}$$

The ionic part of the wavefunction, $\Psi_{\mathrm{n}}(R)$, depends only on the coordinates of the nuclei, while the electronic wavefunction, $\Psi_{\mathrm{e}}(r;R)$, assumes a static ionic geometry. For any such frozen geometry, Eq. (2.3) suggests that Ψ_{e} are eigenstates of an electronic Hamiltonian akin to that of Eq. (2.1) but disregarding the first two (ionic) terms, namely

$$\widehat{\mathcal{H}}_{\mathrm{e}} = -\sum_i \frac{1}{2}\nabla_i^2 + \frac{1}{2}\sum_{i\neq j}\frac{1}{r_{ij}} - \sum_{i,A}\frac{Z_A}{r_{iA}}, \tag{2.4}$$

with the corresponding electronic Schrödinger equation

$$\widehat{\mathcal{H}}_{\mathrm{e}}\Psi_{\mathrm{e}}(r;R) = E(R)\Psi_{\mathrm{e}}(r;R), \tag{2.5}$$

which in principle can be solved for any configuration of ionic coordinates, R. While the Born-Oppenheimer approximation significantly reduces the difficulty of Eq. (2.2), the task of solving Eq. (2.5) exactly remains numerically impossible. Over the years, numerous approaches have been proposed to address this challenge, with DFT emerging as the most widely used today.

2.2 Density-functional Theory

The fundamental difference between DFT and other methods is the suspension of the wavefunction, $\Psi_{\mathrm{e}}(r)$, as the central quantity. Rather, as implied by the

name, the focus of DFT is the electron density, $\rho(\mathbf{r})$, with corresponding operator $\hat{\rho}(\mathbf{r}) = \sum_i \delta(\mathbf{r} - \mathbf{r}_i)$. Disregarding spin, the electron density is then

$$\rho(\mathbf{r}) = N \int |\Psi_\mathrm{e}(\mathbf{r}, \mathbf{r}_2, \ldots, \mathbf{r}_N)|^2 \, \mathrm{d}\mathbf{r}_2 \ldots \mathrm{d}\mathbf{r}_N, \tag{2.6}$$

which essentially relies on only three spatial coordinates, in contrast to the $3N$ coordinates of all electrons in the system. First, Eq. (2.4) can be rewritten as

$$\hat{\mathcal{H}}_\mathrm{e} = -\sum_i \frac{1}{2}\nabla_i^2 + \frac{1}{2}\sum_{i \neq j} \frac{1}{r_{ij}} + \sum_i v_\mathrm{ext}(\mathbf{r}_i), \tag{2.7}$$

where the external potential, v_ext, represents the electron-nuclei interaction and potentially an external electric field. In a groundbreaking manner, P. Hohenberg and W. Kohn [53] proved that v_ext, and, in extension, the total energy, is a unique functional of the electron density, of which the latter can be written as[1]

$$E[\rho] = T_e[\rho] + U_{ee}[\rho] + U_\mathrm{ext}[\rho]. \tag{2.8}$$

Here, the functional T_e describes the kinetic energy of the electrons, U_ext the potential energy from the external sources, and U_{ee} the potential energy from the Coulomb electron-electron interactions. Moreover, as an extension of the variational principle, Hohenberg and Kohn [53] showed that $E[\rho]$ corresponds to the ground state energy of the system if and only if ρ is the ground state density, ρ_0. It is, however, unclear how to determine the functional form of T_e and U_{ee}. To this extent, W. Kohn and L. J. Sham [55] suggested a more practical approach. First, $T_e[\rho]$ in Eq. (2.8) can be decomposed into the classical non-interacting kinetic energy, plus a subtle correction capturing the fact that real systems have interacting electrons. Similarly, $U_{ee}[\rho]$ is represented as the classical, self-interacting Hartree term accompanied by a two-electron exchange-correlation term accounting for electron-electron correlations beyond the mean-field. In both cases, the non-classical terms reflect the quantum-mechanical nature of electrons and are collected into a new term, E_{xc}, called the exchange-correlation energy. In other words,

$$\begin{aligned} E[\rho] = &-\frac{1}{2}\sum_i \int \varphi_i^*(\mathbf{r})\nabla^2\varphi_i(\mathbf{r}) \, \mathrm{d}\mathbf{r} + \frac{1}{2}\int \frac{\rho(\mathbf{r}_1)\rho(\mathbf{r}_2)}{r_{12}} \, \mathrm{d}\mathbf{r}_1 \, \mathrm{d}\mathbf{r}_2 \\ &+ \int v_\mathrm{ext}(\mathbf{r})\rho(\mathbf{r}) \, \mathrm{d}\mathbf{r} + E_{xc}[\rho], \end{aligned} \tag{2.9}$$

where φ_i are called the Kohn-Sham orbitals and form an orthonormal set, i.e. $\langle\varphi_i|\varphi_j\rangle = \delta_{ij}$. In this context, the index i uniquely specifies all the quantum numbers of the orbitals. Furthermore, the one-electron density is calculated as $\rho(\mathbf{r}) = \sum_i \varphi_i^*(\mathbf{r})\varphi_i(\mathbf{r})$ and is assumed exact. Following the variational principle, $E[\rho]$ can be varied around the exact ρ and set equal to zero, which leads to an equation of the form

$$\left\{-\frac{1}{2}\nabla^2 + v_C(\mathbf{r}) + v_\mathrm{ext}(\mathbf{r}) + v_{xc}(\mathbf{r})\right\}\varphi_i(\mathbf{r}) = \epsilon_i\varphi_i(\mathbf{r}). \tag{2.10}$$

[1] The following derivation is loosely based on Ref. [54].

Here, the Hartree potential, v_C, is simply

$$v_C(\mathbf{r}_1) = \int \frac{\rho(\mathbf{r}_2)}{r_{12}} \, \mathrm{d}\mathbf{r}_2, \tag{2.11}$$

which corresponds to the potential of a point charge at $\mathbf{r}_1$ interacting with the charge density, $\rho(\mathbf{r}_2)$. The exchange-correlation potential, v_{xc}, can only be expressed as the functional derivative of E_{xc}, since the true form of E_{xc} is unknown. Formally,

$$v_{xc}(\mathbf{r}) = \frac{\delta E_{xc}[\rho]}{\delta \rho(\mathbf{r})}. \tag{2.12}$$

Eq. (2.10) are known as the Kohn-Sham equations, and the ground-state solutions are exact given that v_{xc} is exact. Moreover, all the potentials of Eq. (2.10) are local, which in itself is an advantage over similar methods such as Hartree-Fock [56–58]. The Kohn-Sham equations are solved in a self-consistent manner starting from an initial guess of $\rho(\mathbf{r})$, which is used to compute the potentials, and thus solve Eq. (2.10) for $\varphi_i(\mathbf{r})$. The Kohn-Sham wavefunctions are then used to compute a new density, and the procedure starts again, which is repeated until convergence is reached.

To consolidate the unknown form of the exchange-correlation potential in Eq. (2.12), several suggestions for approximations have been made over the years, and are often constructed using a combination of $\rho(\mathbf{r})$ and various powers of its derivative. The two most widely used of these are the local density approximation (LDA) [55] and the generalized gradient approximation (GGA) [59], of which the latter is used extensively throughout this work. The LDA assumes the electron density to resemble that of a nearly homogeneous electron gas, and represents the simplest possible description. In such an approximation lies the assumption that the density does not vary significantly in space, as for example in the case of metals. Going one step up "Jacob's ladder" [59], the GGA tries to improve by including $\nabla\rho(\mathbf{r})$, thus increasing the accuracy of the exchange-correlation potential. Moreover, different flavors of the GGA exists, with the most popular being the parametrization of Perdew, Burke and Ernzerhof (PBE) [60]. Finally, going even higher up on the ladder, are approximations such as meta-GGA and hybrid functionals, which are beyond the scope of this work.

2.3 Configuration Interaction

The preceding section has dealt with the ground state electronic properties, since those are the focus of the Hohenberg-Kohn theorems. At the same time, the ultimate goal of DFT is procuring the Kohn-Sham eigenvalues and wavefunctions, which are inherently single-particle states. To go one step further and address the many-body wavefunctions of excited states, further refinement is needed. To this extent, CI proves particularly useful. Consider again the many-body electronic Hamiltonian for N interacting fermions, seen in Eq. (2.7), namely

$$\widehat{\mathcal{H}} = \sum_i \left(-\frac{1}{2}\nabla_i^2 + v_{\text{ext}}(\mathbf{r}_i) \right) + \frac{1}{2} \sum_{i \neq j} \frac{1}{r_{ij}}. \tag{2.13}$$

From here, a single-particle mean-field interaction can be introduced through the potential, $v_{\mathrm{MF}}(\mathbf{r})$, such that

$$\left(-\frac{1}{2}\nabla_i^2 + v_{\mathrm{ext}}(\mathbf{r}_i) + v_{\mathrm{MF}}(\mathbf{r}_i) \right) \varphi_i(\mathbf{r}) = \hat{h}_i \varphi_i(\mathbf{r}) = \epsilon_i \varphi_i(\mathbf{r}), \tag{2.14}$$

where $\hat{h}_i$ denotes the single-particle Hamiltonian, while ϵ_i and φ_i are the single-particle eigenvalues and wavefunctions, respectively, typically obtained through the Kohn-Sham equations. Using Eq. (2.14) allows for rewriting $\widehat{\mathcal{H}}$ to

$$\widehat{\mathcal{H}} = \sum_i \hat{h}_i - \sum_i v_{\mathrm{MF}}(\mathbf{r}_i) + \frac{1}{2} \sum_{i \neq j} \frac{1}{r_{ij}}. \tag{2.15}$$

From here, $\widehat{\mathcal{H}}$ can be expressed in second quantization using the aforementioned single-particle states, $|i\rangle = \varphi_i(\mathbf{r}_i)$. Formally,

$$\widehat{\mathcal{H}} = \sum_i \epsilon_i \hat{c}_i^\dagger \hat{c}_i - \sum_{ij} \langle i | \, v_{\mathrm{MF}} \, | j \rangle \, \hat{c}_i^\dagger \hat{c}_j + \frac{1}{2} \sum_{ijkl} \langle ij | \, v \, | kl \rangle \, \hat{c}_i^\dagger \hat{c}_j^\dagger \hat{c}_l \hat{c}_k, \tag{2.16}$$

where $v = v(\mathbf{r}_1, \mathbf{r}_2) = 1/r_{12}$ is the Coulomb potential, and $\hat{c}^\dagger$ and $\hat{c}$ are the fermionic creation and annihilation operators, respectively. These operators satisfy the usual fermionic (anti) commutation relations, namely

$$[\hat{c}_i, \hat{c}_j^\dagger]_+ = \delta_{ij}, \quad \hat{c}_i \, |\Omega\rangle = 0, \quad \hat{c}_i^\dagger \, |\Omega\rangle = |i\rangle \, . \tag{2.17}$$

Here, $|\Omega\rangle$ denotes the vacuum state of the system, i.e. the (many-body) quantum state with the lowest possible energy.

2.3.1 The Electron-hole Picture

In the single-particle picture, i.e. neglecting the last two terms of Eq. (2.16), the ground state has the lowest N states occupied. Assuming this to be a non-degenerate state allows for defining the Fermi level and a corresponding state index n_f. Then, all states below or equal to n_f are occupied and all above are empty. In the occupation number formalism of second quantization, this state can be described as

$$|\Omega\rangle = |\underbrace{1, \ldots, 1}_{n_f}, 0, \ldots\rangle \tag{2.18}$$

From here, a canonical transformation to an electron-hole picture can be performed, and in this new picture, all states below n_f are now empty (with respect to holes), while all above remain empty too (with respect to electrons). This state then serves as the vacuum state of the new formalism. In extension, the electron creation and annihilation operators, $\hat{a}_i^\dagger$ and $\hat{a}_i$, respectively, can be defined such that

$$\hat{a}_i^\dagger = \hat{c}_i^\dagger, \quad \hat{a}_i = \hat{c}_i. \tag{2.19}$$

Similarly, the corresponding hole operators are given as

$$\hat{b}_\alpha^\dagger = \hat{c}_\alpha, \quad \hat{b}_\alpha = \hat{c}_\alpha^\dagger. \tag{2.20}$$

Notice here the distinction between electron states indicated by Latin letters and hole states by Greek letters. It is trivial that $|\Omega\rangle$ from Eq. (2.18) indeed serves as the vacuum state of the electron-hole picture, since

$$\hat{a}_i |\Omega\rangle = 0, \quad \hat{b}_\alpha |\Omega\rangle = 0, \quad \alpha \leq n_f < i. \tag{2.21}$$

Moreover, the usual fermionic commutation relations hold true for both the electron and hole operators in their own subspace, that is

$$[\hat{a}_i, \hat{a}_j^\dagger]_+ = \delta_{ij}, \quad [\hat{b}_\alpha, \hat{b}_\beta^\dagger]_+ = \delta_{\alpha\beta}. \tag{2.22}$$

However, the electron and hole operators commute with one another. Formally

$$[\hat{a}_i, \hat{b}_\alpha]_+ = [\hat{a}_i, \hat{b}_\alpha^\dagger]_+ = [\hat{a}_i^\dagger, \hat{b}_\alpha]_+ = [\hat{a}_i^\dagger, \hat{b}_\alpha^\dagger]_+ = 0. \tag{2.23}$$

As demonstrated in the following section, the introduction of the new formalism vastly complicates the expression of the many-body Hamiltonian seen in Eq. (2.16). This complexity is, however, more than compensated for by the advantages offered by the electron and hole subspaces, which naturally lend themselves to the description of excited states — where electrons are promoted beyond the Fermi level, leaving behind holes below.

2.3.2 The Electron-hole Hamiltonian

The following procedure consists of splitting each sum of Eq. (2.16) in two, one for all states $\leq n_f$ (holes) and one for all states $> n_f$ (electrons). Clearly, this results in a lot of terms, especially for the last term, which features a quadruple sum. To provide a clearer perspective, the first term describing the independent particles, can be denoted $\widehat{\mathcal{H}}_{\text{IP}}$, the second term $\widehat{\mathcal{H}}_{\text{MF}}$, and the last term $\widehat{\mathcal{H}}_{\text{C}}$. Formally,

$$\widehat{\mathcal{H}}_{\text{IP}} := \sum_i \epsilon_i \hat{c}_i^\dagger \hat{c}_i, \quad \widehat{\mathcal{H}}_{\text{MF}} := \sum_{ij} \langle i| v_{\text{MF}} |j\rangle \, \hat{c}_i^\dagger \hat{c}_j, \quad \widehat{\mathcal{H}}_{\text{C}} := \sum_{ijkl} \langle ij| v |kl\rangle \, \hat{c}_i^\dagger \hat{c}_j^\dagger \hat{c}_l \hat{c}_k. \tag{2.24}$$

Then, $\widehat{\mathcal{H}}$ can be written simply as

$$\widehat{\mathcal{H}} = \widehat{\mathcal{H}}_{\text{IP}} - \widehat{\mathcal{H}}_{\text{MF}} + \frac{1}{2}\widehat{\mathcal{H}}_{\text{C}}. \tag{2.25}$$

For the first term, $\widehat{\mathcal{H}}_{\text{IP}}$, splitting the sum into holes and electrons leads to

$$\widehat{\mathcal{H}}_{\text{IP}} = \sum_i \epsilon_i \hat{a}_i^\dagger \hat{a}_i - \sum_\alpha \epsilon_\alpha \hat{b}_\alpha^\dagger \hat{b}_\alpha + \sum_\alpha \epsilon_\alpha, \tag{2.26}$$

where the last term, $\sum_\alpha \epsilon_\alpha$, is a renormalization term resulting form the use of Eq. (2.22). In a similar manner, $\widehat{\mathcal{H}}_{\text{MF}}$ is rewritten as

$$\widehat{\mathcal{H}}_{\text{MF}} = \sum_{ij} \langle i| v_{\text{MF}} |j\rangle \, \hat{a}_i^\dagger \hat{a}_j + \sum_{i\alpha} \left\{ \langle i| v_{\text{MF}} |\alpha\rangle \, \hat{a}_i^\dagger \hat{b}_\alpha^\dagger + \text{h.c.} \right\} + \sum_{\alpha\beta} \langle \alpha| v_{\text{MF}} |\beta\rangle \, \hat{b}_\alpha \hat{b}_\beta^\dagger, \tag{2.27}$$

where h.c. denotes the Hermitian conjugate. If v_{MF} is taken to be the Hartree-Fock potential, i.e. $\langle i|\, v_{\mathrm{MF}}\, |j\rangle = \sum_\alpha \langle i\alpha|\, v\, |j\alpha\rangle - \langle i\alpha|\, v\, |\alpha j\rangle$, the Hamiltonian associated with the mean-field can be expressed as

$$\widehat{\mathcal{H}}_{\mathrm{MF}} = \sum_{ij\alpha}(v_{i\alpha j\alpha} - v_{i\alpha\alpha j})\hat{a}_i^\dagger \hat{a}_j + \sum_{i\alpha\beta}\left\{(v_{\alpha\beta i\beta} - v_{\alpha\beta\beta i})\hat{b}_\alpha \hat{a}_i + \text{h.c.}\right\} + \sum_{\alpha\beta\gamma}(v_{\alpha\gamma\beta\gamma} - v_{\alpha\gamma\gamma\beta})\hat{b}_\alpha \hat{b}_\beta^\dagger. \tag{2.28}$$

Here, and henceforth, the notation $v_{ijkl} := \langle ij|\, v\, |kl\rangle$ is used. Now, the last term, $\widehat{\mathcal{H}}_{\mathrm{C}}$, features a quadruple sum, and therefore sixteen terms arise. Moving forward, the general strategy is to rearrange the operators in $\widehat{\mathcal{H}}_{\mathrm{C}}$ such that some terms entirely cancel $\widehat{\mathcal{H}}_{\mathrm{MF}}$ of Eq. (2.28). To ease the following derivation, the terms may be grouped by the composition of operators featured, that is

$$\begin{aligned}
\widehat{\mathcal{H}}_{\mathrm{C}} = &\underbrace{\sum_{ijkl} v_{ijkl}\hat{a}_i^\dagger \hat{a}_j^\dagger \hat{a}_l \hat{a}_k}_{ee} + \underbrace{\sum_{ijk\lambda} v_{ijk\lambda}\hat{a}_i^\dagger \hat{a}_j^\dagger \hat{b}_\lambda^\dagger \hat{a}_k}_{ex} + \underbrace{\sum_{ij\gamma l} v_{ij\gamma l}\hat{a}_i^\dagger \hat{a}_j^\dagger \hat{a}_l \hat{b}_\gamma^\dagger}_{ex} + \underbrace{\sum_{ij\gamma\lambda} v_{ij\gamma\lambda}\hat{a}_i^\dagger \hat{a}_j^\dagger \hat{b}_\lambda^\dagger \hat{b}_\gamma^\dagger}_{xx} \\
&+ \underbrace{\sum_{i\beta kl} v_{i\beta kl}\hat{a}_i^\dagger \hat{b}_\beta \hat{a}_l \hat{a}_k}_{ex} + \underbrace{\sum_{i\beta k\lambda} v_{i\beta k\lambda}\hat{a}_i^\dagger \hat{b}_\beta \hat{b}_\lambda^\dagger \hat{a}_k}_{eh} + \underbrace{\sum_{i\beta\gamma l} v_{i\beta\gamma l}\hat{a}_i^\dagger \hat{b}_\beta \hat{a}_l \hat{b}_\gamma^\dagger}_{eh} + \underbrace{\sum_{i\beta\gamma\lambda} v_{i\beta\gamma\lambda}\hat{a}_i^\dagger \hat{b}_\beta \hat{b}_\lambda^\dagger \hat{b}_\gamma^\dagger}_{hx} \\
&+ \underbrace{\sum_{\alpha jkl} v_{\alpha jkl}\hat{b}_\alpha \hat{a}_j^\dagger \hat{a}_l \hat{a}_k}_{ex} + \underbrace{\sum_{\alpha jk\lambda} v_{\alpha jk\lambda}\hat{b}_\alpha \hat{a}_j^\dagger \hat{b}_\lambda^\dagger \hat{a}_k}_{eh} + \underbrace{\sum_{\alpha j\gamma l} v_{\alpha j\gamma l}\hat{b}_\alpha \hat{a}_j^\dagger \hat{a}_l \hat{b}_\gamma^\dagger}_{eh} + \underbrace{\sum_{\alpha j\gamma\lambda} v_{\alpha j\gamma\lambda}\hat{b}_\alpha \hat{a}_j^\dagger \hat{b}_\lambda^\dagger \hat{b}_\gamma^\dagger}_{hx} \\
&+ \underbrace{\sum_{\alpha\beta kl} v_{\alpha\beta kl}\hat{b}_\alpha \hat{b}_\beta \hat{a}_l \hat{a}_k}_{xx} + \underbrace{\sum_{\alpha\beta k\lambda} v_{\alpha\beta k\lambda}\hat{b}_\alpha \hat{b}_\beta \hat{b}_\lambda^\dagger \hat{a}_k}_{hx} + \underbrace{\sum_{\alpha\beta\gamma l} v_{\alpha\beta\gamma l}\hat{b}_\alpha \hat{b}_\beta \hat{a}_l \hat{b}_\gamma^\dagger}_{hx} + \underbrace{\sum_{\alpha\beta\gamma\lambda} v_{\alpha\beta\gamma\lambda}\hat{b}_\alpha \hat{b}_\beta \hat{b}_\lambda^\dagger \hat{b}_\gamma^\dagger}_{hh}.
\end{aligned} \tag{2.29}$$

At first glance, it may seem as if the terms of $\widehat{\mathcal{H}}_{\mathrm{C}}$ no longer conserve the number of particles, which is true in the electron-hole picture. However, as reflected by Eqs. (2.19) and (2.20), the creation of a hole corresponds to the annihilation of an electron and vice versa. Moreover, the notation is not chosen arbitrarily, but reflects how different particle interactions contribute to the overall Hamiltonian, where e, h, and x represent electron, hole and exciton-like interactions, respectively. For example, the first term,

$$\widehat{\mathcal{H}}_{ee} = \sum_{ijkl} v_{ijkl}\hat{a}_i^\dagger \hat{a}_j^\dagger \hat{a}_l \hat{a}_k, \tag{2.30}$$

describes the electron-electron interaction between the created electron pair in states i, j and the annihilated electron pair in states k, l. Similarly, the last term describes pairwise hole-hole interactions, and can be rewritten using the

commutation relations of Eq. (2.22) combined with the fact that $v_{ijkl} = v_{jilk}$, thus yielding

$$\begin{aligned}\widehat{\mathcal{H}}_{hh} &= \sum_{\alpha\beta\gamma\lambda} v_{\alpha\beta\gamma\lambda}\hat{b}_\alpha\hat{b}_\beta\hat{b}_\lambda^\dagger\hat{b}_\gamma^\dagger \\ &= \sum_{\alpha\beta\gamma\lambda} v_{\alpha\beta\gamma\lambda}\hat{b}_\lambda^\dagger\hat{b}_\gamma^\dagger\hat{b}_\alpha\hat{b}_\beta + \sum_{\alpha\beta\gamma}(v_{\alpha\gamma\beta\gamma} - v_{\alpha\gamma\gamma\beta})(\hat{b}_\alpha\hat{b}_\beta^\dagger - \hat{b}_\beta^\dagger\hat{b}_\alpha) \\ &= \sum_{\alpha\beta\gamma\lambda} v_{\alpha\beta\gamma\lambda}\hat{b}_\lambda^\dagger\hat{b}_\gamma^\dagger\hat{b}_\alpha\hat{b}_\beta + 2\sum_{\alpha\beta\gamma}(v_{\alpha\gamma\beta\gamma} - v_{\alpha\gamma\gamma\beta})\hat{b}_\alpha\hat{b}_\beta^\dagger - \sum_{\alpha\gamma}(v_{\alpha\gamma\alpha\gamma} - v_{\alpha\gamma\gamma\alpha}).\end{aligned} \tag{2.31}$$

It is evident, that the second term in the last line of the above expression cancels with the last term of $\widehat{\mathcal{H}}_{\text{MF}}$, due to the factor $1/2$ in Eq. (2.25), and we will come to see that something similar happens to all the remaining terms of $\widehat{\mathcal{H}}_{\text{MF}}$. Proceeding, six of the terms in Eq. (2.29) contain two electron and two hole operators, and the four marked *eh* for electron-hole interaction have an equal number of creation and annihilation operators. These are collected into the term

$$\begin{aligned}\widehat{\mathcal{H}}_{eh} &= \sum_{i\beta k\lambda} v_{i\beta k\lambda}\hat{a}_i^\dagger\hat{b}_\beta\hat{b}_\lambda^\dagger\hat{a}_k + \sum_{i\beta\gamma l} v_{i\beta\gamma l}\hat{a}_i^\dagger\hat{b}_\beta\hat{a}_l\hat{b}_\gamma^\dagger + \sum_{\alpha jk\lambda} v_{\alpha jk\lambda}\hat{b}_\alpha\hat{a}_j^\dagger\hat{b}_\lambda^\dagger\hat{a}_k \\ &\quad + \sum_{\alpha j\gamma l} v_{\alpha j\gamma l}\hat{b}_\alpha\hat{a}_j^\dagger\hat{a}_l\hat{b}_\gamma^\dagger \\ &= 2\sum_{ij\alpha\beta}(v_{i\alpha j\beta} - v_{i\alpha\beta j})\hat{a}_i^\dagger\hat{b}_\alpha\hat{b}_\beta^\dagger\hat{a}_j \\ &= 2\sum_{ij\alpha\beta}(v_{i\alpha\beta j} - v_{i\alpha j\beta})\hat{a}_i^\dagger\hat{b}_\beta^\dagger\hat{b}_\alpha\hat{a}_j + 2\sum_{ij\alpha}(v_{i\alpha j\alpha} - v_{i\alpha\alpha j})\hat{a}_i^\dagger\hat{a}_j,\end{aligned} \tag{2.32}$$

where, once again, the last term cancels with the first term of $\widehat{\mathcal{H}}_{\text{MF}}$. The two remaining terms of Eq. (2.29) with two electron- and two hole operators, but an unequal number of annihilation and creation operators, are labeled *xx* and put into the term

$$\begin{aligned}\widehat{\mathcal{H}}_{xx} &= \sum_{ij\gamma\lambda} v_{ij\gamma\lambda}\hat{a}_i^\dagger\hat{a}_j^\dagger\hat{b}_\lambda^\dagger\hat{b}_\gamma^\dagger + \sum_{\alpha\beta kl} v_{\alpha\beta kl}\hat{b}_\alpha\hat{b}_\beta\hat{a}_l\hat{a}_k \\ &= \sum_{ij\alpha\beta}\Big\{v_{ij\alpha\beta}\hat{a}_i^\dagger\hat{b}_\beta^\dagger\hat{b}_\alpha^\dagger\hat{a}_j^\dagger + \text{h.c.}\Big\}.\end{aligned} \tag{2.33}$$

In a similar manner, the terms labeled *ex* are condensed into

$$\begin{aligned}\widehat{\mathcal{H}}_{ex} &= \sum_{ijk\lambda} v_{ijk\lambda}\hat{a}_i^\dagger\hat{a}_j^\dagger\hat{b}_\lambda^\dagger\hat{a}_k + \sum_{ij\gamma l} v_{ij\gamma l}\hat{a}_i^\dagger\hat{a}_j^\dagger\hat{a}_l\hat{b}_\gamma^\dagger + \sum_{i\beta kl} v_{i\beta kl}\hat{a}_i^\dagger\hat{b}_\beta\hat{a}_l\hat{a}_k \\ &\quad + \sum_{\alpha jkl} v_{\alpha jkl}\hat{b}_\alpha\hat{a}_j^\dagger\hat{a}_l\hat{a}_k \\ &= \sum_{ijk\alpha}\Big\{(v_{ijk\alpha} - v_{ij\alpha k})\hat{a}_j^\dagger\hat{b}_\alpha^\dagger\hat{a}_i^\dagger\hat{a}_k + \text{h.c.}\Big\}.\end{aligned} \tag{2.34}$$

Finally, the remaining terms of Eq. (2.29) are labeled *hx*. The idea is to simplify these terms in such a way that the second term of Eq. (2.28) cancels, which is slightly involved. It can be done as follows:

$$
\begin{aligned}
\hat{\mathcal{H}}_{hx} &= \sum_{i\beta\gamma\lambda} v_{i\beta\gamma\lambda}\hat{a}_i^\dagger \hat{b}_\beta \hat{b}_\lambda^\dagger \hat{b}_\gamma^\dagger + \sum_{\alpha j\gamma\lambda} v_{\alpha j\gamma\lambda}\hat{b}_\alpha \hat{a}_j^\dagger \hat{b}_\lambda^\dagger \hat{b}_\gamma^\dagger + \sum_{\alpha\beta k\lambda} v_{\alpha\beta k\lambda}\hat{b}_\alpha \hat{b}_\beta \hat{b}_\lambda^\dagger \hat{a}_k \\
&+ \sum_{\alpha\beta\gamma l} v_{\alpha\beta\gamma l}\hat{b}_\alpha \hat{b}_\beta \hat{a}_l \hat{b}_\gamma^\dagger \\
&= \sum_{i\alpha\beta\gamma} \Big\{ (v_{\alpha\beta i\gamma} - v_{\alpha\beta\gamma i})\hat{b}_\alpha \hat{b}_\beta \hat{b}_\gamma^\dagger \hat{a}_i + \text{h.c.} \Big\} \\
&= \sum_{i\alpha\beta\gamma} \Big\{ (v_{\alpha\beta\gamma i} - v_{\alpha\beta i\gamma})\hat{b}_\alpha \hat{b}_\gamma^\dagger \hat{b}_\beta \hat{a}_i + \text{h.c.} \Big\} + \sum_{i\alpha\beta} \Big\{ (v_{\alpha\beta i\beta} - v_{\alpha\beta\beta i})\hat{b}_\alpha \hat{a}_i + \text{h.c.} \Big\} \\
&= \sum_{i\alpha\beta\gamma} \Big\{ (v_{\alpha\beta\gamma i} - v_{\alpha\beta i\gamma})(\delta_{\gamma\alpha} - \hat{b}_\gamma^\dagger \hat{b}_\alpha)\hat{b}_\beta \hat{a}_i + \text{h.c.} \Big\} \\
&+ \sum_{i\alpha\beta} \Big\{ (v_{\alpha\beta i\beta} - v_{\alpha\beta\beta i})\hat{b}_\alpha \hat{a}_i + \text{h.c.} \Big\} \\
&= \sum_{i\alpha\beta\gamma} \Big\{ (v_{\alpha\beta i\gamma} - v_{\alpha\beta\gamma i})\hat{b}_\gamma^\dagger \hat{b}_\alpha \hat{b}_\beta \hat{a}_i + \text{h.c.} \Big\} + 2\sum_{i\alpha\beta} \Big\{ (v_{\alpha\beta i\beta} - v_{\alpha\beta\beta i})\hat{b}_\alpha \hat{a}_i + \text{h.c.} \Big\}.
\end{aligned}
\tag{2.35}
$$

The procedure in the above derivation mainly consists of moving $\hat{b}_\gamma^\dagger$ to the left by means of Eq. (2.22). This results in the last term, which exactly cancels with the second term of Eq. (2.28). It is worth noting that there is a discrepancy between the above expression and that of Eq. (7c) of Ref. [61], which follows a similar procedure. However, unless the operators are ordered as in Eq. (2.37), the second term of Eq. (2.28) does not cancel. Finally, the second quantized form of the many-body electron-hole Hamiltonian can then be written as

$$
\hat{\mathcal{H}} = E_c + \hat{\mathcal{H}}_0 + \hat{\mathcal{H}}_{eh} + \hat{\mathcal{H}}_{ee} + \hat{\mathcal{H}}_{hh} + \hat{\mathcal{H}}_{xx} + \hat{\mathcal{H}}_{ex} + \hat{\mathcal{H}}_{hx}, \tag{2.36}
$$

where

$$
\begin{aligned}
E_c &= \sum_\alpha \epsilon_\alpha + \frac{1}{2}\sum_{\alpha,\gamma} \big[\langle \alpha\gamma | v | \gamma\alpha \rangle - \langle \alpha\gamma | v | \alpha\gamma \rangle \big], \\
\hat{\mathcal{H}}_0 &= \sum_i \epsilon_i \hat{a}_i^\dagger \hat{a}_i - \sum_\alpha \epsilon_\alpha \hat{b}_\alpha^\dagger \hat{b}_\alpha, \\
\hat{\mathcal{H}}_{eh} &= \sum_{ij\alpha\beta} \big[\langle i\alpha | v | \beta j \rangle - \langle i\alpha | v | j\beta \rangle \big] \hat{a}_i^\dagger \hat{b}_\beta^\dagger \hat{b}_\alpha \hat{a}_j, \\
\hat{\mathcal{H}}_{ee} &= \frac{1}{2}\sum_{ijkl} \langle ij | v | kl \rangle \, \hat{a}_i^\dagger \hat{a}_j^\dagger \hat{a}_l \hat{a}_k, \\
\hat{\mathcal{H}}_{hh} &= \frac{1}{2}\sum_{\alpha\beta\gamma\lambda} \langle \alpha\beta | v | \gamma\lambda \rangle \, \hat{b}_\lambda^\dagger \hat{b}_\gamma^\dagger \hat{b}_\alpha \hat{b}_\beta, \\
\hat{\mathcal{H}}_{xx} &= \frac{1}{2}\sum_{ij\alpha\beta} \Big\{ \langle ij | v | \alpha\beta \rangle \, \hat{a}_i^\dagger \hat{b}_\beta^\dagger \hat{b}_\alpha^\dagger \hat{a}_j^\dagger + \text{h.c.} \Big\}, \\
\hat{\mathcal{H}}_{ex} &= \frac{1}{2}\sum_{ijk\alpha} \Big\{ \big[\langle ij | v | k\alpha \rangle - \langle ij | v | \alpha k \rangle \big] \hat{a}_j^\dagger \hat{b}_\alpha^\dagger \hat{a}_i^\dagger \hat{a}_k + \text{h.c.} \Big\}, \\
\hat{\mathcal{H}}_{hx} &= \frac{1}{2}\sum_{\alpha\beta\gamma i} \Big\{ \big[\langle \alpha\beta | v | \gamma i \rangle - \langle \alpha\beta | v | i\gamma \rangle \big] \hat{b}_\gamma^\dagger \hat{b}_\beta \hat{b}_\alpha \hat{a}_i + \text{h.c.} \Big\}.
\end{aligned}
\tag{2.37}
$$

Although the same naming convention has been used in the above expressions and Eqs. (2.30) to (2.35), the operators are not necessarily equivalent, since some terms have been canceled or rearranged. Moreover, the first term, E_c, contains no operators, and thus contributes no additional information about the excited states. On the other hand, $\widehat{\mathcal{H}}_0$ describes the non-interacting part of the Hamiltonian, and represents the kinetic energy of the the free fermions. The electron-electron and hole-hole interaction is included through $\widehat{\mathcal{H}}_{ee}$ and $\widehat{\mathcal{H}}_{hh}$, while the electron-hole coupling is contained by $\widehat{\mathcal{H}}_{eh}$. Specifically, $\widehat{\mathcal{H}}_{eh}$ consists of an attractive direct term and a repulsive exchange term. The last three terms describe how exciton-like electron-hole pairs interact with themselves ($\widehat{\mathcal{H}}_{xx}$), with electrons ($\widehat{\mathcal{H}}_{ex}$), and with holes ($\widehat{\mathcal{H}}_{hx}$).

2.3.3 Truncated Formalism

With the second quantized electron-hole Hamiltonian now developed, it can be used to compute the Coulomb-bound many-body excited states of a given system. The basis for $\widehat{\mathcal{H}}$ is the span of all possible excitation levels, which leads to a wave function of the form

$$|\Psi^{\mathrm{CI}}\rangle = A^{(0)}|\Omega\rangle + \sum_{i\alpha} A^{(1)}_{i\alpha}|i\alpha\rangle + \sum_{ij\alpha\beta} A^{(2)}_{ij\alpha\beta}|ij\alpha\beta\rangle + \sum_{ijk\alpha\beta\gamma} A^{(3)}_{ijk\alpha\beta\gamma}|ijk\alpha\beta\gamma\rangle + \ldots, \quad (2.38)$$

where $|i\alpha\rangle = \hat{a}_i^\dagger \hat{b}_\alpha^\dagger |\Omega\rangle$ are the singly excited configurations as illustrated in Fig. 2.1(b), i.e. one electron has been excited from below the Fermi level to above it. Similarly, the doubly excited configurations, represented by $|ij\alpha\beta\rangle = \hat{a}_i^\dagger \hat{a}_j^\dagger \hat{b}_\alpha^\dagger \hat{b}_\beta^\dagger |\Omega\rangle$, involve two electrons excited from below the Fermi level as seen in Fig. 2.1(c), with conditions $i < j$ and $\alpha < \beta$ to avoid double counting and adhere to Pauli's exclusion principle. Although, in theory, this linear combination could extend infinitely, practical applications necessitate truncating the basis to a manageable number of states, which in turn limits the extend of excitation levels.

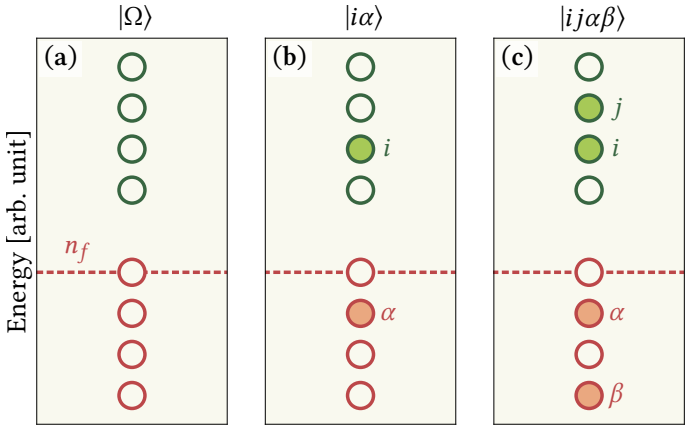

Figure 2.1: (a) The ground state, which features empty electron states (purple) above the Fermi level, n_f, and empty hole states below (orange). (b) A singly excited configuration where electron state, i, and hole state, α, have been filled. (c) Doubly excited configuration having further states j and β filled.

The wavefunction coefficients $A^{(0)}$, $A^{(1)}_{i\alpha}$, $A^{(2)}_{ij\alpha\beta}$ and so on of Eq. (2.38) are the solutions of the eigenvalue problem associated with $\widehat{\mathcal{H}}$ in the many-body excited basis, which corresponds to diagonalizing a matrix of the following form:

$$\begin{array}{r} \langle\Omega| \\ \langle i\alpha| \\ \langle ij\alpha\beta| \\ \langle ijk\alpha\beta\gamma| \\ \vdots \end{array} \begin{pmatrix} E_0 & 0 & v_{02} & 0 & 0 & 0 & \dots \\ 0 & E_1 & v_{12} & v_{13} & 0 & 0 & \dots \\ v_{02}^\dagger & v_{12}^\dagger & E_2 & v_{23} & v_{24} & 0 & \dots \\ 0 & v_{13}^\dagger & v_{23}^\dagger & E_3 & v_{34} & v_{35} & \dots \\ 0 & 0 & v_{24}^\dagger & v_{34}^\dagger & E_4 & v_{45} & \dots \\ 0 & 0 & 0 & v_{35}^\dagger & v_{45}^\dagger & E_5 & \dots \\ \vdots & \vdots & \vdots & \vdots & \vdots & \vdots & \ddots \end{pmatrix} \begin{pmatrix} A^{(0)} \\ A^{(1)} \\ A^{(2)} \\ A^{(3)} \\ A^{(4)} \\ A^{(5)} \\ \vdots \end{pmatrix} = E_\lambda \begin{pmatrix} A^{(0)} \\ A^{(1)} \\ A^{(2)} \\ A^{(3)} \\ A^{(4)} \\ A^{(5)} \\ \vdots \end{pmatrix} \tag{2.39}$$

The diagonal elements, E_x, are computed only within their respective subspaces, that is, for a given level of excited determinants (ED). In contrast, the off-diagonal elements, v_{xy}, correspond to the coupling between different EDs, and, notably, the off-diagonal elements between the ground state and the singly EDs are zero, which is known as Brillouin's theorem [62]. Moreover, as a consequence of the Slater-Condon rules [63, 64], off-diagonal elements computed between EDs differing in more than two spin-orbitals, e.g. between singly EDs and triply EDs, vanish, explaining the structure of the matrix.

The procedure of finding the matrix elements and subsequently diagonalizing the matrix of Eq. (2.39) is commonly referred to as full CI, since no restrictions are made on the level of EDs. However, approximations do exists within in the CI framework, with some of the more common being CI singles (CIS), CI doubles (CID), and CI singles and doubles (CISD). CIS refers to a restricted CI procedure, where only the subspace of singly ED constitute the (incomplete) basis, which corresponds to diagonalizing E_1. Analogously, in the CID formalism, the subspace is restricted to doubly EDs, while CISD include singly EDs, doubly EDs and the coupling between these. A notable drawback with the truncated CI procedures, however, is their size-inconsistency [65], meaning that the energy of two non-interacting systems calculated together does not equal the sum of their individual energies, which tends to lead to inaccuracies for larger systems.

In the particular case of CIS, each singly ED essentially consists of only one electron-hole pair, and as such the solutions are of the form, $|\mathrm{X}\rangle = \sum_{i\alpha} A_{i\alpha} |i\alpha\rangle$, commonly referred to as excitons. In this sense, E_1, represents the excitonic Hamiltonian, and by referring to Eq. (2.36), it can be seen that the matrix elements of E_1 are

$$\langle i\alpha| \widehat{\mathcal{H}} |j\beta\rangle = (E_c + \epsilon_i - \epsilon_\alpha)\delta_{ij}\delta_{\alpha\beta} - \langle i\beta| v |j\alpha\rangle + \langle i\beta| v |\alpha j\rangle ,$$

where all terms of $\widehat{\mathcal{H}}$ has vanishing contributions except for E_c, $\widehat{\mathcal{H}}_0$ and $\widehat{\mathcal{H}}_{eh}$. In general, when projecting into a subspace of only one specific level of EDs, the terms $\widehat{\mathcal{H}}_{xx}$, $\widehat{\mathcal{H}}_{ex}$ and $\widehat{\mathcal{H}}_{hx}$ vanish. This can be seen quite easily, since they feature an uneven number of creation and annihilation operators, and therefore do not conserve the number of particles. As such, in a truncated CI formalism limited to one level of excitation, these three operators can be ignored. Additionally, since

E_c only contributes a constant to the eigenvalues, it can be disregarded as well. With this in mind, the matrix elements can be reformulated as

$$\langle i\alpha|\,\widehat{\mathcal{H}}\,|j\beta\rangle = (\epsilon_i - \epsilon_\alpha)\delta_{ij}\delta_{\alpha\beta} - \underbrace{\langle i\beta|\,v\,|j\alpha\rangle}_{J_{eh}} + \underbrace{\langle i\beta|\,v\,|\alpha j\rangle}_{K_{eh}}. \tag{2.40}$$

Here, the second term, J_{eh}, denotes the attractive term often called the direct/-Coulomb interaction, whereas the last term, K_{eh} represents the repulsive exchange interaction. These matrix elements may be compared to those of the effective GW/Bethe-Salpeter equation (GW/BSE) in the Tamm-Dancoff approximation [66], namely

$$\langle i\alpha|\,\widehat{\mathcal{H}}_{\text{BSE}}\,|j\beta\rangle = (\epsilon_i^{\text{qp}} - \epsilon_\alpha^{\text{qp}})\delta_{ij}\delta_{\alpha\beta} - \langle i\beta|\,W\,|j\alpha\rangle + \langle i\beta|\,v\,|\alpha j\rangle. \tag{2.41}$$

Clearly, some key differences exists here; first off all, the direct term in the GW/BSE Hamiltonian features a screened interaction, W, and secondly, the independent particle (or Kohn-Sham) eigenvalues are replaced by the quasi-particle ones, ϵ^{qp}. The screened interaction is of the form:

$$W(\mathbf{r}_1, \mathbf{r}_2) = \int \epsilon^{-1}(\mathbf{r}_1, \mathbf{r}_3) v(\mathbf{r}_3, \mathbf{r}_2)\, \mathrm{d}\mathbf{r}_3, \tag{2.42}$$

where ϵ^{-1} represents the inverse dielectric function. The quasi-particle energies arise from electronic correlation effects introduced through the self-energy, which effectively accounts for electron-electron interactions beyond the mean-field approximation. As a result, the independent particle energies are renormalized by this self-energy correction, providing a more accurate description of the systems electronic structure [67].

In summary, the many-body Hamiltonian found in Eq. (2.37) encapsulates the full CI formalism. However, when truncating the basis to a specific level of EDs, the last three terms have vanishing contributions, and the first term may be omitted, since it merely offsets the eigenvalues by a constant. Additionally, there are evident discrepancies between the GW/BSE Hamiltonian of Eq. (2.41) and Eq. (2.16), namely the quasi-particle energies and the screening of the direct Coulomb interaction. With all this in mind, $\widehat{\mathcal{H}}$ may be reformulated as

$$\widehat{\mathcal{H}} = \widehat{\mathcal{H}}_0 + \widehat{\mathcal{H}}_{eh} + \widehat{\mathcal{H}}_{ee} + \widehat{\mathcal{H}}_{hh}, \tag{2.43}$$

where

$$\widehat{\mathcal{H}}_0 = \sum_i \epsilon_i^{\text{qp}} \hat{a}_i^\dagger \hat{a}_i - \sum_\alpha \epsilon_\alpha^{\text{qp}} \hat{b}_\alpha^\dagger \hat{b}_\alpha, \quad \widehat{\mathcal{H}}_{eh} = \sum_{ij\alpha\beta} \left[\, \langle i\alpha|\,v\,|\beta j\rangle - \langle i\alpha|\,W\,|j\beta\rangle \,\right] \hat{a}_i^\dagger \hat{b}_\beta^\dagger \hat{b}_\alpha \hat{a}_j,$$
$$\widehat{\mathcal{H}}_{ee} = \frac{1}{2}\sum_{ijkl} \langle ij|\,W\,|kl\rangle\, \hat{a}_i^\dagger \hat{a}_j^\dagger \hat{a}_l \hat{a}_k, \quad \widehat{\mathcal{H}}_{hh} = \frac{1}{2}\sum_{\alpha\beta\gamma\lambda} \langle \alpha\beta|\,W\,|\gamma\lambda\rangle\, \hat{b}_\lambda^\dagger \hat{b}_\gamma^\dagger \hat{b}_\alpha \hat{b}_\beta.$$

It should be stressed that this new $\widehat{\mathcal{H}}$ only applies when the basis is confined to a subspace consisting of just a single level of EDs, since the off-diagonal elements v_{xy} seen in Eq. (2.39) require the inclusion of $\widehat{\mathcal{H}}_{xx}$, $\widehat{\mathcal{H}}_{ex}$ and $\widehat{\mathcal{H}}_{hx}$.

3

Methods

This chapter presents the implementation of the CI procedure as described in Chapter 2, which can be summarized in three main steps. First, the independent particle wavefunctions and energies are obtained through a DFT calculation, performed in this work using the `Quantum ESPRESSO` (QE) suite [68, 69]. The second step is the dielectric screening - a computationally demanding quantity obtained within the `YAMBO` framework [70, 71]. Since the QE and `YAMBO` packages are external, this chapter does not focus on the theory or implementation of these. Finally, when the prerequisite calculations are finished, the actual CI procedure is carried out. For this purpose, and inspired by earlier works [45–47], the `MX`-package was developed in this work for 2D materials. All CI-based results presented throughout this thesis are computed using this package. For a more thorough explanation of the entire procedure, and an in-depth tutorial for the `MX`-package, please refer to Chapter A.

Contents

3.1 Plane-wave Basis

As is the case for any periodic system, the wavefunctions used in DFT adhere to Bloch's theorem, such that

$$|n\rangle = u_n(\mathbf{r})e^{i\mathbf{k}_n\cdot\mathbf{r}}, \tag{3.1}$$

where $n = (n, \mathbf{k}_n)$ denotes both a band index, n, and k-point, $\mathbf{k}_n$. The Bloch function, u_n, is (generally) a two-component spinor. Moreover, it is periodic with the lattice, and may be expressed in terms of its Fourier transform, that is

$$u_n(\mathbf{r}) = \frac{1}{\sqrt{\Omega}} \sum_j u_n(\mathbf{G}_j)e^{i\mathbf{G}_j\cdot\mathbf{r}}. \tag{3.2}$$

Here, $\mathbf{G}_j$ denote the reciprocal lattice points, while Ω represents the primitive cell volume. Eq. (3.2) is essentially an expansion of the Bloch function into plane-wave components, and the amount of $\mathbf{G}_j$ included, n_G, is a parameter that needs to be converged in terms of a *cut-off energy*, E_cut, such that

$$\frac{1}{2}(\mathbf{k} + \mathbf{G}_j)^2 < E_\mathrm{cut}, \tag{3.3}$$

for all $\mathbf{G}_j$, where all terms are in atomic units. This implies that the norm of any included **G**-vectors must not exceed a certain threshold, G_max. Consequently, these **G**-vectors form a sphere in reciprocal space with radius G_max, such that $n_\mathrm{G} \propto (G_\mathrm{max})^3$. In conjunction with Eq. (3.3), this relationship indicates that $n_\mathrm{G} \propto (E_\mathrm{cut})^{3/2}$, which is further illustrated in Fig. 3.1, where the total energy seems converged around 60 Ry. As such, larger values of E_cut lead to a substantial increase in the

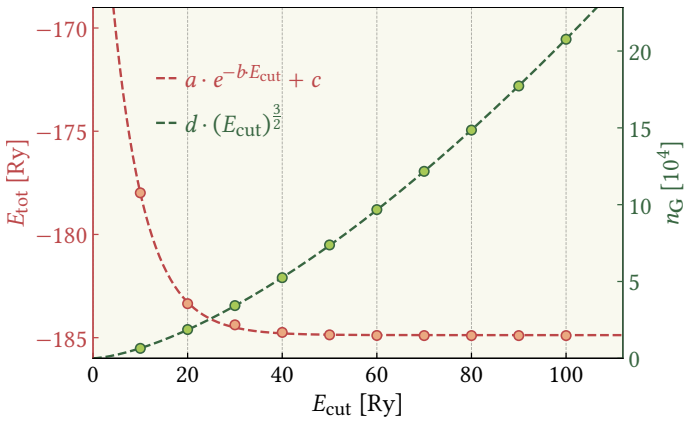

Figure 3.1: Convergence of the total energy, E_tot, of monolayer MoS_2 with respect to E_cut fitted with a decaying exponential (orange). Additionally, the number of **G**-vectors, n_G, corresponding to each value of E_cut are shown, including a fit $\propto E_\mathrm{cut}^{3/2}$ (green).

file-size of wavefunction coefficients, and, equally or more important, an increase in the computational time of operations with said wavefunctions, e.g. the fast Fourier transform (FFT).

3.2 Computing Matrix Elements

As can be seen from Eq. (2.43), the bulk of the CI procedure is the computation of two-body matrix elements, namely

$$\langle ij|\, v\, |kl\rangle = \int \varphi_i^*(1)\varphi_j^*(2) v(\mathbf{r}_1,\mathbf{r}_2)\varphi_k(1)\varphi_l(2)\,\mathrm{d}1\,\mathrm{d}2, \tag{3.4}$$

$$\langle ij|\, W\, |kl\rangle = \int \varphi_i^*(1)\varphi_j^*(2) W(\mathbf{r}_1,\mathbf{r}_2)\varphi_k(1)\varphi_l(2)\,\mathrm{d}1\,\mathrm{d}2, \tag{3.5}$$

where v represents the bare Coulomb interaction kernel and W the screened one, which both formulate the scattering process between $\langle ij|$ and $|kl\rangle$. Since the Kohn-Sham wavefunctions, φ_n, are two-component spinors, the notation $1 = (\mathbf{r}_1, \sigma)$ combines both position, $\mathbf{r}$, and spin degrees of freedom, σ, while $\int \mathrm{d}1 = \sum_{\sigma=\uparrow,\downarrow} \int \mathrm{d}\mathbf{r}_1$ includes spin summation.

3.2.1 The Coulomb Kernel

As is the case for the wavefunctions, the Coulomb kernel, v, may also be represented in terms of its Fourier transform, such that

$$v(\mathbf{r}_1,\mathbf{r}_2) = \frac{1}{\Omega}\sum_{\mathbf{q},\mathbf{G}} v_{\mathrm{G}}(\mathbf{q}) e^{i(\mathbf{q}+\mathbf{G})(\mathbf{r}_1-\mathbf{r}_2)}. \tag{3.6}$$

Here, $v_{\mathrm{G}}(\mathbf{q})$ is the Fourier transform of $v(\mathbf{r}_1,\mathbf{r}_2) = |\mathbf{r}_1 - \mathbf{r}_2|^{-1}$, which is simply $v_{\mathrm{G}}(\mathbf{q}) = 4\pi|\mathbf{q}+\mathbf{G}|^{-2}$, where $\mathbf{G}$ are the reciprocal lattice points, while $\mathbf{q}$ only takes on values within the first Brillouin zone (BZ) - similar to k-points.

While the DFT unit cell and thereby the wavefunctions adhere to periodic boundary conditions along all three cartesian axes, the focus of the work is 2D materials. Therefore, to avoid artificial interactions between out-of-plane periodic images in DFT, a layer of vacuum is introduced to the unit cell along this direction. Although a vacuum of around 10-20 Å typically suffices in DFT calculations, the long-range components of the Coulomb interaction and the response functions still require additional suppression in the out-of-plane direction. This is achieved by letting $v_{\mathrm{G}}(\mathbf{q}) := v_{\mathrm{G}}^{\mathrm{2D}}(\mathbf{q})$ [72, 73], where

$$v_{\mathrm{G}}^{\mathrm{2D}}(\mathbf{q}) = \frac{4\pi}{|\mathbf{q}+\mathbf{G}|^2}\left\{1 - e^{-|\mathbf{q}_\parallel+\mathbf{G}_\parallel|\frac{L_z}{2}}\cos\left(|q_z+G_z|\frac{L_z}{2}\right)\right\}, \tag{3.7}$$

with L_z being the out-of-plane length of the unit cell. Moreover, $\mathbf{q}_\parallel = (q_x, q_y)$ and $\mathbf{G}_\parallel = (G_x, G_y)$ are the in-plane components of $\mathbf{q}$ and $\mathbf{G}$, respectively. The form of Eq. (3.7) is not trivial, but the details behind its nature is not explored in this work.

Clearly, in the limit of $\mathbf{q} = \mathbf{G} = 0$, special care must be taken for $v_{\mathrm{G}}^{\mathrm{2D}}(\mathbf{q})$. The method used in this work to treat the divergent nature of this limit is inspired by that of Marini et al. [70]. In Fig. 3.2(a), the first BZ is depicted with the discrete q-points included, and the inset shows the Voronoi region of q-points that $\mathbf{q} = \Gamma = (0,0,0)$ actually represents. The area of this region is denoted A_q, and is simply $A_q = (2\pi)^2 L_z/(\Omega n_q)$, where n_q is the number of q-points within

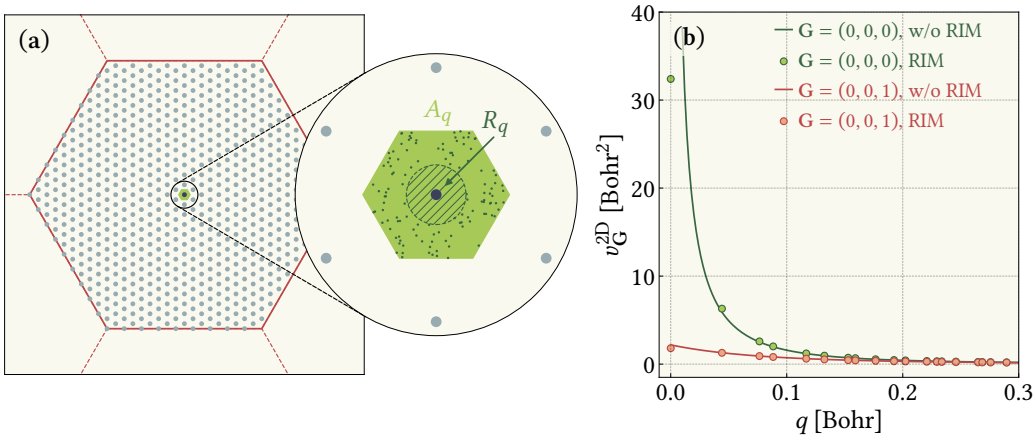

Figure 3.2: (a) The first BZ and the q-points of a 27×27 Monkhorst grid. The inset zooms in on a region near Γ (green) and shows the area, A_q, associated with $\mathbf{q}_\Gamma = (0, 0, 0)$ (green) and the circular region, R_q, in which the potential is treated semi-analytically (striped). The random points are marked in dark green. (b) The Fourier transformed 2D Coulomb potential, v^{2D}, as a function $q = |\mathbf{q}|$ for $\mathbf{G} = (0, 0, 0)$ (green) and $\mathbf{G} = (0, 0, 1)$ (orange), where the solid lines represent values computed without use of the RIM, while dots are computed with use of the RIM.

the first BZ, and Ω denotes the unit cell volume. In order to compute $v_0^{2D}(0)$, a random integration method (RIM) is employed here, such that

$$v_0^{2D}(0) \simeq \frac{1}{A_q} \int_{A_q} v_0^{2D}(\mathbf{q}')\, \mathrm{d}\mathbf{q}' \simeq \frac{1}{n_{\mathrm{RIM}}} \sum_i^{n_{\mathrm{RIM}}} v_0^{2D}(\mathbf{q}_i') \tag{3.8}$$

where $\mathbf{q}_i'$ denote the random points and n_{RIM} is the amount of these, which is typically set to 10^6. However, when the random points approach Γ, this method is insufficient. As such, a circular region, R_q, with area defined as $R_q = 0.2A_q$ has been marked near Γ in the inset of Fig. 3.2, where the divergency is treated semi-analytically by performing an average. Therefore, the previous expression becomes

$$v_0^{2D}(0) \simeq \frac{1}{A_q} \left[\int_{A_q \setminus R_q} v_0^{2D}(\mathbf{q}')\, \mathrm{d}\mathbf{q}' + \int_{R_q} v_0^{2D}(\mathbf{q})\, \mathrm{d}\mathbf{q} \right], \tag{3.9}$$

As there is no electronic dispersion along the out-of-plane axis of 2D materials, the q-points do not feature any out-of-plane components. Moreover, $\mathbf{G} = 0$, and as such, the cosine of Eq. (3.7) is simply unity, meaning that

$$\int_{R_q} v_0^{2D}(\mathbf{q})\, \mathrm{d}\mathbf{q} = 4\pi \int_{\phi=0}^{2\pi} \int_{q=0}^{\sqrt{R_q/\pi}} \frac{1}{q^2} \left\{ 1 - e^{-q\frac{L_z}{2}} \right\} q\, \mathrm{d}q\, \mathrm{d}\phi. \tag{3.10}$$

To ease the evaluation of this integral, we can make the substitution that $x = qL_z/2$, such that

$$\int_{R_q} v_0^{2D}(\mathbf{q})\, \mathrm{d}\mathbf{q} = 4\pi \cdot 2\pi \int_{x=0}^{\sqrt{\frac{R_q}{\pi}}\frac{L_z}{2}} \frac{1 - e^{-x}}{x}\, \mathrm{d}x. \tag{3.11}$$

The exponential can be expanded around $x = 0$ as $\lim_{x\to 0} e^{-x} = \sum_{n=0}^{\infty}(-x)^n/n!$, which finally reduces the expression to

$$\int_{R_q} v_0^{\mathrm{2D}}(\mathbf{q})\,\mathrm{d}\mathbf{q} = 4\pi\cdot 2\pi \sum_{n=1}^{\infty} \frac{(-1)^{n-1}}{n\cdot n!}\left(\sqrt{\frac{R_q}{\pi}}\frac{L_z}{2}\right)^n. \tag{3.12}$$

Regarding implementation, the RIM is indeed used for all q-points within the first BZ, i.e. $\mathbf{G} = 0$, $\mathbf{q} \neq 0$. However, it is only for the case $\mathbf{q} = \mathbf{G} = 0$, where R_q needs special treatment. Further than that, because the reciprocal lattice points typically pack quite densely along the out-of-plane direction, the RIM can even be advantageous for $\mathbf{G} \neq 0$. In the general case,

$$v_{\mathrm{G}}^{\mathrm{2D}}(\mathbf{q}) \simeq \frac{1}{A_q}\int_{A_q} v_{\mathrm{G}}^{\mathrm{2D}}(\mathbf{q}+\mathbf{q}')\,\mathrm{d}\mathbf{q}'. \tag{3.13}$$

By sorting the $\mathbf{G}$-vectors according to their norm, an index can be chosen such that $v_{\mathrm{G}}^{\mathrm{2D}}(\mathbf{q})$ is computed using Eq. (3.13) for all $\mathbf{G}$-vectors below or equal to this index, except for when $\mathbf{q} = \mathbf{G} = 0$, where Eq. (3.9) is used. All $\mathbf{G}$-vectors that fall above this index, are computed by Eq. (3.7). For the systems included in this work, it is typically sufficient to employ the RIM only for the first three $\mathbf{G}$-vectors.

Many of the matrix elements feature the screened Coulomb kernel, W, which, similar to v, can be represented in terms of its Fourier transform [74]. Formally,

$$W(\mathbf{r}_1,\mathbf{r}_2) = \frac{1}{\Omega}\sum_{\mathbf{q},\mathrm{G},\mathrm{G}'} W_{\mathrm{G}\mathrm{G}'}(\mathbf{q}) e^{i(\mathbf{q}+\mathrm{G})\mathbf{r}_1} e^{-i(\mathbf{q}+\mathrm{G}')\mathbf{r}_2}, \tag{3.14}$$

where

$$W_{\mathrm{G}\mathrm{G}'}(\mathbf{q}) = \epsilon^{-1}_{\mathrm{G}\mathrm{G}'}(\mathbf{q},\omega=0)\sqrt{v_{\mathrm{G}}(\mathbf{q})}\sqrt{v_{\mathrm{G}'}(\mathbf{q})}. \tag{3.15}$$

Here, $\epsilon^{-1}_{\mathrm{G}\mathrm{G}'}(\mathbf{q},\omega=0)$ is the Fourier transform of the static part of the inverse dielectric screening ($\omega = 0$).

3.2.2 Explicit Expression of Matrix Elements

A more explicit form of the unscreened matrix elements can be realized by combining Eqs. (3.1), (3.4) and (3.6), such that

$$\begin{aligned}\langle ij|\,v\,|kl\rangle = \frac{1}{\Omega^3}\sum_{\mathbf{q},\mathrm{G}} v_{\mathrm{G}}(\mathbf{q}) \int u_i^*(1)u_k(1)e^{i\mathrm{G}\mathbf{r}_1} e^{i(\mathbf{k}_k-\mathbf{k}_i+\mathbf{q})\mathbf{r}_1}\,\mathrm{d}1 \\ \times \int u_j^*(2)u_l(2)e^{-i\mathrm{G}\mathbf{r}_2} e^{i(\mathbf{k}_l-\mathbf{k}_j-\mathbf{q})\mathbf{r}_2}\,\mathrm{d}2.\end{aligned} \tag{3.16}$$

Now, the first integral is only non-zero when $\mathbf{k}_k - \mathbf{k}_i + \mathbf{q} = 0$ up to a reciprocal lattice vector, since the integral is over the unit cell. For the same reason, the term $e^{i\mathrm{G}\mathbf{r}_1}$ will never make the integral vanish. Moreover, an analogous condition holds true for the second integral, and thus

$$\langle ij|\,v\,|kl\rangle = \frac{1}{\Omega^3}\sum_{\mathbf{q},\mathrm{G}} v_{\mathrm{G}}(\mathbf{q}) \int u_i^*(1)u_k(1)e^{i\mathrm{G}\mathbf{r}_1}\,\mathrm{d}1\,\delta_{\mathbf{q},\mathbf{q}_{ik}} \int u_j^*(2)u_l(2)e^{-i\mathrm{G}\mathbf{r}_2}\,\mathrm{d}2\,\delta_{\mathbf{q},\mathbf{q}_{lj}}, \tag{3.17}$$

where $\mathbf{q}_{ik} = \mathbf{k}_i - \mathbf{k}_k$, and the two Kronecker-Delta functions further imply that $\mathbf{k}_i - \mathbf{k}_k = \mathbf{k}_l - \mathbf{k}_j$. This is, however, always satisfied given the way the configurations are chosen, which is discussed in Section 3.3.1. To further reduce Eq. (3.17), it is helpful to define

$$\rho_{ik}(\mathbf{r}_1) = \sum_{\sigma=\uparrow,\downarrow} u_i^*(1) u_k(1), \tag{3.18}$$

which is an element of the density matrix of Bloch functions. Moreover, the Fourier transform of $\rho_{ik}(\mathbf{r}_1)$ is

$$\rho_{ik}(\mathbf{G}) = \frac{1}{\Omega} \int \rho_{ik}(\mathbf{r}_1) e^{i\mathbf{G}\mathbf{r}_1} \, \mathrm{d}\mathbf{r}_1, \tag{3.19}$$

which can be used in Eq. (3.17) to arrive at the final expression,

$$\langle ij| v |kl\rangle = \frac{1}{\Omega} \sum_{\mathbf{G}\neq 0} \rho_{lj}(\mathbf{G})^* v_{\mathbf{G}}(\mathbf{q}_{ik}) \rho_{ik}(\mathbf{G}), \tag{3.20}$$

Notably, the $\mathbf{G} = 0$ term has been excluded to ensure consistency between the BSE and our many-body Hamiltonian when projecting into the exciton subspace [66, 75]. The compressed form of Eq. (3.20) demonstrates the procedure implemented to compute unscreened matrix elements. First, the wavefunctions are read directly from QE in reciprocal space, $u_n(\mathbf{G})$, and then immediately Fourier transformed to obtain $u_n(\mathbf{r})$ for all n included in the CI calculation. During the computation of each matrix element, $\rho_{ik}(\mathbf{r})$ and $\rho_{jl}(\mathbf{r})$ are evaluated and then inverse Fourier transformed to obtain $\rho_{ik}(\mathbf{G})$ and $\rho_{jl}(\mathbf{G})$. In the final step, namely Eq. (3.20), $\langle ij| v |kl\rangle$ is readily obtained as an element-wise vector product followed by an inner product, since all three constituents are simply stored as vectors over $\mathbf{G}$.

Using a similar procedure, a more compact form of the screened matrix elements can be formulated, namely

$$\langle ij| W |kl\rangle = \frac{1}{\Omega} \sum_{\mathbf{G},\mathbf{G}'} \rho_{lj}(\mathbf{G}')^* W_{\mathbf{G}\mathbf{G}'}(\mathbf{q}_{ik}) \rho_{ik}(\mathbf{G}), \tag{3.21}$$

which can be evaluated as a matrix-vector product followed by an inner product.

For both unscreened and screened matrix elements, $\rho_{ik}(\mathbf{G})$ and $\rho_{lj}(\mathbf{G}')$ must be evaluated. However, it is not a trivial matter to compute these, since the wavefunctions obtained from QE are stored only for k-points within the irreducible Brillouin zone (IBZ). This is particularly challenging for matrix elements involving states outside the IBZ, as it requires the application of symmetry operations to both the spatial and spin parts of the wavefunctions. Likewise, $\epsilon^{-1}_{\mathbf{G}\mathbf{G}'}(\mathbf{q})$ is stored only for q-points within the IBZ, which further necessitates that $\rho_{lj}(\mathbf{G}')$, $\rho_{ik}(\mathbf{G})$ and $W_{\mathbf{G}\mathbf{G}'}(\mathbf{q}_{ik})$ of Eq. (3.21) are aligned via symmetry operations when ($\mathbf{q}_{ik}$ lies outside the IBZ. This is discussed in further details in the following section.

3.2.3 Symmetries and Unfolding

As a prerequisite to any DFT calculation, the inherent symmetries of the system are analyzed. These symmetries include rotations, inversion, identity, and reflections,

or any combinations thereof. Additionally, non-symmorphic symmetries may be present, such as fractional translations, although this is not the case for any materials studied in this work. Identifying these symmetries allows for a reduction of the k-point sampling to the IBZ, which substantially decreases the computational resources needed. That is, instead of computing and storing the wavefunction for all k-points, only the irreducible k-points and their wavefunctions are stored along with the symmetry operations needed to generate all k-points and wavefunctions. This is illustrated in Fig. 3.3. In Fig. 3.3(a), the k-points included in a DFT calculation

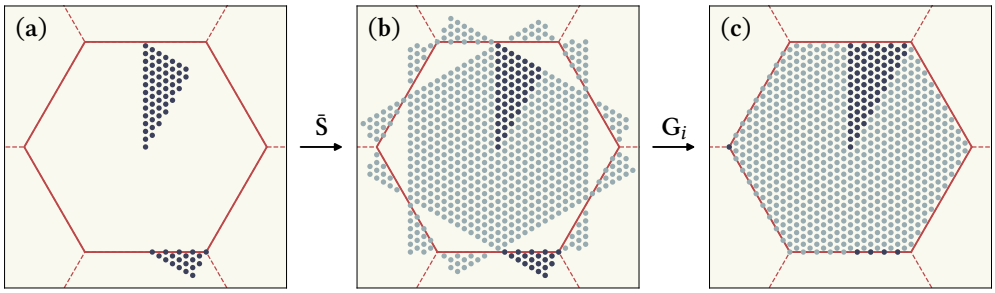

Figure 3.3: (a) The irreducible k-points marked in dark blue along with the first BZ marked by a solid orange line. (b) Similar to (a), but with the full k-point sampling generated by applying symmetry operations marked in light blue. (c) Similar to (b), but all k-points are translated into the first BZ with the help of **G**-vectors.

for monolayer MoS_2 are shown for an input sampling of 27×27 k-points. Then, in Fig. 3.3(b), symmetry operations are applied to the irreducible k-points, and the entirety of the requested k-point sampling is recovered. Lastly, and mainly for visualization purposes, in Fig. 3.3(c), the now unfolded k-points have been translated into the first BZ using **G**-vectors.

Generally, the symmetry operations are represented as three-dimensional (3D) rotation matrices,

$$\bar{\mathbf{S}} = \bar{\mathbf{R}}(\mathbf{u}, \theta), \tag{3.22}$$

where $\mathbf{u}$ is the axis of rotation, and θ is the angle of rotation. One example of a symmetry operation for monolayer MoS_2 is a 120° rotation around the z-axis, which is represented as

$$\bar{\mathbf{S}} = \bar{\mathbf{R}}(\hat{z}, 2\pi/3) = \begin{pmatrix} -1/2 & -\sqrt{3}/2 & 0 \\ \sqrt{3}/2 & -1/2 & 0 \\ 0 & 0 & 1 \end{pmatrix}. \tag{3.23}$$

However, for this specific example, QE stores the non-unitary matrix

$$\bar{\mathbf{S}}_c = \begin{pmatrix} -1 & -1 & 0 \\ 1 & 0 & 0 \\ 0 & 0 & 1 \end{pmatrix}. \tag{3.24}$$

The reason for this discrepancy is that $\bar{\mathbf{S}}$ rotates coordinates in cartesian space, $\mathbf{r}$, while $\bar{\mathbf{S}}_c$ rotates crystal coordinates, $\mathbf{r}_c$. The two coordinate systems are related by

$$\mathbf{r} = \bar{\mathbf{A}} \cdot \mathbf{r}_c, \quad \bar{\mathbf{A}} = \begin{pmatrix} a_{1,x} & a_{2,x} & a_{3,x} \\ a_{1,y} & a_{2,y} & a_{3,y} \\ a_{1,z} & a_{2,z} & a_{3,z} \end{pmatrix}, \tag{3.25}$$

Here, $\bar{\mathbf{A}}$ is a "change-of-basis matrix" that holds the unit cell vectors, e.g. $a_{1,x}$ is the x-component of first lattice vector. In extension, the relation between $\bar{\mathbf{S}}$ and $\bar{\mathbf{S}}_c$ is a change of basis as well, that is

$$\bar{\mathbf{S}} = \bar{\mathbf{A}}^{-1}\,\bar{\mathbf{S}}_c\,\bar{\mathbf{A}}. \tag{3.26}$$

It is helpful to define the "change-of-basis" matrix in reciprocal space as well, namely

$$\bar{\mathbf{B}} = \begin{pmatrix} b_{1,x} & b_{2,x} & b_{3,x} \\ b_{1,y} & b_{2,y} & b_{3,y} \\ b_{1,z} & b_{2,z} & b_{3,z} \end{pmatrix}, \tag{3.27}$$

since $\bar{\mathbf{A}}$ and $\bar{\mathbf{B}}$ are related as $2\pi\bar{\mathbf{A}}^{-1} = \bar{\mathbf{B}}^{\mathrm{T}}$. Notably, any symmetry operation in real space corresponds to an equal operation in reciprocal space, which is important moving forward.

Now, as hinted in Section 3.2.2, the evaluation of matrix elements include the computation of density-matrix elements in real space, namely $\rho_{ik}(\mathbf{r}_1) = \sum_{\sigma=\uparrow,\downarrow} u_i^*(1)u_k(1)$. Clearly, there are many cases where the corresponding k-vectors, $\mathbf{k}_i$ and $\mathbf{k}_k$, do not originate from the IBZ, which necessitates being able to unfold u_i and u_k on the fly. This requires identifying the particular k-point in the IBZ, $\boldsymbol{\kappa}_i$, from which the corresponding $\mathbf{k}_i$ originates, as well as the symmetry operation, $\bar{\mathbf{S}}_i$, used for unfolding. Additionally, since the wavefunctions are spinors, their spin components also undergo rotation during the unfolding process. This behavior is governed by the spin rotation operator for spin-$\frac{1}{2}$ particles,

$$\mathcal{S}(\theta, \mathbf{u}) = \exp\left(-i\frac{\theta}{2}\mathbf{u}\cdot\boldsymbol{\sigma}\right). \tag{3.28}$$

Here, $\boldsymbol{\sigma}$ is a vector of the Pauli matrices. To ease the expression of $\mathcal{S}(\theta, \mathbf{u})$, the exponential can be expanded, while keeping in mind that $(\mathbf{u}\cdot\boldsymbol{\sigma})^{2n} = \bar{\mathbb{1}}$ and $(\mathbf{u}\cdot\boldsymbol{\sigma})^{2n+1} = \mathbf{u}\cdot\boldsymbol{\sigma}$. This leads to

$$\mathcal{S}(\theta, \mathbf{u}) = \bar{\mathbb{1}}\cos\frac{\theta}{2} - i\mathbf{u}\cdot\boldsymbol{\sigma}\sin\frac{\theta}{2}. \tag{3.29}$$

Thus, to unfold the wavefunctions of $\mathbf{k}_i$ originating from those of $\boldsymbol{\kappa}_i$, the relation is

$$u_{\mathbf{k}_i}(\bar{\mathbf{S}}_i\,\mathbf{r}) = \mathcal{S}(\theta_i, \mathbf{u}_i)\,u_{\boldsymbol{\kappa}_i}(\mathbf{r}), \tag{3.30}$$

or alternatively

$$u_{\mathbf{k}_i}(\mathbf{r}) = \mathcal{S}(\theta_i, \mathbf{u}_i)\,u_{\boldsymbol{\kappa}_i}(\bar{\mathbf{S}}_i^{-1}\,\mathbf{r}). \tag{3.31}$$

The expression seen in Eq. (3.31) dictates a recipe for unfolding wavefunctions on the fly. By keeping $u_{\boldsymbol{\kappa}_i}$ in memory for all k-points within the IBZ in combination with an array of indexes mapping $\bar{\mathbf{S}}_i^{-1}\,\mathbf{r}$ for each symmetry, the memory is vastly reduced compared to storing $u_{\mathbf{k}_i}$ for the entire BZ. Moreover, the unfolding procedure outlined in Eq. (3.31) does not constitute a significant computational bottleneck when compared to the FFT operations involved in Eqs. (3.20) and (3.21).

As mentioned, $\epsilon^{-1}_{\mathrm{GG}'}(\mathbf{q})$ is also only stored for q-points within the IBZ, and, by extension, so is $W_{\mathrm{GG}'}(\mathbf{q})$. However, in Eq. (3.21), $\mathbf{q}_{ik}$ does not necessarily lie within

the IBZ, and unfolding $W_{GG'}(\mathbf{q})$ to match the symmetry of $\mathbf{q}_{ik}$ is complicated due to its multi-coordinate nature. Therefore, instead of unfolding $W_{GG'}(\mathbf{q})$ to match ρ_{lj} and ρ_{ik}, it is much easier to simply fold ρ_{lj} and ρ_{ik} such that $\mathbf{q}_{ik}$ maps back into the IBZ, which, by arguments of symmetry, should give the same result. For clarity, $\mathbf{q}_{ik}$ can be described as

$$\mathbf{q}_{ik} = \bar{\mathbf{S}}_{ik}\mathbf{q}_{ik}^{\mathrm{IBZ}} + \mathbf{G}_f, \tag{3.32}$$

where $\mathbf{q}_{ik}^{\mathrm{IBZ}}$ denotes the q-point in the IBZ from which $\mathbf{q}_{ik}$ originates with corresponding symmetry $\bar{\mathbf{S}}_{ik}$. $\mathbf{G}_f$ represents a "folding" $\mathbf{G}$-vector potentially needed to ensure that $\mathbf{q}_{ik}$ matches with the symmetry-generated full set of $\mathbf{q}$-points. All these quantities are illustrated in Fig. 3.4(a,b). With this in mind, ρ_{ik} can be folded

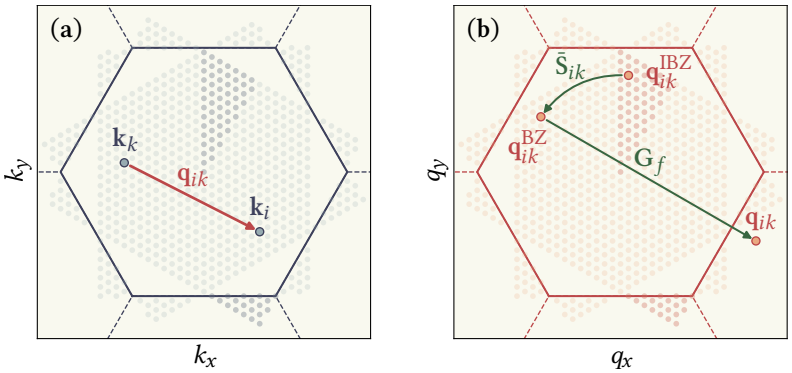

Figure 3.4: (a) Two $\mathbf{k}$-points, $\mathbf{k}_i$ and $\mathbf{k}_k$, in $\mathbf{k}$-space and the difference of these two, $\mathbf{q}_{ik}$. The BZ is marked by a solid blue line, while both the $\mathbf{k}$-points of the IBZ (faint dark blue) and the full set of $\mathbf{k}$-points (faint light blue) are marked. (b) Similar to (a), but in $\mathbf{q}$-space (red). Here, $\mathbf{q}_{ik}$ is connected to to $\mathbf{q}_{ik}^{\mathrm{BZ}}$ via $\mathbf{G}_f$ (green), while $\mathbf{q}_{ik}^{\mathrm{BZ}}$ is connected to $\mathbf{q}_{ik}^{\mathrm{IBZ}}$ by the symmetry $\bar{\mathbf{S}}_{ik}$ (green).

to match the Coulomb kernel, $W_{GG'}(\mathbf{q})$, as

$$\rho_{ik}^{\mathrm{IBZ}}(\mathbf{G}) = \rho_{ik}(\bar{\mathbf{S}}_{ik}\mathbf{G} + \mathbf{G}_f), \tag{3.33}$$

where ρ_{ik}^{IBZ} denotes the folded equivalent of ρ_{ik}. Similar to the wavefunction unfolding, this is done on the fly. It's worth mentioning that the unscreened matrix elements seen in Eq. (3.20), are not required to undergo this procedure, since the kernel, $v_G(\mathbf{q})$, remains unchanged under symmetry operations.

3.3 The CI Procedure

This section outlines the key steps involved in the CI procedure, beginning with the construction of the configurational space, which is crucial for managing the computational complexity. The criteria and constraints that reduce the number of configurations are discussed, such as momentum conservation and localization effects, which makes CI computations feasible for 2D systems. Finally, the methods used to diagonalize the resulting matrix are presented, highlighting the importance of employing optimized algorithms and libraries tailored to the size and sparsity of the CI matrices encountered.

3.3.1 Building Configurations

As suggested in Section 2.3.3, the many-body Hamiltonian in this work is truncated to match configurations built within a certain subspace of EDs. For excitons, this subspace consists of configurations of the form $|i\alpha\rangle = \hat{a}_i^\dagger \hat{b}_\alpha^\dagger |\Omega\rangle$, corresponding to EDs with a single electron-hole pair excited. Similarly, for negatively charged excitons (negative trions), these configurations are $|ij\alpha\rangle = \hat{a}_i^\dagger \hat{a}_j^\dagger \hat{b}_\alpha^\dagger |\Omega\rangle$, and so on. However, a typical DFT calculation often includes many k-points, and most often, quite dense k-meshes are needed to converge excited state energies, e.g. 30×30 k-points or more. Even if just a single conduction and valence band is included in the configurational space, this would suggest $(30^2)^4 = 810000$ possible configurations just in the exciton subspace of EDs. Fortunately, the matrix elements are subject to momentum conservation, and the configurations are restricted to $\mathbf{k}_i - \mathbf{k}_\alpha = \mathbf{Q}_{\text{COM}}$, where $\mathbf{Q}_{\text{COM}}$ is the center-of-mass momentum for the many-body compound, in this case an exciton. Essentially, the momentum constraint removes one degree of freedom. This vastly reduces the number of configurations, and by extension, the number of matrix elements and the final size of the eigenvalue problem. In the previous example, the number of included configurations is reduced to $30^2 = 900$. The center-of-mass momentum restriction can be expressed in a more general fashion by saying that all configurations within a given subspace of EDs must satisfy

$$\sum_i^{n_e} \mathbf{k}_i - \sum_\alpha^{n_h} \mathbf{k}_\alpha = \mathbf{Q}_{\text{COM}}, \tag{3.34}$$

where n_e and n_h denote the numbers of excited electrons and holes in the chosen subspace of EDs, respectively. Typically, for excitonic species at low temperatures $\mathbf{Q}_{\text{COM}} = 0$.

Although Eq. (3.34) severely restricts the number of possible configuration within a given subspace of EDs, numerous configurations still remain within certain subspaces. As an example, the subspace of EDs for negative trions including two valence bands, four conduction bands and 39×39 k-points, features $\approx \frac{1}{2} \cdot 2 \cdot 4^2 \cdot (39^2)^2 \approx 3.7 \cdot 10^7$ configurations, where the $\frac{1}{2}$ serves to avoid double counting. However, the states of interest often localize around around particular high-symmetry points in k-space, which can be exploited to significantly reduce the configurational space. An example of this can be seen in Fig. 3.5(a), which shows the exciton ground state of monolayer WSSe in k-space for a 39×39 k-mesh. The exciton wavefunction is of the form

$$|\mathrm{X}\rangle = \sum_{i\alpha} A_{i\alpha} |i\alpha\rangle, \tag{3.35}$$

where $A_{i\alpha}$ are the (complex) excitonic wavefunction coefficients. The weights shown in Fig. 3.5(a) are defined as $w_k(\mathbf{k}) = \sum_{i\alpha} |A_{i\alpha}|^2 \delta_{\mathbf{k},\mathbf{k}_i}$, which is a projection of the wavefunction coefficients onto the k-mesh, adding all band contributions. However, as revealed in the inset of Fig. 3.5(a), the wavefunction is strongly localized around $\mathbf{K}$ and $\mathbf{K}'$, and therefore, it is often sufficient to employ a reduced k-mesh as seen in Fig. 3.5(b). Naturally, this depends on the state of interest, while the radius is a parameter that must be converged. Going back to the negative

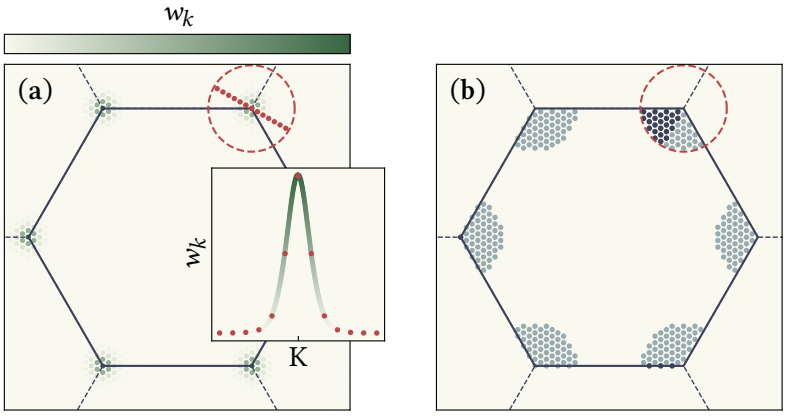

Figure 3.5: (a) Configurational weights for the excitonic ground state of monolayer WSSe projected onto the k-points. The weight magnitude is indicated by the colorbar, where green corresponds to large configurational weight. The dashed red circle corresponds to a radius of 0.2 Bohr^{-1} around the K-point, and inside some k-points are marked in red. In the inset, w_k is plotted along these k-points, and are further interpolated for easier visualization. (b) A reduced k-mesh capable of replicating the state in (a).

trion example, the reduced k-mesh seen in Fig. 3.5(b) features only 302 k-points as opposed to the 1521 k-points from the full BZ, which in turn reduces the number of configurations to $\approx \frac{1}{2} \cdot 2 \cdot 4^2 \cdot (302)^2 \approx 1.4 \cdot 10^6$ - almost by a factor 20.

Another important selection rule employed within the presented methodology are the Slater-Condon rules. Essentially, if more than two spin-orbitals differ between two EDs, the resultant matrix element of a two-body operator between said states vanishes. For excitons, which are built in the configurational space of EDs with only two spin-orbitals differing from $|\Omega\rangle$, the rules clearly provide no advantage. However, for anything beyond the exciton, such as trions and biexcitons, the rules enable a much faster determination of whether a given matrix element is non-zero, compared to explicitly evaluating the creation and annihilation operators seen in (2.25). Moreover, and as a consequence, the resulting matrix is typically very sparse for excitations above the exciton level - for trions, often more than 99%.

Once the configurational space and the non-zero entries of the CI matrix are known, the many-body Hamiltonian of Eq. (2.43) is employed to determine which two-body interactions each matrix element allocates. While this could be manually evaluated for each excitation level, such an approach is cumbersome and prone to errors. Instead, in this work - and within the `MX`-package in general - second quantization is used, which bypasses the need to so. This framework can, in principle, handle any level of excitation, though practical limitations arise from how the number of configurations and matrix elements scale with the number of k-points.

3.3.2 Diagonalization

The final step of the CI procedure is diagonalization of the CI matrix. In the 2D systems presented in this work, these matrices are often of significant size, due to the extensive configurational space introduced by the incorporation of k-points.

Consequently, it is essential to utilize specialized libraries and solvers optimized for efficient and accurate diagonalization of large-scale matrices. As mentioned in the previous section, the matrix elements between excitonic configurations always result in non-zero values by the Slater-Condon rules, meaning that a dense diagonalization scheme should be employed. To this end, the ScaLAPACK and BLACS libraries [76] have been implemented, offering the advantage of parallel execution. This is particularly advantageous when handling large dense matrices, where limited non-distributed memory can become a bottleneck, impacting both computational time and resource efficiency.

For exicted states beyond the exciton, the CI matrix is, however, exceptionally sparse, which calls for a sparse solver. For this purpose, the PETSc/SLEPc suite [77–80] has been implemented, which, much like before, also allows for parallel execution. However, in this case it is neither realistic nor desirable to obtain all eigenvalues and eigenvectors. Fortunately, a keyword can be fed to the solver to only obtain a limited number of states, optionally sorted from lowest to highest energy.

3.4 Post-processing

Obtaining the many-body states through diagonalization gives a set of energies and wavefunction coefficients, which must be analyzed to obtain meaningful results. A key tool when examining the optical properties is the absorption spectrum, which gives a concise overview of the brightness and, to some extent, the density of the excited states. Then, for the states of interest it is often interesting to look at their distribution both in real space and reciprocal space, as in 3.5(a). In the following, both of these methods are described in more detail.

3.4.1 Absorption

Absorption is the process of an initial (many-body) state absorbing a photon, which, for some frequencies, creates an additional electron-hole pair. This pair then renders the final state at one excitation level higher than the initial one. Thus, the absorption spectrum is essentially a collection of information about which final states are more likely to be created by the exciting photon. To this extent, Fermi's golden rule proves an excellent starting point, with an expression of the form

$$\alpha(\omega) \propto \sum_{\lambda} |\langle \mathrm{X}^{m-1}|\hat{\boldsymbol{\mathcal{E}}} \cdot \mathbf{r}|\mathrm{X}^{m}_{\lambda}\rangle|^2 \delta(E^{m}_{\lambda} - E^{m-1} - \hbar\omega), \tag{3.36}$$

where $|\mathrm{X}^{m-1}\rangle$ and $|\mathrm{X}^{m}_{\lambda}\rangle$ are the initial and final states, respectively, with corresponding energies E^{m-1} and E^{m}_{λ}. The transition is subject to conservation of momentum, and therefore $\mathbf{Q}_{\mathrm{COM}}$ must be equal for both states to have a non-vanishing contribution. Likewise, the transition also follows conservation of energy, which is governed by the Dirac delta function, that includes the photon energy, $\hbar\omega$. The interaction Hamiltonian, $\hat{\boldsymbol{\mathcal{E}}} \cdot \mathbf{r}$, describes the light-matter coupling in the dipole approximation, and governs optical transitions between the initial

and final state(s). It consists of the polarization direction of the photon, $\hat{\boldsymbol{\mathcal{E}}}$, and the transition dipole moment, $\mathbf{r}$, where the latter is given in second quantization as

$$\mathbf{r} = \sum_{i\alpha} \langle \alpha|\mathbf{r}|i\rangle \, \hat{b}_\alpha \hat{a}_i, \tag{3.37}$$

emphasizing that the initial and final states differ by exactly one electron-hole pair. Furthermore, due to momentum conservation $\langle \alpha|\mathbf{r}|i\rangle = 0$ if $\mathbf{k}_i \neq \mathbf{k}_\alpha$. Now, the dipole matrix elements $\langle \alpha|\mathbf{r}|i\rangle$ are computed from the Kohn-Sham states using the momentum operator, $\mathbf{p}$, since

$$\langle \alpha|\mathbf{r}|i\rangle = \frac{i}{(\epsilon_i - \epsilon_\alpha)} \langle \alpha|\mathbf{p}|i\rangle \,, \tag{3.38}$$

where ϵ_i and ϵ_α are the corresponding Kohn-Sham energies. Similar to the CI matrix elements, the Kohn-Sham dipole matrix elements are also computed only within the IBZ, from which the dipole matrix elements of the entire BZ may be unfolded using symmetry operations.

To highlight the implementation of Eq. (3.36), one may consider the process of biexciton generation, which can occur when an exciton absorbs a photon. In this case, $|\mathrm{X}^{m-1}\rangle = \sum_{i\alpha} A_{i\alpha} \hat{a}_i^\dagger \hat{b}_\alpha^\dagger |\Omega\rangle$ and $|\mathrm{X}^{m}\rangle = \sum_{kl\gamma\lambda} A_{pq\mu\nu} \hat{a}_k^\dagger \hat{a}_l^\dagger \hat{b}_\gamma^\dagger \hat{b}_\lambda^\dagger |\Omega\rangle$, which leads to dipole matrix elements of the form

$$\begin{aligned}
\langle \mathrm{X}^{m-1}|\mathbf{r}|\mathrm{X}^{m}\rangle &= \sum_{j\beta} \sum_{i\alpha} \sum_{kl\gamma\lambda} A^*_{i\alpha} A_{kl\gamma\lambda} \mathbf{r}_{\beta j} \langle \Omega| \, \hat{b}_\alpha \hat{a}_i \hat{b}_\beta \hat{a}_j \hat{a}_k^\dagger \hat{a}_l^\dagger \hat{b}_\gamma^\dagger \hat{b}_\lambda^\dagger \, |\Omega\rangle \\
&= \sum_{i\alpha} \sum_{kl\gamma\lambda} A^*_{i\alpha} A_{kl\gamma\lambda} \Big(\mathbf{r}_{\gamma k} \delta_{\alpha\lambda} \delta_{il} - \mathbf{r}_{\gamma l} \delta_{\alpha\lambda} \delta_{ik} - \mathbf{r}_{\lambda k} \delta_{\alpha\gamma} \delta_{il} + \mathbf{r}_{\lambda l} \delta_{\alpha\gamma} \delta_{ik} \Big).
\end{aligned} \tag{3.39}$$

Here, the short-hand notation $r_{i\alpha} = \langle \alpha|\mathbf{r}|i\rangle$ has been used. Clearly, the above expression is quite involved, however, in the code that computes dipole matrix elements, the signs and Dirac delta functions are computed implicitly through second quantization, instead of explicitly deriving the formula for each excitation level. Lastly, as seen in Eq. (3.36), $\hat{\boldsymbol{\mathcal{E}}}$ can be polarized along each of the cartesian directions or any linear combination thereof. Since the materials discussed here are isotropic along the cartesian x- and y-axes, the absorption is calculated as

$$\alpha_{xy}(\omega) \propto \sum_\lambda \frac{|\langle \mathrm{X}^{m-1}|\mathbf{r}_x|\mathrm{X}^m_\lambda\rangle|^2 + |\langle \mathrm{X}^{m-1}|\mathbf{r}_y|\mathrm{X}^m_\lambda\rangle|^2}{2} \delta(E^m_\lambda - E^{m-1} - \hbar\omega), \tag{3.40}$$

which can be interpreted as the in-plane absorption. In practice, the Dirac-delta distribution is unrealistic and typically absorption peaks feature significant broadening. To account for this, the spectra shown within this thesis instead feature a phenomenological Lorentzian broadening, such that

$$\alpha_{xy}(\omega) \propto \sum_\lambda \mathfrak{Im} \left\{ \frac{1}{2} \frac{|\langle \mathrm{X}^{m-1}|\mathbf{r}_x|\mathrm{X}^m_\lambda\rangle|^2 + |\langle \mathrm{X}^{m-1}|\mathbf{r}_y|\mathrm{X}^m_\lambda\rangle|^2}{E^m_\lambda - E^{m-1} - \hbar\omega + i\hbar\Gamma} \right\}, \tag{3.41}$$

where Γ determines the broadening.

3.4.2 Many-body Wavefunctions

As mentioned, another important tool is the visualization of excited state wavefunctions. For monolayers, it reveals the in-plane distribution and extend, while for bilayers, it helps identify in which layer(s) the constituent particles localize. As a first step, the exciton wave function can be considered, that is

$$|\mathrm{X}\rangle = \sum_{i\alpha} A_{i\alpha}\varphi_i(\mathbf{r}_{e_1})\varphi^*_\alpha(\mathbf{r}_{h_1}), \tag{3.42}$$

where $\mathbf{r}_{e_1}$ and $\mathbf{r}_{h_1}$ are the electron and hole coordinates, respectively. However, the quantity of interest here is the density, which has corresponding operator

$$\hat{\rho} = \delta(\mathbf{r}_{e_1} - \mathbf{r}_1)\delta(\mathbf{r}_{h_1} - \mathbf{r}_2). \tag{3.43}$$

The density operator positions the electron at $\mathbf{r}_1$ and the hole at $\mathbf{r}_2$. Typically, $\mathbf{r}_1$ is varied while $\mathbf{r}_2$ is fixed, or vice versa, since plotting or computing a function depending on six spatial coordinates is impractical. Applying this operator and, without loss of generality, letting $\mathbf{r}_2$ be fixed, the electronic part of the exciton density is computed as

$$\rho_e(\mathbf{r}_1) = \langle \mathrm{X}|\,\hat{\rho}\,|\mathrm{X}\rangle = \Big|\sum_{i\alpha} A_{i\alpha}\varphi_i(\mathbf{r}_1)\varphi^*_\alpha(\mathbf{r}_2)\Big|^2. \tag{3.44}$$

Analogously, the density of the hole, $\rho_h(\mathbf{r}_2)$, could have been evaluated. The expression is, however, not straightforward to evaluate, since the exciton typically is not confined to a single unit cell. In Fig. 3.6, both ρ_e and ρ_h are plotted for monolayer WSSe, and indeed, the density spans multiple unit cells. As such, the

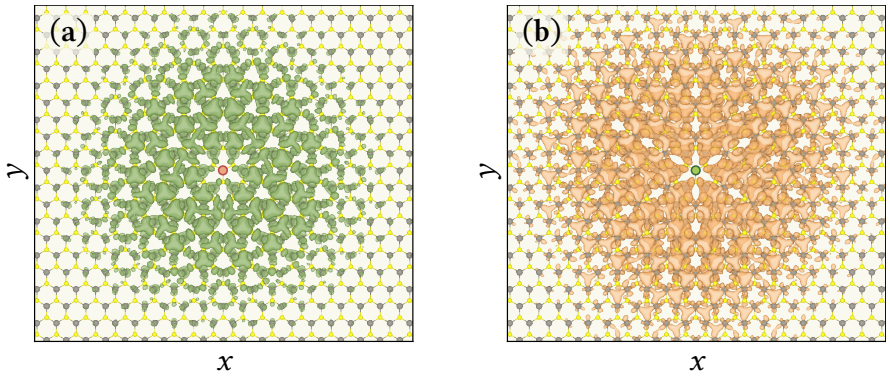

Figure 3.6: (a) The electronic part of the excitonic density, ρ_e, for the exciton ground state of monolayer WSSe shown in green with the hole fixed at the orange dot in the center of the image. The background shows the lattice. (b) Similar to (a), but with the hole part of the density shown in orange and the electron fixed at the green dot. In both (a) and (b) the isosurface value is set to 10^{-10} for the density.

evaluation of e.g. ρ_e should reflect this behavior, and in Fig. 3.6, ρ_e is evaluated for $\mathbf{r}_1$ spanning 31×31 unit cells.

Proceeding to higher excited states, such as negative trions, the wavefunction is given as

$$\begin{aligned} |\mathrm{X}^-\rangle &= \frac{1}{\sqrt{2}} \sum_{ij\alpha} A_{ij\alpha} \Big\{ \varphi_i(\mathbf{r}_{e_1}) \varphi_j(\mathbf{r}_{e_2}) - \varphi_j(\mathbf{r}_{e_1}) \varphi_i(\mathbf{r}_{e_2}) \Big\} \varphi_\alpha^*(\mathbf{r}_{h_1}) \\ &= \frac{1}{\sqrt{2}} \sum_{i<j,\alpha} \Big\{ A_{ij\alpha} - A_{ji\alpha} \Big\} \varphi_i(\mathbf{r}_{e_1}) \varphi_j(\mathbf{r}_{e_2}) \varphi_\alpha^*(\mathbf{r}_{h_1}). \end{aligned} \tag{3.45}$$

In this case, a similar procedure to the exciton can be used, where one particle is fixed and another is plotted. The remaining particle is then simply averaged out. This can be achieved with an operator identical to that of Eq. (3.43), which fixes/plots the hole while plotting/fixing one of the electrons, leading to an expression of the form

$$\langle \mathrm{X}^- | \, \hat{\rho} \, | \mathrm{X}^- \rangle = \sum_j \Big| \sum_{i\alpha} \Big\{ A^\lambda_{ij\alpha} - A^\lambda_{ji\alpha} \Big\} \varphi_i(\mathbf{r}_1) \varphi_\alpha^*(\mathbf{r}_2) \Big|^2 \tag{3.46}$$

Alternatively, for this excitation level, an operator that puts one electron at position $\mathbf{r}_1$ and another electron at position $\mathbf{r}_2$ while the hole is averaged out could be employed. For even higher orders of excitation, the process is analogous except multiple particles would need to be averaged out. Clearly, the signs between the different permutations of wavefunction products seen in Eq. (3.45) get increasingly more complicated with the number of excited particles. However, as for absorption, this is handled implicitly, instead of explicitly finding an expression for each excitation level.

4 Results

As this work is a cumulative thesis, key publications have been chosen from peer-reviewed magazines to be presented here. To enhance understanding, each of the three included manuscripts are preceded by a brief introduction. The first publication focuses on excitons and trions in monolayer WSe_2, providing a foundational understanding of excited state properties in TMDs. The second publication is of similar nature, and explores interlayer excited states in bilayer Janus MoSSe-WSSe, offering insights into more complex bilayer systems. The third and final publication addresses atomic relaxation effects in bilayer TMD moiré heterostructures. This work aims to establish a prerequisite setup for relaxing large moiré-structured systems, which will serve as a basis for subsequent CI calculations in such structures. While these results are beyond the scope of this thesis, the developed framework lays the baseline for future research in this direction.

Contents

4.1 [E1] Exciton and Trion Fine-structure of Monolayer WSe_2

Monolayer TMDs, such as WSe_2, have garnered considerable attention due to their remarkable optical and electronic properties, including sizable band gaps, substantial spin-orbit coupling, and robust light-matter interactions. While many previous studies have predominantly focused on direct optical transitions occur-

ring at the high-symmetry **K**-point [81–89], experimental and theoretical data indicate that, for WSe_2, the electronic band structure is more intricate [43, 44]. Specifically, the conduction band minimum (CBM) is situated in the **Q**-valley, located approximately halfway between **Γ** and **K**, as seen in Fig. 4.1(a). This

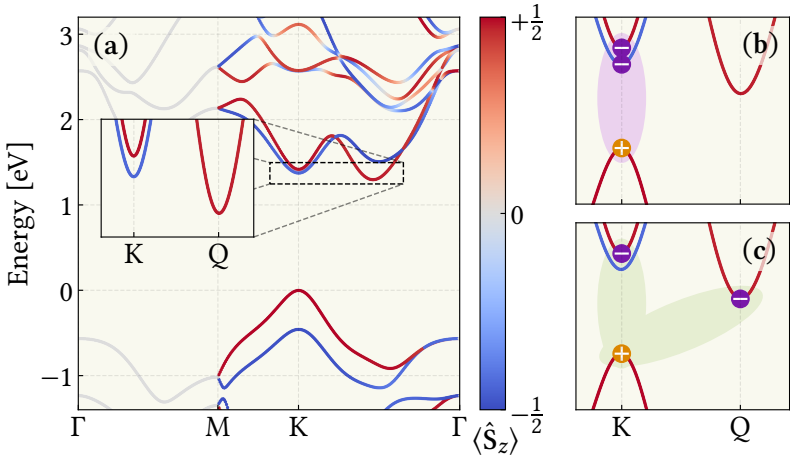

Figure 4.1: (a) The band structure of monolayer WSe_2 at the PBE level. The spin projection is encoded in the color of the bands. (b) Conventional negatively charged trion species centered around **K** (purple), where electrons are marked as purple dots, while holes are indicated by orange dots. (c) Similar to (a), but for proposed trion species with a carrier located at **Q** (green).

peculiarity implies that at low temperatures carriers populate the **Q**-valley prior to **K**. Thus, the low-energy excited states should involve carriers residing in both the **K**- and **Q**-valleys, influencing the formation and energetic ordering of excitons and trions. An example of this idea is depicted in Fig. 4.1(b,c), highlighting both the conventional **K**-centered negatively charged trions, and the proposed negatively charged trion species with a carrier located at **Q**. In light of this, the following work is the first to reveal the detailed fine-structure of negatively charged trion species involving the **Q**-valley. Here, it is demonstrated how this multi-valley configuration gives rise to distinct trion species that are energetically more favorable than their conventional **K**-centered counterparts. Notably, these **Q**-valley trions exhibit a larger singlet-triplet splitting and a systematic redshift in their energies, which is attributed to stronger electron-hole exchange interactions enhanced by reduced spin polarization at **Q**. Although the underlying mechanisms are complex, they are comprehensively described through the CI approach outlined in Chapter 3. Furthermore, as a possible consequence, when the system thermalizes, these trion species may have implications for the population and performance of trion species excited only within the **K**-valley. This fundamental investigation opens new avenues for understanding valley-dependent phenomena and potential device applications in valleytronics, where valley degrees of freedom are exploited.

Related Supplementary Information can be found in Section B.1.

npj | 2D materials and applications

Article

Published in partnership with FCT NOVA with the support of E-MRS

https://doi.org/10.1038/s41699-025-00532-w

Beyond the K-valley: exploring unique trion states in indirect band gap monolayer WSe_2

Carl Emil Mørch Nielsen[1,4], Franz Fischer[1,2,4] & Gabriel Bester[1,3] ✉

We calculate the optical properties of monolayer WSe_2 using ab initio many-body screened configuration interaction. For this indirect band gap material we describe additional species of negatively charged trions involving the **Q**-valley which are energetically more favorable than those formed at the **K**-valley. While the results are in excellent agreement with experimental data, they shed new light on observed but yet unaddressed optical features. The analysis of the many-body interactions reveals mechanisms behind increased singlet-triplet splitting and redshifted energies in these **Q**-valley trions, compared to **K**-valley trions.

Extensive research is currently focused on two-dimensional (2D) systems due to their favorable physical characteristics, including substantial band gaps, large spin-orbit coupling (SOC) effects, and strong light-matter interaction[1–4]. Additionally, the tunability of electronic and optical properties via external fields, strain, stacking, and twisting makes 2D materials an interesting playground for theoretical and experimental studies[5–9]. The reduced dimensionality of these systems results in unconventional screening of the Coulomb interaction, thereby generating strongly bound neutral and charged excitons[10–13]. One of the most renowned groups of 2D materials are layered transition metal dichalcogenides (TMDs) with significant potential for future applications[14,15]. TMDs can be represented as MX_2 where M = (Mo, W) and X = (S, Se, Te) and crystallize in the hexagonal 2H-phase crystal phase. Upon exfoliation to a single layer, most TMDs undergo an indirect-to-direct semiconductor transition, resulting in a direct optical gap at the **K**-valley[16–18]. Thus, many previous experimental and theoretical studies on optically excited states in monolayer TMDs rely on explanations based solely on the **K**-valley to account for the prominent spectral features of absorption and photoluminescence (PL)[19–27]. While this assumption may hold true for most TMDs, compelling data, both experimental and theoretical, indicates the presence of an indirect band gap for atomically-thin WSe_2[28–33]. Whereas the valence band maximum (VBM) remains situated at **K**, the conduction band minimum (CBM) is found at the **Q**-valley, halfway along the Γ-K direction[29,31,32] (see Fig. 1). As such, an additional electron would preferentially localize at **Q** rather than **K** for low temperatures, which impacts the compositions and energies of low-energy negative trions. Absorption and PL spectra on WSe_2 reveal a distinctive two-peak structure for negatively-charged trions[21,22,24–26,34–40]. The prevailing belief is that these originate from configurations of electrons and holes located near **K**/**K**' (denoted X_K^-).

We show that monolayer WSe_2 hosts negative trion species with a total center-of-mass momentum $\mathbf{Q}_{COM} = \mathbf{Q}$ (denoted X_Q^-), where one carrier is located at **Q**, as recently suggested by Perea-Causin et al.[41] based on effective mass (eff. mass) calculations. We find that X_Q^- and X_K^- produce similar absorption features, with X_Q^- energies slightly red-shifted relative to those of X_K^-. Additionally, we find singlet-triplet ordering for both trion species and reveal the relevant mechanisms for the trion fine-structure splitting beyond independent-particle (IP) effects. Our insights into WSe_2 trion species not only impact the fundamental understanding of excitonic physics but also bear practical applications in optoelectronics. Specifically, the emerging field of valleytronics, where one seeks to exploit the electron's valley degree of freedom (e.g., in valley-based transistors and switches, where information can be encoded in the valley degree of freedom, photodetectors and light-emitting devices that leverage valley polarization, or even quantum computing components, where valleys can serve as qubits), may profit from this type of excitation.

Results

Figure 1a shows the DFT-relaxed crystal structure of monolayer WSe_2, and the corresponding electronic structure is depicted in Fig. 1c, where we find an energetic offset in the lowest conduction band between **Q** and **K** of 82 meV. The SOC induced spin-splitting in the valence band is computed to be ~455 meV[42], an order of magnitude larger than the SOC-induced conduction band splitting (CBS) of 44 meV. Our calculations overestimate the CBS at **K**, which is experimentally observed to be 10–15 meV[27,43], prompting us to manually adjust the splitting to 10 meV.

[1]Institute of Physical Chemistry, University of Hamburg, Hamburg, Germany. [2]Max Planck Institute for the Structure and Dynamics of Matter, Hamburg, Germany. [3]The Hamburg Centre for Ultrafast Imaging, Hamburg, Germany. [4]These authors contributed equally: Carl Emil Mørch Nielsen, Franz Fischer.
✉e-mail: gabriel.bester@uni-hamburg.de

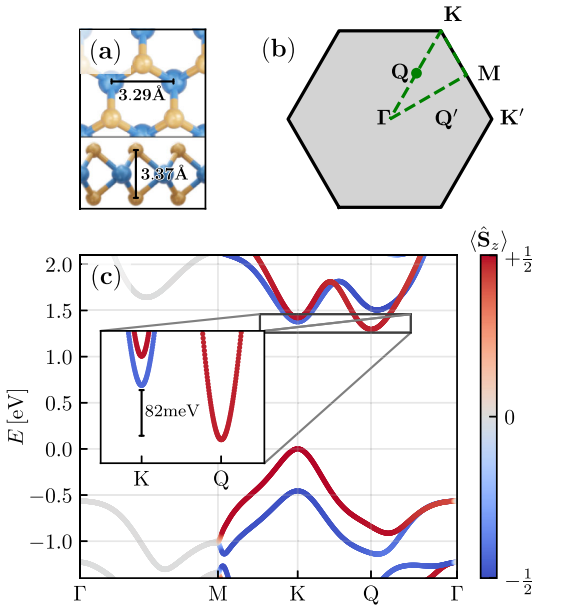

Fig. 1 | Unit cell and bandstructure of monolayer WSe_2. a WSe_2 in top and side view with the in-plane lattice constant and Se − Se distance. **b** The first Brillouin zone with the prominent high-symmetry points and corresponding **k**-path (green) as used in **c** the bandstructure computed within DFT. The color indicates the spin expectation value along *z*. The inset shows the energy difference of the conduction band at **K** and **Q**.

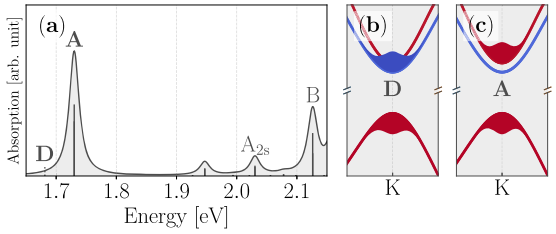

Fig. 2 | Low-energy excitonic states. a Absorption spectrum for X using a phenomenological broadening of 10 meV. **b**, **c** Configurational weights displayed on the bands near **K** of states D and A, respectively.

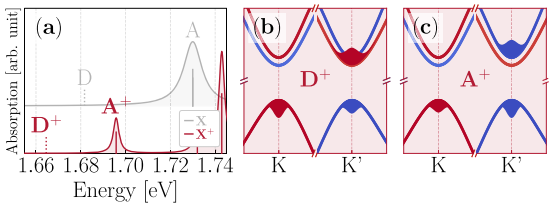

Fig. 3 | Low-energy positively charged trions centered around K. a Absorption spectrum for X^+ and X (offset along the *y*-axis) in red and grey, respectively. A phenomenological broadening of 1.5 meV has been used for the trions. **b**, **c** Configurational weights near **K** and **K'** for states D^+ and A^+.

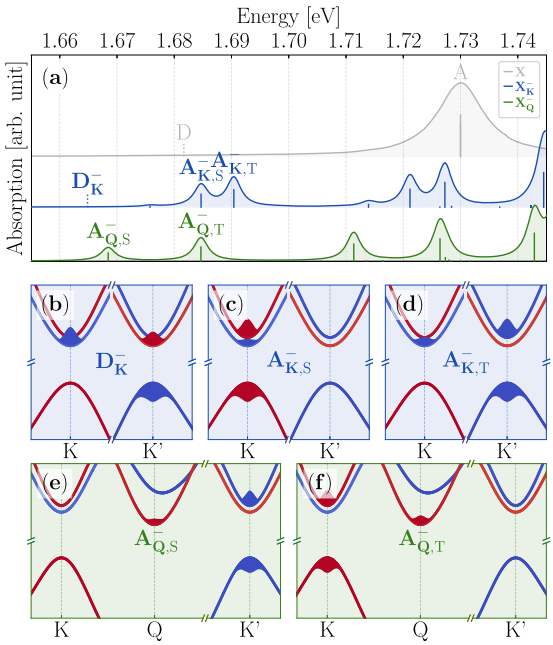

Fig. 4 | The two species of low-energy negatively charged trions. a Absorption spectrum for X (grey), X^-_K (blue) and X^-_Q (green). The spectra are shifted for better comparison. A phenomenological broadening of 1.5 meV has been used for the trions. Configurational weights for X^-_K (**b**–**d**) and X^-_Q (**e**, **f**), where the weight on **Q** is scaled by 1.5 for better visibility.

Excitons

In Fig. 2a the absorption spectrum of excitons (X, $\mathbf{Q}_{COM} = 0$) is displayed, where the entire spectrum is shifted so that the first bright exciton, A (see Fig. 2c), is located at the experimental value of 1.73 eV[21,24–26,34,39]. Three optically-active bound excitons, denoted as A, A_{2s}, and B[44], can be identified, with a predicted binding energy of 480 meV for the A exciton. We further observe a bright state close to the A_{2s} transition (see Supplementary Information (SI)). All reported values are found by extrapolating to infinitely dense *k*-samplings in order to ensure high accuracy. The splitting between the A and B excitons (here 388 meV) arises mainly due to SOC splittings of the valence and conduction bands, consistent with reported experimental values (380 meV[39]). Furthermore, we indicate the lowest exciton in the spectrum with D, which is a spin-dark state located 49 meV below the A exciton as seen in Fig. 2b. We isolate the dominant contributor to the D-A splitting to be the coupling between configurations, making it almost five times larger than the CBS.

Positively charged trions

For positively charged trions (X^+) the spectrum in Fig. 3a shows only a single bright resonance, A^+, with a binding energy of 31 meV relative to A, as the VBM splitting is comparably large. A^+ is accompanied by a satellite dark state, D^+, with a dark-bright splitting of 33 meV. As shown in Fig. 3b, c, the positive trions resemble either D or A excitons formed at **K'** plus an additional hole at **K**. Compared to the excitons, the configurational weights are more localized in reciprocal space.

Negatively charged trions

Figure 4a displays the absorption spectra for X^-_K in blue and X^-_Q in green. For X^-_K we identify two bright trion states, $A^-_{K,S}$ and $A^-_{K,T}$, which exhibit binding energies of 43 meV and 37 meV with respect to A. Figure 4c, d reveals that these states resemble a more localized version of the A exciton in reciprocal space with an additional carrier at **K**. $A^-_{K,S}$ is an intra-valley singlet state, with all configurational weight localized near **K**. In contrast, $A^-_{K,S}$ is an inter-valley triplet, where the eh pair localizes at **K'**. In our calculations $A^-_{K,S}$

Table 1 | Comparison of binding energies for excitons and trions from both experiment (Exp.) and theory (Theo.).

	D^+	D^-	D	$A^-_{Q,S}$	$A^-_{Q,T}$	$A^-_{K,S}$	$A^-_{K,T}$	A^+
[27] Exp.	–	15	41	48[a]	–	35	29	–
[45] Exp.	15	16	39	47[a]	–	34	27	20
[24] Exp.	15	16	42	–	–	37	30	24
[25] Exp.	16	14	41	–	–	35	29	21
[26] Exp.	–	–	–	–	–	35	29	–
[20]*GW*-BSE	15	15	80	–	–	62	65	30
[41] Eff. mass	12	12	57	46	–	24	–	11
This work	15	15	49	61	44	43	37	31

The binding energies of bright states ($A^\pm_i$) are relative to A, whereas the binding energy of dark states ($D^\pm_i$) are given with respect to D. All values in units of meV.
[a]Hypothesized peak origin.

appears slightly less optically-active than $A^-_{K,T}$, because $A^-_{K,T}$ has greater configurational weight in the first conduction band at **K**. Furthermore, D^-_K appears dark for the same reasons as D and D^+ as shown in Fig. 4b. It is located ~15 meV below D and 64 meV below A. We emphasize, that both splittings and energetic orderings are in excellent agreement with experimental studies for X^-_K[24–27,35], see Table 1.

So far, results have been limited to excited states localized near **K**/**K**', but Fig. 4a indicates that additional trion species, X^-_Q, appear in the same energetic window.

Similar to X^-_K, we unravel two distinct bright trion species, denoted as $A^-_{Q,S}$ and $A^-_{Q,T}$, with binding energies of 61 meV and 44 meV relative to A, redshifted with respect to X^-_K, in agreement with ref. 41.

The composition and energetic ordering of these states is analogous to those of X^-_K, albeit with a carrier localized at **Q** instead of **K**, which can be seen in Fig. 4e, f. They appear less bright in Fig. 4a since the configurational weight on the dopant electron at **Q** is less pronounced.

Indeed, our findings reveal agreement with experimental results within a few meV for all states of interest displayed in Table 1. Interestingly, Ren et al.[27] and Jindal et al.[45] both report an additional peak ~13 meV below the $A^-_{K,S}$ state. We suggest that this additional peak aligns with our predicted $A^-_{Q,S}$ state found 17 meV below $A^-_{K,S}$. Moreover, the recombination of the $A^-_{K,S}$ and $A^-_{Q,T}$ states within the same valley results in light emission polarized in the same direction, posing a challenge for experimental differentiation due to their similar polarization.

Due to the multi-valley composition of X^-_Q, the classification in intra- and inter-valley trions is not applicable to $A^-_{Q,S}$ and $A^-_{Q,T}$, as opposed to $A^-_{K,S}$ and $A^-_{K,T}$. Instead, the spin character of the constituting carriers hints at what determines the energetic ordering.

Discussion

Despite the similarities between X^-_K and X^-_Q, our results highlight two major differences; (i) X^-_Q are more strongly bound and (ii) the singlet-triplet splitting (STS) for X^-_Q is larger than that of X^-_K. We attribute the lower energies of X^-_Q partially to the slightly larger effective mass of the lowest conduction band at **Q** compared to **K** - in agreement with ref. 41. Artificially adjusting the effective mass of the lowest conduction band at **K** to equal that of **Q** redshifts the bright states of X^-_K by 2 meV. The remaining energy difference is likely due to variations in the coupling strength between the configurations of each species.

To understand the magnitude of the STS, we examine the contributions from the individual terms of the Hamiltonian, illustrated in Fig. 5. At the IP level there is no STS for either trion species. The introduction of diagonal interactions instigates an STS, and the Hamiltonian has four contributions (See SI); the IP energies, eh interaction between the A-like eh pair (black arrows in Fig. 5), eh interaction between the hole and the dopant electron (K^{eh}), and electron-electron (ee) interaction between the two

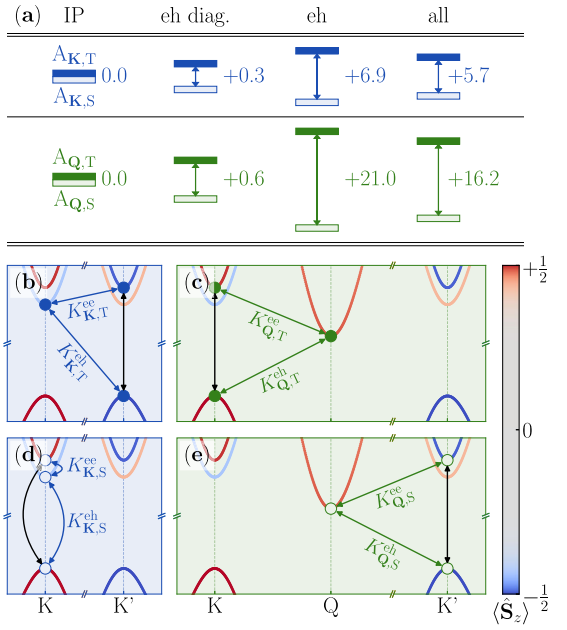

Fig. 5 | Schematic of interactions relevant to the singlet-triplet splitting of negatively charged trions. a Splitting of the singlet (light) and triplet (dark) states for X^-_K (blue) and X^-_Q (green) in meV including successively more interaction terms: only the IP energies, adding only diagonal eh interaction (eh diag.), adding off-diagonal eh interactions (eh), and finally adding electron-electron interactions (all). **b**–**e** Relevant eh exchange coupling elements for the singlet-triplet splitting of X^-_K and X^-_Q. The black arrow indicates the A-like interaction shared by all four configurations. In each figure, the spin expectation value is encoded in the color of the bands.

electrons (K^{ee}), giving rise to an energy of

$$E_\lambda = \epsilon_\lambda + \left(K^{eh}_A - J^{eh}_A\right) + \left(K^{eh}_\lambda - J^{eh}_\lambda\right) - \left(K^{ee}_\lambda - J^{ee}_\lambda\right),$$

where λ is a trion state index and ϵ_λ the corresponding sum of trion state IP energies. Furthermore, J indicate direct Coulomb matrix elements, whereas K denote exchange matrix elements (not to be confused with the reciprocal **K**-point). J^{eh}_A and K^{eh}_A represent the A-like eh interaction between the VBM and the second conduction band at **K**/**K**', which are terms shared by all configurations of interest, marked as black arrows in Fig. 5b–d, f. For X^-_K, the STS is then

$$E_{K,T} - E_{K,S} = \left(K^{eh}_{K,T} - K^{eh}_{K,S}\right) - \left(K^{ee}_{K,T} - K^{ee}_{K,S}\right),$$

revealing that only eh and ee exchange interactions are responsible for the STS, which analogously holds true for X^-_Q. Strong eh exchange interactions occur between states of equal spin. However, the lowermost conduction band at **Q** is more spin-polarized than at **K**. Therefore, $K^{eh}_{Q,T}$, is larger in magnitude than $K^{eh}_{K,T}$, while the opposite holds true for $K^{eh}_{Q,S}$ and $K^{eh}_{K,S}$. In other words,

$$\underbrace{K^{eh}_{Q,T} - K^{eh}_{Q,S}}_{0.6\text{meV}} > \underbrace{K^{eh}_{K,T} - K^{eh}_{K,S}}_{0.3\text{meV}}.$$

Since the true trion states are superpositions of configurations near **K**, **K**' and **Q**, we argue that tendencies observed on the diagonal carry over when allowing for coupling between configurations introduced by off-diagonal

matrix elements. Fig. 5a reveals that allowing for off-diagonal eh interactions magnifies the splittings, while in contrast, the repellent ee exchange interactions decrease the STS, albeit less pronounced due to the screened ee kernel.

Lastly, the IP energy difference between the lowest conduction band at **K** and **Q** is highly sensitive to and as such tunable by strain. For compressive strain we find that the **Q**-valley shifts even further down in energy compared to the **K**-valley, suggesting an enhanced redshift of $X^-_{\mathbf{Q}}$ compared to $X^-_{\mathbf{K}}$. Applying tensile strain has the opposite effect, causing WSe_2 to behave as a direct band gap material at certain levels of strain (see SI for more details). Here, we speculate that $X^-_{\mathbf{K}}$ would dominate the low-energy spectrum[46]. Quantitatively predicting the strain dependent transition between a **Q**- and a **K**-valley dominated low-energy spectrum would be an interesting avenue for future calculations.

In summary, we explored low-energy neutral and charged excitations of monolayer WSe2, incorporating the effects of its indirect band gap in an unprecedented manner. Our analysis reveals remarkable agreement with experimental data for excitons (X) and positively charged trions (X^+), along with the previously established negatively charged trions localized around the **K**-valley ($X^-_{\mathbf{K}}$). However, we identified additional bright negatively charged trions composed of configurations involving the **Q**-valley ($X^-_{\mathbf{Q}}$), exhibiting absorption characteristics similar to $X^-_{\mathbf{K}}$. Despite similarities, we observed a significant enhancement in the STS and a systematic redshift of energy in $X^-_{\mathbf{Q}}$. The increased splitting is quantitatively attributed to strong eh exchange coupling due to the greater spin polarization in the lowermost conduction band at **Q** compared to **K**.

These findings not only resonate with recent experimental and theoretical observations but also emphasize the importance of spin polarization in determining the energetic ordering of these trionic species. Our findings shine a new light on existing measurements but also has important implications for the design of future optoelectronic devices, introducing a new candidate for the field of valleytronics, harnessing the unique properties of valley-dependent phenomena.

Methods

At the core of our method is the parameter-free and truly ab initio effective many-body Hamiltonian $\mathcal{H}$ formulated in the electron-hole (eh) picture[47,48] (see SI for more details). The approach was first implemented for semiconductor quantum dots[49,50] where an empirical screening derived for bulk semiconductors was used. Our approach follows this original work with modifications for 2D materials as given by Torche et al.[51], which includes a random phase approximation (RPA) screening. The approach naturally yields any level of charge excitation, and takes the second quantization form

$$\mathcal{H} = \mathcal{H}_0 + \mathcal{H}_{eh} + \mathcal{H}_{ee} + \mathcal{H}_{hh}, \tag{1}$$

where

$$\begin{aligned}
\mathcal{H}_0 &= \sum_i \epsilon^{\mathrm{qp}}_i a^\dagger_i a_i - \sum_\alpha \epsilon^{\mathrm{qp}}_\alpha b^\dagger_\alpha b_\alpha,\\
\mathcal{H}_{eh} &= \sum_{i,j,\alpha,\beta} \left[\langle i\alpha|v|\beta j\rangle - \langle i\alpha|W|j\beta\rangle\right] a^\dagger_i b^\dagger_\beta b_\alpha a_j,\\
\mathcal{H}_{ee} &= \tfrac{1}{2}\sum_{i,j,k,l} \langle ij|W|kl\rangle a^\dagger_i a^\dagger_j a_l a_k,\\
\mathcal{H}_{hh} &= \tfrac{1}{2}\sum_{\alpha,\beta,\gamma,\lambda} \langle \alpha\beta|W|\gamma\lambda\rangle b^\dagger_\lambda b^\dagger_\gamma b_\alpha b_\beta.
\end{aligned}$$

Here, a_i and $a^\dagger_i$ (b_α and $b^\dagger_\alpha$) represent electron (hole) annihilation and creation operators, respectively. The Latin (Greek) index i,j ($\alpha,\beta,\ldots$) denote states above (below) the Fermi level. Moreover, $\epsilon^{\mathrm{qp}}_{i,\alpha}$ are quasiparticle energy levels typically found from a *GW* calculation. The two-body matrix elements are computed as

$$\langle ij|v|kl\rangle = \int \psi^*_i(1)\psi^*_j(2)v(\mathbf{r}_1,\mathbf{r}_2)\psi_k(1)\psi_l(2)\,\mathrm{d}1\mathrm{d}2,$$

$$\langle ij|W|kl\rangle = \int \psi^*_i(1)\psi^*_j(2)W(\mathbf{r}_1,\mathbf{r}_2)\psi_k(1)\psi_l(2)\,\mathrm{d}1\mathrm{d}2,$$

where $1 = (\mathbf{r}_1, \sigma)$ combines position and spin, while $\int \mathrm{d}1 = \sum_{\sigma=\uparrow,\downarrow}\int \mathrm{d}\mathbf{r}_1$ includes spin summation. Furthermore, ψ_i denotes single-particle wavefunctions found using density functional theory (DFT), while $v(\mathbf{r}_1, \mathbf{r}_2)$ represents the bare (unscreened) Coulomb interaction, and $W(\mathbf{r}_1, \mathbf{r}_2)$ the screened one, here computed within the RPA[52,53]. In this work the eh exchange interaction is left unscreened, which is still debatable[50,54]. In the SI, we compare results with and without screening of this term, similarly to Torche et al.[51]. Although discrepancies are minor, the unscreened results align closer with experiment.

Matrix elements for X, X^- and X^+, can be found in refs. 51,55, and with more detail in the SI. However, our implementation uses second quantization and does not require an explicit expression of these elements.

The starting point for our many-body calculations are Kohn–Sham wave functions and energies computed within DFT using the generalized-gradient approximation and the parametrization of Perdew, Burke and Ernzerhof (PBE)[56]. We utilize fully-relativistic, norm-conserving pseudopotentials[57] and employ the plane wave implementation as present in the `Quantum Espresso` suite[58,59] to compute the electronic ground state observables. An out-of-plane cell length of 50 Bohr has been used to suppress the spurious interaction of periodic images. During structural relaxation, we include an ab initio DFT-D3-BJ parameterization[60] of the van-der-Waals interaction, achieving a lattice constant closer to experimental values[61–64]. We found that a plane wave cutoff of 60 Ry yields converged results. The construction of the screened interaction kernel, *W*, includes the static inverse dielectric screening function, $\epsilon^{-1}_{\mathbf{GG}'}(\omega = 0, \mathbf{q})$, which we compute within the RPA using the `YAMBO` code[52,53]. An energetic screening cutoff of 10 Ry, along with 20 times more unoccupied bands than occupied bands, ensuring convergence of the response function. Lastly, we use Kohn–Sham energies as IP energy levels instead of quasi-particles energies in our Hamiltonian, since our interests lie in binding energies, which depend only on two-body matrix elements. Further computational details regarding implementation and convergence can be found in the SI.

Data availability

The data used and analyzed during the current study is available from the corresponding author upon reasonable request.

Code availability

The underlying code for this study is not publicly available but may be made available to qualified researchers on reasonable request from the corresponding author.

Received: 25 September 2024; Accepted: 22 January 2025;
Published online: 08 February 2025

References

1. Ramasubramaniam, A., Naveh, D. & Towe, E. Tunable band gaps in bilayer transition-metal dichalcogenides. *Phys. Rev. B* **84**, 205325 (2011).
2. Chaves, A. et al. Bandgap engineering of two-dimensional semiconductor materials. *npj 2D Mater. Appl.* **4**, 29 (2020).
3. Zhu, Z. Y., Cheng, Y. C. & Schwingenschlögl, U. Giant spin-orbit-induced spin splitting in two-dimensional transition-metal dichalcogenide semiconductors. *Phys. Rev. B* **84**, 153402 (2011).

4. Al-Ani, I. A. M. et al. Recent advances on strong light-matter coupling in atomically thin TMDC semiconductor materials. *J. Opt.* **24**, 053001 (2022).
5. Mak, K. F., Lee, C., Hone, J., Shan, J. & Heinz, T. F. Atomically thin MoS_2: a new direct-gap semiconductor. *Phys. Rev. Lett.* **105**, 136805 (2010).
6. Li, L. J. et al. Controlling many-body states by the electric-field effect in a two-dimensional material. *Nature* **529**, 185–189 (2015).
7. Rajapakse, M. et al. Intercalation as a versatile tool for fabrication, property tuning, and phase transitions in 2D materials. *npj 2D Mater. Appl.* **5**, 30 (2021).
8. Liu, Y. et al. Van der Waals heterostructures and devices. *Nat. Rev. Mater.* **1**, 16042 (2016).
9. Nielsen, C. E. M., da Cruz, M., Torche, A. & Bester, G. Accurate force-field methodology capturing atomic reconstructions in transition metal dichalcogenide moiré system. *Phys. Rev. B* **108**, 045402 (2023).
10. Ramezani, H. R. et al. Nonconventional screening of Coulomb interaction in two-dimensional semiconductors and metals: a comprehensive constrained random phase approximation study of *MX2* (*M* = Mo, W, Nb, Ta; *X* = S, Se, Te). *Phys. Rev. B* **109**, 125108 (2024).
11. Chernikov, A. et al. Exciton binding energy and nonhydrogenic Rydberg series in monolayer WS_2. *Phys. Rev. Lett.* **113**, 076802 (2014).
12. Qiu, D. Y., da Jornada, F. H. & Louie, S. G. Optical spectrum of MoS_2: many-body effects and diversity of exciton states. *Phys. Rev. Lett.* **111**, 216805 (2013).
13. Molina-Sánchez, A., Sangalli, D., Hummer, K., Marini, A. & Wirtz, L. Effect of spin-orbit interaction on the optical spectra of single-layer, double-layer, and bulk MoS_2. *Phys. Rev. B* **88**, 045412 (2013).
14. Mak, K. F. & Shan, J. Photonics and optoelectronics of 2D semiconductor transition metal dichalcogenides. *Nat. Photon* **10**, 216–226 (2016).
15. Zeng, Q. & Liu, Z. Novel optoelectronic devices: transition-metal-dichalcogenide-based 2D heterostructures. *Adv. Electron. Mater.* **4**, 1700335 (2018).
16. Splendiani, A. et al. Emerging photoluminescence in monolayer MoS_2. *Nano Lett.* **10**, 1271–1275 (2010).
17. Lezama, I. G. et al. Indirect-to-direct band gap crossover in few-layer $MoTe_2$. *Nano Lett.* **15**, 2336–2342 (2015).
18. Sun, Y., Wang, D. & Shuai, Z. Indirect-to-direct band gap crossover in few-layer transition metal dichalcogenides: a theoretical prediction. *J. Phys. Chem. C* **120**, 21866–21870 (2016).
19. Drüppel, M., Deilmann, T., Krüger, P. & Rohlfing, M. Diversity of trion states and substrate effects in the optical properties of an MoS_2 monolayer. *Nat. Commun.* **8**, 2117 (2017).
20. Deilmann, T. & Thygesen, K. S. Dark excitations in monolayer transition metal dichalcogenides. *Phys. Rev. B* **96**, 201113 (2017).
21. Courtade, E. et al. Charged excitons in monolayer WSe_2: experiment and theory. *Phys. Rev. B* **96**, 085302 (2017).
22. Jones, A. M. et al. Excitonic luminescence upconversion in a two-dimensional semiconductor. *Nat. Phys.* **12**, 323–327 (2016).
23. Ma, Y., Wang, Q., Han, S., Qu, F. & Fu, J. Fine structure mediated magnetic response of trion valley polarization in monolayer WSe_2. *Phys. Rev. B* **104**, 195424 (2021).
24. Li, Z. et al. Revealing the biexciton and trion-exciton complexes in BN encapsulated WSe_2. *Nat. Commun.* **9**, 3719 (2018).
25. Liu, E. et al. Gate tunable dark trions in monolayer WSe_2. *Phys. Rev. Lett.* **123**, 027401 (2019).
26. Lyons, T. P. et al. The valley Zeeman effect in inter- and intra-valley trions in monolayer WSe_2. *Nat. Commun.* **10**, 2330 (2019).
27. Ren, L. et al. Measurement of the conduction band spin-orbit splitting in WSe_2 and WS_2 monolayers. *Phys. Rev. B* **107**, 245407 (2023).
28. Ramasubramaniam, A. Large excitonic effects in monolayers of molybdenum and tungsten dichalcogenides. *Phys. Rev. B* **86**, 115409 (2012).
29. Zhang, C. et al. Probing critical point energies of transition metal dichalcogenides: surprising indirect gap of single layer WSe_2. *Nano Lett.* **15**, 6494–6500 (2015).
30. Liu, H. et al. Observation of intervalley quantum interference in epitaxial monolayer tungsten diselenide. *Nat. Commun.* **6**, 8180 (2015).
31. Hsu, W.-T. et al. Evidence of indirect gap in monolayer WSe_2. *Nat. Commun.* **8**, 929 (2017).
32. Ciccarino, C. J., Christensen, T., Sundararaman, R. & Narang, P. Dynamics and spin-valley locking effects in monolayer transition metal dichalcogenides. *Nano Lett.* **18**, 5709–5715 (2018).
33. Khalid, S., Medasani, B., Lyons, J. L., Wickramaratne, D. & Janotti, A. The deep-acceptor nature of the chalcogen vacancies in 2D transition-metal dichalcogenides. *2D Mater.* **11**, 021001 (2024).
34. Chen, Z., Luo, W., Liang, L., Ling, X. & Swan, A. K. Charge separation in monolayer WSe_2 by strain engineering: implications for strain-induced diode action. *ACS Appl. Nano Mater.* **5**, 15095–15101 (2022).
35. He, M. et al. Valley phonons and exciton complexes in a monolayer semiconductor. *Nat. Commun.* **11**, 618 (2020).
36. Wang, G. et al. In-plane propagation of light in transition metal dichalcogenide monolayers: optical selection rules. *Phys. Rev. Lett.* **119**, 047401 (2017).
37. Arora, A. et al. Excitonic resonances in thin films of WSe2: from monolayer to bulk material. *Nanoscale* **7**, 10421–10429 (2015).
38. Robert, C. et al. Fine structure and lifetime of dark excitons in transition metal dichalcogenide monolayers. *Phys. Rev. B* **96**, 155423 (2017).
39. Chow, C. M. E. et al. Monolayer semiconductor auger detector. *Nano Lett.* **20**, 5538–5543 (2020).
40. Li, Z. et al. Direct observation of gate-tunable dark trions in monolayer WSe_2. *Nano Lett.* **19**, 6886–6893 (2019).
41. Perea-Causin, R., Brem, S., Schmidt, O. & Malic, E. Trion photoluminescence and trion stability in atomically thin semiconductors. *Phys. Rev. Lett.* **132**, 036903 (2024).
42. Riley, J. M. et al. Direct observation of spin-polarized bulk bands in an inversion-symmetric semiconductor. *Nat. Phys.* **10**, 835–839 (2014).
43. Kapuściński, P. et al. Rydberg series of dark excitons and the conduction band spin-orbit splitting in monolayer WSe_2. *Commun. Phys.* **4**, 186 (2021).
44. He, K. et al. Tightly bound excitons in monolayer WSe_2. *Phys. Rev. Lett.* **113**, 026803 (2014).
45. Jindal, V. et al. Brightened emission of dark trions in transition-metal dichalcogenide monolayers. Preprint at https://arxiv.org/abs/2406.02095 (2024).
46. Kumar, A. M. et al. Strain fingerprinting of exciton valley character in 2D semiconductors. *Nat. Commun.* **15**, 7546 (2024).
47. Altick, P. L. & Glassgold, A. E. Correlation effects in atomic structure using the random-phase approximation. *Phys. Rev.* **133**, A632–A646 (1964).
48. Haken, H. *Quantum Field Theory Of Solids. An Introduction* (North-Holland Publishing Company, 1976).
49. Franceschetti, A., Fu, H., Wang, L. W. & Zunger, A. Many-body pseudopotential theory of excitons in InP and CdSe quantum dots. *Phys. Rev. B* **60**, 1819–1829 (1999).
50. Bester, G. Electronic excitations in nanostructures: an empirical pseudopotential based approach. *J. Phys. Condens. Matter* **21**, 023202 (2008).
51. Torche, A. & Bester, G. First-principles many-body theory for charged and neutral excitations: Trion fine structure splitting in transition metal dichalcogenides. *Phys. Rev. B* **100**, 201403 (2019).

52. Marini, A., Hogan, C., Grüning, M. & Varsano, D. yambo: An ab initio tool for excited state calculations. *Comput. Phys. Comm.* **180**, 1392–1403 (2009).
53. Sangalli, D. et al. Many-body perturbation theory calculations using the yambo code. *J. Phys. Condens. Matter* **31**, 325902 (2019).
54. Benedict, L. X. Screening in the exchange term of the electron-hole interaction of the bethe-salpeter equation. *Phys. Rev. B* **66**, 193105 (2002).
55. Deilmann, T., Drüppel, M. & Rohlfing, M. Three-particle correlation from a many-body perspective: trions in a carbon nanotube. *Phys. Rev. Lett.* **116**, 196804 (2016).
56. Perdew, J. P., Burke, K. & Ernzerhof, M. Generalized gradient approximation made simple. *Phys. Rev. Lett.* **77**, 3865–3868 (1996).
57. van Setten, M. et al. The PseudoDojo: training and grading a 85 element optimized norm-conserving pseudopotential table. *Comput. Phys. Comm.* **226**, 39–54 (2018).
58. Giannozzi, P. et al. QUANTUM ESPRESSO: a modular and open-source software project for quantum simulations of materials. *J. Phys. Condens. Matter* **21**, 395502 (2009).
59. Giannozzi, P. et al. Advanced capabilities for materials modelling with QUANTUM ESPRESSO. *J. Phys. Condens. Matter* **29**, 465901 (2017).
60. Grimme, S., Antony, J., Ehrlich, S. & Krieg, H. A consistent and accurate ab initio parametrization of density functional dispersion correction (DFT-D) for the 94 elements H-Pu. *J. Chem. Phys.* **132**, 154104 (2010).
61. Chen, J. et al. Chemical vapor deposition of large-size monolayer $MoSe_2$ crystals on molten glass. *J. Am. Chem. Soc.* **139**, 1073–1076 (2017).
62. Huang, J. et al. Large-area synthesis of monolayer WSe_2 on a SiO_2/Si substrate and its device applications. *Nanoscale* **7**, 4193–4198 (2015).
63. Yun, W. S., Han, S. W., Hong, S. C., Kim, I. G. & Lee, J. D. Thickness and strain effects on electronic structures of transition metal dichalcogenides: 2H-*MX2* semiconductors (M = Mo, W; X = S, Se, Te). *Phys. Rev. B* **85**, 033305 (2012).
64. Gusakova, J. et al. Electronic properties of bulk and monolayer TMDs: theoretical study within DFT framework (GVJ-2e Method). *Phys. Status Solidi A* **214**, 1700218 (2017).

Acknowledgements

The project is supported by the Deutsche Forschungsgemeinschaft (DFG, German Research Foundation) within the Priority Program SPP2244 2DMP and by the Cluster of Excellence "Advanced Imaging of Matter" of the DFG – EXC 2056 – project ID 390715994. Calculations were carried out on Hummel funded by the DFG – 498394658.We would like to extend thanks to Yasser Saleem and Marta Prada for fruitful discussions.

Author contributions

C.E.M.N. and F.F. carried out all calculations, analysed and visualized the results. Method development and writing were contributed equally by all authors (C.E.M.N., F.F., and G.B.)

Funding

Open Access funding enabled and organized by Projekt DEAL.

Competing interests

The authors declare no competing interests.

Additional information

Supplementary information The online version contains supplementary material available at https://doi.org/10.1038/s41699-025-00532-w.

Correspondence and requests for materials should be addressed to Gabriel Bester.

4.2 [E2] Bright Interlayer Excitons in Janus-structured TMD Bilayers

One of the characteristics that makes 2D systems especially appealing, is the possibility of stacking them vertically. This is used to fabricate new materials with properties differing from their pristine constituent counterparts [90]. In Fig. 4.2(a), the band structure of hexagonally stacked bilayer MoS_2-WS_2 is illustrated, where the colors of the bands indicate the contributions of the constituents, MoS_2 (green) and WS_2 (dark grey). The particular stacking configuration used here is the

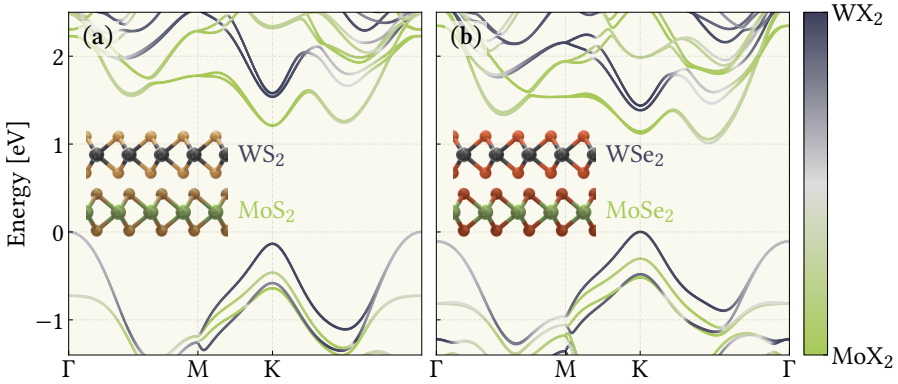

Figure 4.2: (a) The band structure of H_X^M-stacked bilayer MoS_2-WS_2 at the PBE level. The layer projection is encoded in the color of the bands, where green implies contribution from the MoS_2 layer, and dark grey from the WS_2 layer. (b) Same as (a), but for $MoSe_2$-WSe_2.

H_X^M ordering, which is the most stable between all stacking configurations. For most TMD heterostructures, a type-II transition occurs at the **K**-point [91–93], meaning that the CBM and the valence band maximum (VBM) stem from different materials, which is also the case for bilayer MoS_2-WS_2. However, in this system the VBM is no longer situated at **K**, but instead at **Γ**, which can be attributed to out-of-plane orbitals being the dominant contributors here [94]. Specifically, the hybridized bands split into two branches - a bonding and an anti-bonding state, of which the latter is found at an energy higher than that at the **K**-point. Similarly, in the lower conduction bands the energetic separation between **K** and **Q** decrease in the bilayer system. In fact, the **Q**-point is the CBM for most other TMD bilayer heterostructures as well [95–97], which can also be seen in Fig. 4.2(b) for $MoSe_2$-WSe_2.

The broken in-plane symmetry is a requirement for hosting interlayer excited states, such as excitons, where the hole and electron reside in different layers. The asymmetry between the layers can be further enhanced through the use of Janus structured monolayers [98–101]. While the two-faced Roman god, Janus, had one face that looked into the *past*, and one that gazed into the *future*, Janus materials are re*present*ed by featuring different chalcogenides on either face of the monolayer. This instigates potential drops in the monolayer, and further in the interface between layers, which reorders the bands - a mechanism described comprehensively in Ref. [102], mainly mediated by hybridization between the out-of-plane chalcogen orbitals.

In Fig. 4.3, the layer-projected bandstructure of bilayer MoSSe-WSSe is depicted for different interfacial configurations. First off, the bandstructure and band

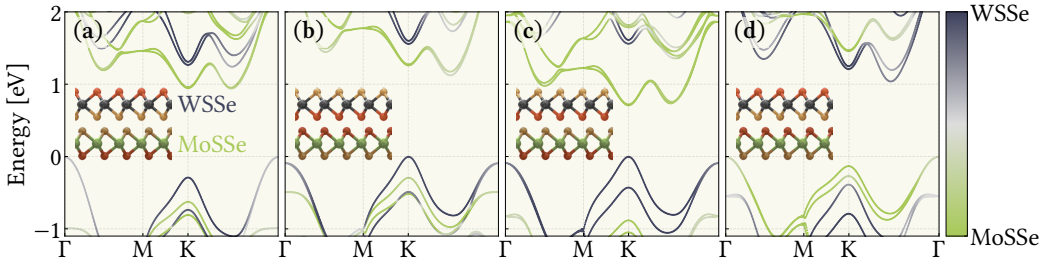

Figure 4.3: The bandstructure of bilayer Janus MoSSe-WSSe, where the inset shows the crystal structure. The interfaces displayed are S-S in (a), Se-Se in (b), S-Se in (c), and Se-S in (d). The layer projection is encoded in the color of the bands with green corresponding to MoSSe and dark grey to WSSe.

ordering of Fig. 4.3(a) bares a striking resemblance to WS_2 in Fig. 4.2(a) - an artifact of the S-S interlayer interface shared by the two systems. Similarly, when both interlayer interfaces are exchanged from S to Se as in Fig. 4.3(b), the bandstructure is reminiscent of WSe_2 in Fig. 4.2(b), again due to the interface. However, when the interface is heterogeneous as in Fig. 4.3(c,d), the aforementioned potential drops reorders the bands completely. For the S-Se interface seen in Fig. 4.3(c), the WSSe-like bands shift upwards in energy with respect to the MoSSe-like ones, and vice versa for the Se-S interface seen in Fig. 4.3(d). In fact, the lowest-energy optical transition in the Se-S interface, situated at **K**, has its carriers swapped relative to the remaining configurations, which has distinct implications for the excited states of this material. Specifically, because the lower-most conduction bands originate from the WSSe layer, the conduction band splitting in the Se-S configuration is significantly larger than in all other cases, where the light Mo-compound provides a comparably minute splitting, as was also demonstrated in Fig. 1.1(d,e,f). This unique property combined with vanishing (interlayer) electron-hole exchange coupling offers valuable opportunities for engineering the excited states of these materials, particularly in the design of spin-allowed exciton and trion groundstates, as revealed in the following work.

The following is reprinted (whole article) with permission from **C. E. Mørch Nielsen, F. Fischer, M. Prada, and G. Bester**, From dark to bright: first-principles prediction of ground state excitons and trions in Janus transition metal dichalcogenide bilayers, *2D Mater* **12**, 045015 (2025). [DOI: 10.1088/2053-1583/ae04fb]

Related Supplementary Information can be found in Section B.2.

IOP Publishing 2D Mater. 12 (2025) 045015 https://doi.org/10.1088/2053-1583/ae04fb

2D Materials

OPEN ACCESS

RECEIVED
18 June 2025

REVISED
11 August 2025

ACCEPTED FOR PUBLICATION
8 September 2025

PUBLISHED
30 September 2025

PAPER

From dark to bright: first-principles prediction of ground state excitons and trions in Janus transition metal dichalcogenide bilayers

Carl Emil Mørch Nielsen[1], **Franz Fischer**[1,2], **Marta Prada**[1,3] and **Gabriel Bester**[1,4,*]

[1] Institute of Physical Chemistry, University of Hamburg, Luruper Chaussee 149, 22607 Hamburg, Germany
[2] Max Planck Institute for the Structure and Dynamics of Matter, Luruper Chaussee 149, 22761 Hamburg, Germany
[3] I. Institute for Theoretical Physics, University of Hamburg, 22761 Hamburg, Germany
[4] The Hamburg Centre for Ultrafast Imaging, Luruper Chaussee 149, 22761 Hamburg, Germany
[*] Author to whom any correspondence should be addressed.

E-mail: gabriel.bester@uni-hamburg.de

Keywords: excitons, optoelectronics, trions, transition metal dichalcogenide, Janus, bright ground state

Supplementary material for this article is available online

Abstract

We investigate bilayer Janus transition metal dichalcogenides using *ab initio* many-body screened configuration interaction calculations and find that MoSSe–WSSe and WSSe–WSSe, with Se–S interfaces, exhibit spin-allowed interlayer exciton and trion ground states, in contrast to the spin-forbidden ground states of conventional transition metal dichalcogenides bilayers. This behavior arises from intrinsic structural asymmetry and interface-induced polarization, which rearrange the band structure. We further show that, besides the intrinsic asymmetry, also the applied external strain enables tuning of the ground state exciton brightness, allowing for detailed control of their optical properties.

1. Introduction

The two-dimensional (2D) family of transition metal dichalcogenides (TMDs) is an interesting and widely-known platform for studying optoelectronics and excited states [1–3]. They feature significant bandgaps, large spin–orbit coupling effects, and intriguing characteristics when stacked vertically via van der Waals interaction [4–6]. In particular, bilayer heterostructures usually lead to type-II band alignments, where band edge electrons and holes localize in different monolayers [7, 8]. This leads to long-lived interlayer excitons with lifetimes in the nanosecond range [9–11]. A popular material combination hosting these type of excitons is MoX_2–WX_2 ($X = S, Se, Te$), where the electron is localized in MoX_2 and the hole in WX_2. This can be seen already at the single-particle level in figure 1(b), where we color coded the band structure according to the localization of the state; with dark grey for WSe_2 and green for $MoSe_2$. These systems are particularly notable for their lack of mirror and inversion symmetry and a negligible lattice mismatch between the layers, typically around 0.1%, which prevents the formation of complex moiré patterns [12]. However, regardless of the stacking configuration, the exciton ground state remains spin-forbidden and therefore dark [11, 13, 14]—mainly an artifact of the marginal conduction band splitting in MoX_2. To circumvent this issue, we propose bilayer Janus TMDs, which, as opposed to their conventional TMD counterparts, feature different chalcogen elements on either face, as shown in figure 1(f) [15, 16]. This heterogeneity instigates potential drops in the individual monolayers and, for some stacking configurations, at the interface between them—substantially altering the electronic properties of the materials [17–21]. The introduction of the different interfaces, combined with various material combinations and stacking orders, means that a wide range of designs are feasible. In total, we examined 181 unique combinations, and identified at least two promising Janus heterostructures, namely bilayer MoSSe–WSSe and WSSe–WSSe with a Se–S interface, which exhibit a spin-allowed lowest energy transition along with a significant conduction band splitting. Figures 1(d) and (e) reveal the band

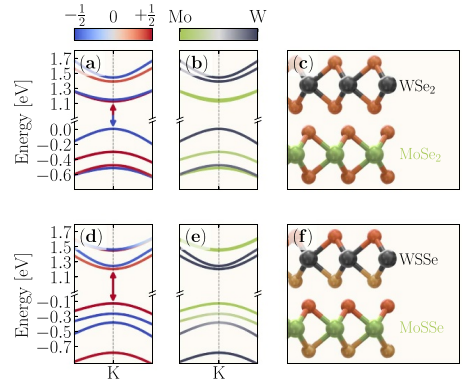

Figure 1. (a), (d) Spin-projected bands near **K** of hexagonally stacked bilayer MoS_2–WS_2 and MoSSe–WSSe, respectively. (b), (e) Layer-projected bands of bilayer MoS_2–WS_2 and MoSSe–WSSe, respectively. Green indicates large contribution from the lower Mo-base layer, while dark grey corresponds to the upper W-base layer. (c), (f) Visual representation of bilayer MoS_2–WS_2 and MoSSe–WSSe, respectively.

ordering near **K** for MoSSe–WSSe. Due to the potential drops instigated by the interface, the bands of the monolayers shift relative to each other (the dark grey WSSe bands shift down and the green MoSSe bands shift up in energy), such that the upper most valence bands have MoSSe character, while the lower most conduction bands are of WSSe character—opposite to the case of $MoSe_2$–WSe_2 shown in figure 1(b). This reordering of the valence bands leads to a change of spin character of the uppermost valence band, from spin down in $MoSe_2$–WSe_2 (blue in figure 1(a)) to spin up in MoSSe–WSSe (red in figure 1(d)). The new ordering of the conduction bands does not change the spin character of the lowest conduction band state at K (spin-up, red, in both figures 1(a) and (b)) but increases the conduction band splitting. This leads to a spin-allowed and potentially bright transition in MoSSe–WSSe with a rather large conduction band splitting.

In this work, we show that bilayer Janus TMD heterostructures, specifically MoSSe–WSSe and WSSe–WSSe with Se–S interfaces, exhibit spin-allowed ground state interlayer excitons and trions, in marked contrast to the spin-forbidden and optically dark ground states of conventional TMD bilayers. We attribute this behavior to the combined effects of intrinsic structural asymmetry and interface-induced polarization, which reorder the single-particle bands and enable optically active ground state transitions with substantial dark–bright energy splitting. Furthermore, we show that both intrinsic asymmetry and the application of external strain provide effective means to tune the brightness of the ground state excitons and trions, enabling detailed control over their optical properties and excitonic fine structure.

2. Results

We have conducted extensive calculations for both Se–S-interfaced bilayer MoSSe–WSSe and WSSe–WSSe, both exhibiting unique yet similar properties. For the sake of brevity, the results discussed in this section focus exclusively on the bilayer MoSSe–WSSe system, while findings for bilayer WSSe–WSSe are provided in the supplemental material (SM).

Figures 2(a) and (b) shows the band structure of Se–S interfaced MoSSe–WSSe projected onto the constituting layers in (a) and with the spin-projection in (b), in a similar fashion to figures 1(d) and (e) but for the entire Brillouin zone. Notably, the material features type-II band alignment, where the lower most conduction bands at **K** stem from the upper WSSe layer, while the upper most valence bands at **K** arise from the lower MoSSe layer [18, 22]. We find a lattice constant, a_0, of 3.22 Å [17, 23] and an interlayer distance, d, (metal–metal z-distance) of 6.29 Å. The spin–orbit coupling induced splittings at **K** of the conduction and valence bands are 40 and 136 meV, respectively, and the energetically lowest direct transition is spin-allowed and lies exactly at **K**. Moreover, the second and third highest valence bands are strongly hybridized between the two layers, as can be seen by the intermediate color of the bands in figure 2(a). We note, that the conduction band minimum lies around halfway between **K** and Γ, sometimes denoted **Q** [24–26], whereas the valence band maximum is situated at Γ. However, our focus lies on the low temperature limit, i.e. excitons with vanishing center-of-mass momentum, $\mathbf{Q}_{\mathrm{COM}} = 0$, meaning only momentum allowed transitions around **K** are relevant.

The exciton absorption spectrum of bilayer MoSSe–WSSe is displayed in figure 3(a) relative to the single-particle direct bandgap at **K**. The energetically lowest state, denoted A_{IL}, is a pure interlayer state, where the electron resides in WSSe and the hole in MoSSe, and has an exciton binding energy of 0.31 eV (with respect to the single-particle bandgap at **K**). It should be noted that figure 3(a) shows results for a k-point sampling of the Brillouin zone using a Monkhorst-Pack grid of 45×45, which is not fully converged. However, extrapolating the results to the converged grid is straight forward in this case (see SM) and the binding energies reported throughout the text are the converged values.

As seen in figure 3(b), the constituents of A_{IL} are spin-aligned (electrons and holes both in red color), and the optical transition relatively bright. Interestingly, D_{IL} with a binding energy of 0.27 eV appears comparably brighter in the spectrum, even though the constituents seem spin-forbidden, as

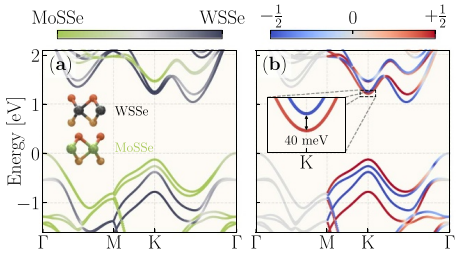

Figure 2. (a) Layer-projected band structure of Se–S interfaced MoSSe–WSSe at the PBE level, where green denotes the lower MoSSe layer and dark grey the upper WSSe layer, and (b) $\langle \hat{s}_z \rangle$-projected band structure where red denotes spin-up and blue spin-down. The inset shows the spin–orbit coupling induced conduction band splitting of 40 meV.

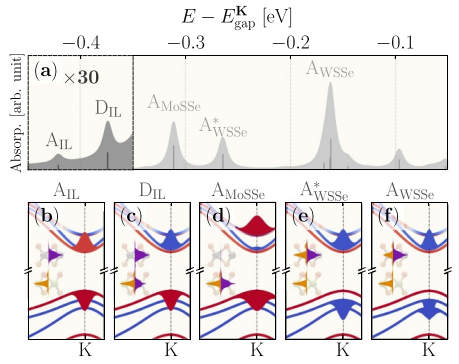

Figure 3. (a) Exciton absorption spectrum of bilayer MoSSe–WSSe relative to the interlayer single-particle bandgap at **K**. To increase the visibility of interlayer states, the first portion of the spectrum is magnified by a factor of 30. The prominent excitonic states labeled in (a) are analyzed in (b)–(f). The configurational weight is thereby encoded in the thickness of the bands; the color of the bands are according to the spin-character and the insets on the left of each panel shows the real-space excitonic density along z for the hole (orange) and the electron (purple).

portrayed in figure 3(c) (electron blue, hole red). This can be attributed to the electron localizing in both layers (purple electron density distributed over both layers, see inset of figure 3(c)), which allows for some overlap between electron and hole within the MoSSe layer. In essence, while A_{IL} is spin allowed but spatially indirect, D_{IL} is weakly spatially direct, and primarily spin-forbidden, although a weak spin-allowed admixing occurs. Furthermore, the bands are not fully spin-polarized, i.e. $\langle \hat{s}_z \rangle \neq \pm 1/2$, making the transition less spin-forbidden than anticipated by the different colors of the two bands in figure 3(c). Further details on the intralayer character of D_{IL} can be found in the SM. Due to the interlayer character of A_{IL} and the spin-asymmetry of D_{IL}, only minor electron–hole exchange coupling occurs for both states [27, 28]. This statement can be summarized as

$$\langle i\alpha|\nu|\alpha i\rangle = \begin{cases} \langle l_1 l_2|\nu|l_2 l_1\rangle \approx 0, & \text{for } A_{IL} \\ \langle \downarrow\uparrow|\nu|\uparrow\downarrow\rangle \approx 0, & \text{for } D_{IL} \end{cases}, \quad (1)$$

where i and α denote electron (conduction) and hole (valence) states, respectively. Similarly, l_{12} indicate the layer of each constituent fermion, while the arrows symbolize the spin character. For A_{IL}, the spatial separation leads to a minute orbital overlap between the hole and electron wavefunctions, and for D_{IL}, the orthogonality of the spin wavefunctions leads to vanishing coupling. As such, the splitting between the two states (48 meV) is comparable to the conduction band splitting (40 meV). Pang and Wang [29] report comparable interlayer exciton binding energies of 0.32 eV for rhombohedral-stacked Se–S interfaced MoSSe–WSSe; however, they observe that the lowest-lying exciton is spin-forbidden and dark. This can be understood when realizing that the rhombohedral-stacked structure can be obtained by rotating one of our layers by 180° in figure 1(f). Such a rotation leads to an interchange of **K** and **K**′, and hence an inversion of the spin character in the bands associated with the rotated layer.

Figures 3(d)–(f) shows the three spin-allowed bright states that are most prominent in the interlayer part of the spectrum. A_{MoSSe} is a pure interlayer state residing in the MoSSe layer, and, when compared to the MoSSe single-particle bandgap at **K** (found between the upper most valence band and the third conduction band), features an exciton binding energy of 0.45 eV. In contrast, A^*_{WSSe} and A_{WSSe} show intralayer WSSe character with exciton binding energies of 0.41 and 0.30 eV, respectively. Due to the mixed layer localization of the second and third highest valence bands we noted earlier in figure 2(a), the hole hybridizes between the two monolayers for both states (seen in the orange hole distribution). However, A_{WSSe} has a larger contribution from the third highest valence band compared to A^*_{WSSe}, which explains the smaller binding energy.

The presented excitonic states and associated binding energies compare well to their conventional TMD counterparts, namely MoS_2–WS_2 and $MoSe_2$–WSe_2. Here, the interlayer binding energies are typically in the range of 0.3–0.4 eV, while intralayer states are bound by 0.3–0.6 eV [11, 13, 14, 30]. However, the splitting between the interlayer, D_{IL}, and intralayer states, A_{MoSSe}, (60 meV) is significantly smaller than for the regular TMD counterpart,e.g. MoS_2–WS_2 (200 meV) [11, 14, 30]. This can be attributed to the relatively small energetic offsets between the MoSSe and WSSe bands in the upper most valence bands compared to MoX_2–WX_2 (see figures 1(b) and (e))—an effect of the dipole moment induced by the Janus structured interface.

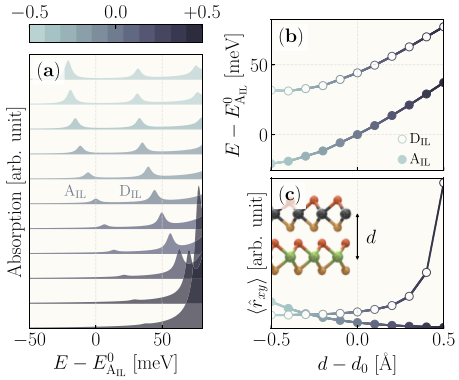

Figure 4. (a) Low-energy excitonic absorption spectra for different interlayer distances centered around the energy of A_{IL} at equilibrium. The color indicates the offset from equilibrium spacing, $d - d_0$, in Å. (b), (c) energetic offset and in-plane dipole moment of A_{IL} (filled) and D_{IL} (hollow) plotted against the variation of interlayer distance.

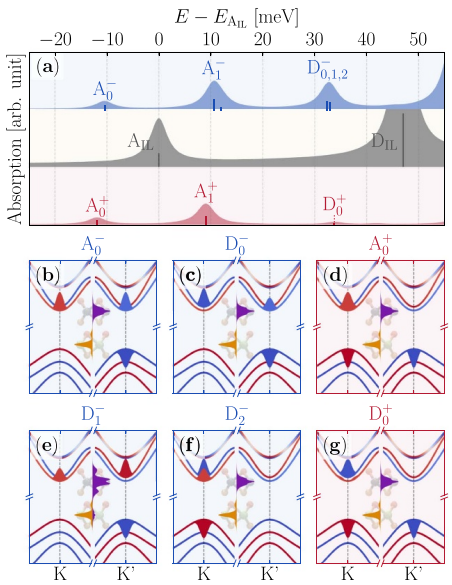

Figure 5. (a) Trion and exciton absorption spectra of bilayer MoSSe–WSSe with energy given relative to A_{IL}. Negatively charged trions in upper, blue panel, excitons in middle, gray panel and positively charged trions in lower, red panel. The configurational weight of the states of interest are displayed in (b)–(g) in the same fashion as in figures 3(b)–(f).

We have further investigated the effects of out-of-plane strains on the lowest-lying excitonic states, A_{IL} and D_{IL}, and depicted the results in figure 4(a). While previous work has explored the impact of in-plane strain and hydrostatic pressure [29, 31], our results specifically examine out-of-plane strain effects. Here, we vary the interlayer spacing (metal–metal distance), d, between the two layers around the equilibrium distance, d_0, and observe in figure 4(b) that both A_{IL} and D_{IL} experience a blueshift with increasing d. We attribute this to two effects: a bandgap modulation with strain and a reduction of the direct Coulomb interaction with increasing interlayer spacing. Regarding the first effect, we observe that the bandgap at **K** changes by −7 meV (+26 meV) when d is compressed (expanded) by −0.5 Å (+0.5 Å). The exciton calculations of A_{IL} show a much larger shift of −20 meV and +38 meV for compression and expansion, respectively. We attribute the missing energetic offsets to the direct Coulomb interaction being increased for decreasing interlayer distance. Both effects are of similar magnitude: 33 meV for the bandgap modulation and 25 meV for the change in Coulomb interaction between the two extrema.

In figure 4(c) we plot the strength of the in-plane optical dipole $\langle \hat{r}_{xy} \rangle$ for D_{IL} and A_{IL} as a function of interlayer spacing. We observe for A_{IL} an increase by a factor of four with decreasing interlayer distance, which can be explained by an increased overlap between the hole- and electron wavefunctions for this interlayer exciton. In contrast, D_{IL} becomes counterintuitively brighter when the layers are pulled apart. We observe that for $d - d_0 = +0.5$ Å, the electron of D_{IL} fully localizes in the lower MoSSe layer, and as such D_{IL} becomes of intralayer character, explaining the large increase in brightness.

Finally, we study the effect of adding additional carriers to the system, leading to the formation of charged excitons, i.e. trions. In this work, we focus only on trion species, where the total center-of-mass momentum of the constituent carriers, $\mathbf{Q}_{COM}$, equals **K** for negatively charged trions and **K′** for positively charged trions. This typically results in trion species where all carriers are located in the **K**- and/or **K′**-valleys. However, for electron doping, lower lying bright and dark states may be found for $\mathbf{Q}_{COM} = \mathbf{Q}$ [26, 32], due to the energetically low-lying nature of the **Q**-valley in bilayer TMD-like systems. A similar statement holds true for hole doping and the Γ-point. Nevertheless, we do not compute these states, since they are expected to show similar traits regarding bright–dark ordering as for $\mathbf{Q}_{COM} = \mathbf{K}$.

Figure 5(a) shows the absorption spectra of excitons (middle panel), negative trions (upper panel) and positive trions (lower panel). The initial state for photon absorption is represented by an electron loatced in the lowest conduction band at **K** for negatively charged trions, and a hole located in the top valence band at **K′** for positively charged trions. A_0^- is the energetically lowest negatively charged trion state with a binding energy of 11 meV with respect to A_{IL}, and resembles an electron at **K** combined with an A_{IL}-like electron–hole pair at **K′**, as seen in figure 5(b).

We observe three nearly degenerate states, denoted as $D^-_{0,1,2}$, positioned 32 meV below D_{IL} (be reminded that this value corresponds to the fully converged extrapolated value, while the results in figure 5 are for the 45×45 k-point grid). This value aligns closely with the trion binding energies of intralayer states identified in Janus TMD monolayers [33], as well as those reported in conventional TMD heterobilayers [14, 34]. We attribute the near-degeneracy of the three states to the spatial separation of wavefunctions, which, due to reduced electron–hole overlap, results in significantly reduced exchange-couplings. In the monolayer, these three states have significantly larger exchange-couplings and, hence, splitting [26]. Moreover, D^-_1 and D^-_2 are deceptively bright—in a similar manner to D_{IL}. For D^-_1, we attribute this to the electron localizing slightly in the lower MoSSe layer, such that a significant overlap forms between the wavefunctions of the two carrier types. In the case of D^-_2, the relative brightness of the state can be understood from the bright A_{IL}-like transition, which is spin-allowed but spatially indirect, between the upper valence band and lower conduction band. As opposed to D^-_1 and D^-_2, D^-_0 appears completely dark, since we have assumed a thermalization of the additional electron before absorption leaving the upper conduction band empty. At higher temperatures, however, the second conduction band is thermally accessible, in which case D^-_0 is expected to show some bright character. Lastly, the splitting between A^-_0 and $D^-_{0,1,2}$ is found to be 43 meV—almost identical to the conduction band splitting of 40 meV, and can be easily understood from the configurational weights, see figures 5(c), (e) and (f).

A^+_0, depicted in figure 5(d), is the positively charged analogue of A^-_0 with a binding energy of 11 meV, and also features similar brightness. Contrastingly, D^+_0, which has the electron in the second conduction band, appears dark, especially compared to the similar case of D_{IL} and D^-_1. However, as opposed to the aforementioned states, D^+_0 is a true interlayer state, and is as such almost completely dark.

3. Conclusions

Based on *ab initio* screened configuration interaction calculations, we have demonstrated the presence of spin-allowed exciton and trion ground states in MoSSe–WSSe and WSSe–WSSe bilayers of Janus TMDs. The intra- an interlayer polarization of the Janus bilayers allows, for the specific material combinations mentioned, to shift the bands in such a way that the exciton (and trion) ground state is spin-allowed, in contrast to bilayers of conventional TMDs, where a dark spin-forbidden ground state prevails.

The resulting strong coupling of the ground state to the light field paves the way for faster optoelectronic devices and facilitates the generation, manipulation, and detection of complex excitonic states—including trions—which are especially valuable for valleytronics, spintronics, and advanced quantum information protocols.

Furthermore, we show that both intrinsic structural asymmetry and extrinsic factors such as applied strain can be used as design parameters, enabling the rational creation of heterostructures with tailored spin and optical properties. In particular, our results demonstrate that while the intrinsic Janus asymmetry can lead to bright ground state excitons and trions, the application of external strain provides additional control over their brightness, inspiring new strategies for next-generation quantum light sources and highly responsive 2D optoelectronic platforms.

4. Methodology

We employ a parameter-free, truly *ab initio* effective many-body Hamiltonian, $\mathcal{H}$, formulated in the electron–hole (eh) picture, adapted from earlier work on semiconductor quantum dots [35, 36] and refined for 2D materials [26, 37]. The Hamiltonian takes the form:

$$\mathcal{H} = \mathcal{H}_0 + \mathcal{H}_{eh} + \mathcal{H}_{ee} + \mathcal{H}_{hh},$$

where $\mathcal{H}_0$ incorporates single-particle energies, while $\mathcal{H}_{eh}$, $\mathcal{H}_{ee}$ and $\mathcal{H}_{hh}$ capture electron–hole, electron–electron and hole–hole interactions, respectively, formulated in second quantization. Two-body matrix elements are computed from wavefunctions obtained via density functional theory (DFT) [38, 39], where all components except electron–hole exchange elements include a screened Coulomb potential. A detailed theoretical description can be found in previous works [26]. We obtain the screened interaction kernel, W, through the random phase approximation [40, 41], while wavefunctions and Kohn–Sham energy levels are computed within the generalized-gradient approximation with PBE parametrization [42]. During structural relaxation of our systems, we include an *ab initio* DFT-D3-BJ parameterization [43] to account for the vdW interaction between the layers. The results presented in this work do not feature self-energy corrected quasiparticle energies as typically found from a *GW* calculation. This is both due to the extensive nature of *GW*-convergence, and because our interests do not lie in obtaining energies that are accurate on an absolute energy scale, but rather on the energetic positions of excited states relative to the bandgap and one another [44]. Further computational details and convergence studies are available in the SM.

Data availability statement

The data cannot be made publicly available upon publication because no suitable repository exists for hosting data in this field of study. The data that support the findings of this study are available upon reasonable request from the authors.

Supplementary material available at https://doi.org/10.1088/2053-1583/ae04fb/data1.

Acknowledgments

The project is supported by the Deutsche Forschungsgemeinschaft (DFG, German Research Foundation) within the Priority Program SPP2244 2DMP and by the Cluster of Excellence 'Advanced Imaging of Matter' of the DFG—EXC 2056 – Project ID 390715994. Calculations were carried out on Hummel funded by the DFG – 498394658.

Code availability

The underlying code for this study is not publicly available but may be made available to qualified researchers on reasonable request from the corresponding author.

Conflict of interest

All authors declare no financial or non-financial competing interests.

ORCID iDs

Carl Emil Mørch Nielsen 0000-0002-2597-7120
Franz Fischer 0009-0007-2416-4199
Marta Prada 0000-0003-3845-9012
Gabriel Bester 0000-0003-2304-0817

References

[1] Castro Neto A H, Guinea F, Peres N M R, Novoselov K S and Geim A K 2009 The electronic properties of graphene *Rev. Mod. Phys.* **81** 109
[2] Mak K F, Lee C, Hone J, Shan J and Heinz T F 2010 Atomically thin MoS_2: a new direct-gap semiconductor *Phys. Rev. Lett.* **105** 136805
[3] Manzeli S, Ovchinnikov D, Pasquier D, Yazyev O V and Kis A 2017 2D transition metal dichalcogenides *Nat. Rev. Mater.* **2** 17033
[4] Zhu Z Y, Cheng Y C and Schwingenschlögl U 2011 Giant spin-orbit-induced spin splitting in two-dimensional transition-metal dichalcogenide semiconductors *Phys. Rev. B* **84** 153402
[5] Novoselov K S, Mishchenko A, Carvalho A and Neto A H C 2016 2D materials and van der Waals heterostructures *Science* **353** aac9439
[6] Chaves A *et al* 2020 Bandgap engineering of two-dimensional semiconductor materials *npj 2D Mater. Appl.* **4** 29
[7] Gong C, Zhang H, Wang W, Colombo L, Wallace R M and Cho K 2013 Band alignment of two-dimensional transition metal dichalcogenides: application in tunnel field effect transistors *Appl. Phys. Lett.* **103** 053513
[8] Zhang C *et al* 2016 Systematic study of electronic structure and band alignment of monolayer transition metal dichalcogenides in Van der Waals heterostructures *2D Mater.* **4** 015026
[9] Rivera P *et al* 2015 Observation of long-lived interlayer excitons in monolayer $MoSe_2$–WSe_2 heterostructures *Nat. Commun.* **6** 6242
[10] Miller B, Steinhoff A, Pano B, Klein J, Jahnke F, Holleitner A and Wurstbauer U 2017 Long-lived direct and indirect interlayer excitons in van der Waals heterostructures *Nano Lett.* **17** 5229
[11] Torun E, Miranda H P C, Molina-Sánchez A and Wirtz L 2018 Interlayer and intralayer excitons in MoS_2/WS_2 and $MoSe_2$/WSe_2 heterobilayers *Phys. Rev. B* **97** 245427
[12] Nielsen C E M, da Cruz M, Torche A and Bester G 2023 Accurate force-field methodology capturing atomic reconstructions in transition metal dichalcogenide moiré system *Phys. Rev. B* **108** 045402
[13] Gillen R and Maultzsch J 2018 Interlayer excitons in $MoSe_2$/WSe_2 heterostructures from first principles *Phys. Rev. B* **97** 165306
[14] Deilmann T and Thygesen K S 2018 Interlayer trions in the MoS_2/WS_2 van der Waals heterostructure *Nano Lett.* **18** 1460
[15] Zhang J *et al* 2017 Janus Monolayer Transition-Metal Dichalcogenides *ACS Nano* **11** 8192
[16] Trivedi D B *et al* 2020 Room-temperature synthesis of 2D Janus crystals and their heterostructures *Adv. Mater.* **32** 2006320
[17] Li F, Wei W, Zhao P, Huang B and Dai Y 2017 Electronic and optical properties of pristine and vertical and lateral heterostructures of Janus MoSSe and WSSe *J. Phys. Chem. Lett.* **8** 5959
[18] Wang Y, Wei W, Huang B and Dai Y 2019 The mirror asymmetry induced nontrivial properties of polar WSSe/MoSSe heterostructures *J. Phys.: Condens. Matter* **31** 125003
[19] Ju L, Bie M, Tang X, Shang J and Kou L 2020 Janus WSSe monolayer: an excellent photocatalyst for overall water splitting *ACS Appl. Mater. Interfaces* **12** 29335
[20] Zheng T, Lin Y-C, Rafizadeh N, Geohegan D B, Ni Z, Xiao K and Zhao H 2022 Janus monolayers for ultrafast and directional charge transfer in transition metal dichalcogenide heterostructures *ACS Nano* **16** 4197
[21] Li Y, Yan Z and Wang S 2024 Spin character of interlayer excitons in tungsten dichalcogenide heterostructures: GW-BSE calculations *Phys. Rev. B* **109** 045422
[22] Jiang Y, Lei S, Jiang Y and Wang M 2024 Highly stable two-dimensional Janus transition metal dichalcogenide-based van der Waals heterostructures for exceptional solar cell performance *Surf. Interfaces* **52** 104830
[23] Ma X, Wu X, Wang H and Wang Y 2018 A Janus MoSSe monolayer: a potential wide solar-spectrum water-splitting photocatalyst with a low carrier recombination rate *J. Mater. Chem. A* **6** 2295
[24] Piatti E, De Fazio D, Daghero D, Tamalampudi S R, Yoon D, Ferrari A C and Gonnelli R S 2018 Multi-valley superconductivity in ion-gated MoS_2 layers *Nano Lett.* **18** 4821
[25] Ding D *et al* 2022 Multivalley superconductivity in monolayer transition metal dichalcogenides *Nano Lett.* **22** 7919
[26] Mørch Nielsen C E, Fischer F and Bester G 2025 Beyond the K-valley: exploring unique trion states in indirect band gap monolayer WSe_2 *npj 2D Mater. Appl.* **9** 11
[27] Thygesen K S 2017 Calculating excitons, plasmons and quasiparticles in 2D materials and van der waals heterostructures *2D Mater.* **4** 022004
[28] Deilmann T and Thygesen K S 2018 Interlayer excitons with large optical amplitudes in layered van der waals materials *Nano Lett.* **18** 2984
[29] Pang R and Wang S 2022 Dipole moment and pressure dependent interlayer excitons in MoSSe/WSSe heterostructures *Nanoscale* **14** 3416

[30] Okada M *et al* 2018 Direct and indirect interlayer excitons in a van der Waals heterostructure of hBN/WS_2/MoS_2/hBN *ACS Nano* **12** 2498
[31] Guo W, Ge X, Sun S, Xie Y and Ye X 2020 The strain effect on the electronic properties of the MoSSe/WSSe van der Waals heterostructure: a first-principles study *Phys. Chem. Chem. Phys.* **22** 4946
[32] Perea-Causin R, Brem S, Schmidt O and Malic E 2024 Trion photoluminescence and trion stability in atomically thin semiconductors *Phys. Rev. Lett.* **132** 036903
[33] Pucko K O *et al* 2022 Excitons and trions in WSSe monolayers *2D Mater.* **10** 015018
[34] Calman E V, Fowler-Gerace L H, Choksy D J, Butov L V, Nikonov D E, Young I A, Hu S, Mishchenko A and Geim A K 2020 Indirect excitons and trions in $MoSe_2$/WSe_2 van der Waals heterostructures *Nano Lett.* **20** 1869
[35] Franceschetti A, Fu H, Wang L W and Zunger A 1999 Many-body pseudopotential theory of excitons in InP and CdSe quantum dots *Phys. Rev. B* **60** 1819–29
[36] Bester G 2008 Electronic excitations in nanostructures: an empirical pseudopotential based approach *J. Phys.: Condens. Matter* **21** 023202
[37] Torche A and Bester G 2019 First-principles many-body theory for charged and neutral excitations: trion fine structure splitting in transition metal dichalcogenides *Phys. Rev. B* **100** 201403
[38] Giannozzi P *et al* 2009 QUANTUM ESPRESSO: a modular and open-source software project for quantum simulations of materials *J. Phys.: Condens. Matter* **21** 395502
[39] Giannozzi P *et al* 2017 Advanced capabilities for materials modelling with QUANTUM ESPRESSO *J. Phys.: Condens. Matter* **29** 465901
[40] Marini A, Hogan C, Grüning M and Varsano D 2009 yambo: an *ab initio* tool for excited state calculations *Comput. Phys. Commun.* **180** 1392–403
[41] Sangalli D *et al* 2019 Many-body perturbation theory calculations using the yambo code *J. Phys.: Condens. Matter* **31** 325902
[42] Perdew J P, Burke K and Ernzerhof M 1996 Generalized gradient approximation made simple *Phys. Rev. Lett.* **77** 3865–8
[43] Grimme S, Antony J, Ehrlich S and Krieg H 2010 A consistent and accurate *ab initio* parametrization of density functional dispersion correction (DFT-D) for the 94 elements H-Pu *J. Chem. Phys.* **132** 154104
[44] Marsili M, Molina-Sánchez A, Palummo M, Sangalli D and Marini A 2021 Spinorial formulation of the *GW*-BSE equations and spin properties of excitons in two-dimensional transition metal dichalcogenides *Phys. Rev. B* **103** 155152

4.3 [E3] Relaxation Effects in Moiré-structured TMD Heterostructures

When two monolayers are stacked on top of each other with a relative twist, θ, between them, a moiré pattern often emerges. Similarly, if the constituent layers feature a mismatch between their respective lattice constants, δ, the pattern emerges as well. For theoretical purposes, especially *ab initio* implementations, this makes it especially difficult to simulate such systems due to their sizable unit cells, and, as such, the ability to generate the smallest possible moiré structure unit cells for any given θ or δ is of utmost importance.

For two arbitrary monolayers with a relative twist between them, the condition to form a moiré unit cell is that

$$i\mathbf{a}_{1,t} + j\mathbf{a}_{2,t} = \bar{\mathbf{R}}(\theta)\left[k\mathbf{a}_{1,b} + l\mathbf{a}_{2,b}\right], \tag{4.1}$$

where i, j, k and l are integers, $\bar{\mathbf{R}}(\theta)$ denotes the 2D rotation matrix, and the subscripts t and b denote the top and bottom layers, respectively. The idea of this criteria can be understood from Fig. 4.4(a,b), in which the vector that connects two points where the constituent lattices overlap, forms the primitive vector of the moiré unit cell. In this particular example, the two layers are *commensurate*,

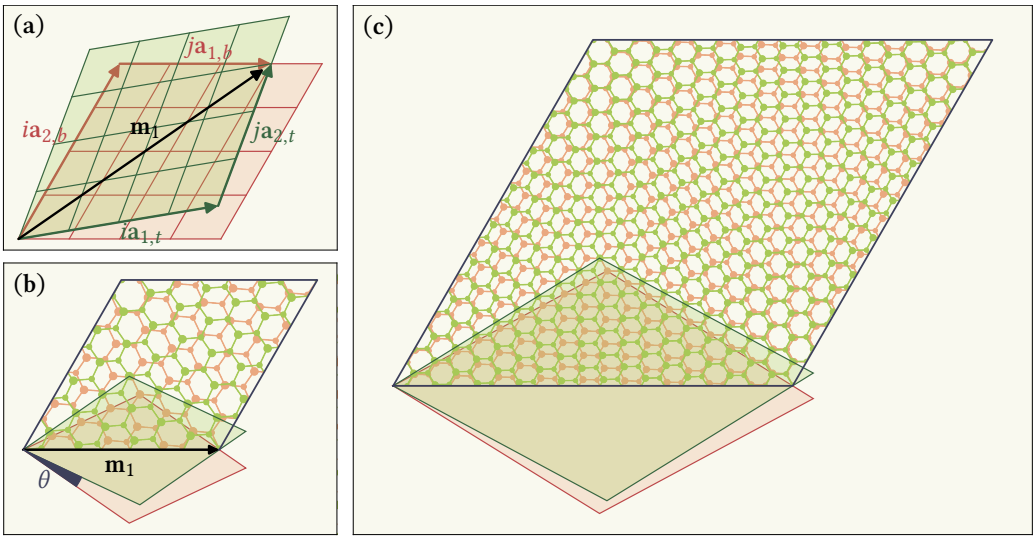

Figure 4.4: (a) Visualization of the criterion to create moiré structure unit cell, where $\mathbf{m}_1$, denotes a primitive vector of the moiré heterostructure. The grid lines seen on both the upper (green) and lower (orange) layers denote the unit cells of the constituent layers. (b) The moire structure generated by letting $i = j + 1 = 4$ as seen in (a) with the twist angle θ highlighted. (c) Similar to (b), but for $i = j + 1 = 10$.

meaning they have the same lattice constants, and by extension $k = j$, $l = i$. This is, generally, not the case for *incommensurate* heterostructures, where $\delta \neq 0$. Finally, Fig. 4.4(c) shows a larger moiré unit cell in the case where $i = j + 1 = 10$.

The criterion of Eq. (4.1) can be used to find and generate moire heterostructures by iterating over different values of i, j (and further k, l for incommensurate structures). Fig. 4.5(a) shows the number of atoms with respect to twist angle for all possible commensurate moirés structure with less than 10^4 atoms in the

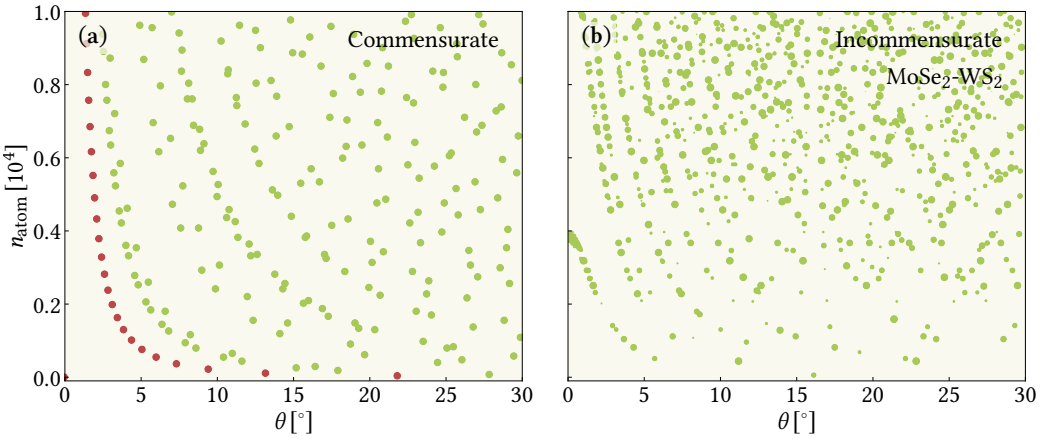

Figure 4.5: (a) The number of atoms, n_{atom}, with respect to the twist angle, θ, for all commensurate structures where $n_{\text{atom}} < 10^4$. Brown markers denote structures where $i = j + 1$. (b) Similar to (a), but for the incommensurate heterostructure of bilayer $MoSe_2$-WS_2, which features a lattice mismatch of $\approx 4\%$. The size of the marker indicates the level of in-plane strain put on the constituting layers to force them to align perfectly. Larger markers indicate less strain, and the maximum allowed level of strain is here set to 0.1%.

unit cell. Here, the brown markers indicate structures where $i = j + 1$, which, coincidentally, will create the smallest possible cell for the given angles. Indeed, in this work, the only commensurate structures used are the ones following this line. In Fig. 4.5(b), a similar plot is shown for incommensurate $MoSe_2$-WS_2 heterostructures, which feature a lattice mismatch of $\delta \approx 4\%$. For such structures, a more loose interpretation of Eq. (4.1) must be used, since perfect alignment is almost never guaranteed. Here, specifically, the constituting monolayers are allowed a $\pm 0.1\%$ deviation from their pristine lattice constants, which is represented in the size of the markers. Larger markers indicate smaller deviations, meaning smaller strain must be applied to align the layers. Interestingly, at $\theta = 0$, a moire heterostructure is found with 3903 atoms, where $i = 25$, $k = 26$ and $j = l = 0$, which agrees with the lattice mismatch of $\approx 4\%$.

While the unit cell depicted Fig. 4.4(c) features a distinct moiré pattern, it does not represent a structurally optimized example. In reality, the moiré structure resembles a landscape of variations in interlayer binding energies, which shifts around atomic positions both in- and out-of-plane [103–107]. This, in turn, leads to significant changes in the energetic landscape, and has consequences for the underlying physics, e.g. the localization of quasiparticles [108–110]. Therefore, to accurately describe a moiré structured unit cell, especially for small θ, and all the characteristics that go along with it, the inclusion of relaxation effects is crucial. To this extent, the following work presents a parametrized force-field model for capturing critical optimization effects based on *ab initio* calculations. As will be shown, this model allows for obtaining highly accurate results for moiré structures at almost any θ.

The following is reprinted (whole article) with permission from **C. E. Mørch Nielsen, F. Fischer, and G. Bester**, Accurate force-field methodology capturing atomic reconstructions in transition metal dichalcogenide moiré system, *Phys. Rev. B* **108**, 045402 (2023). [DOI: 10.1103/PhysRevB.108.045402]

Accurate force-field methodology capturing atomic reconstructions in transition metal dichalcogenide moiré system

Carl Emil Mørch Nielsen, Miguel da Cruz, Abderrezak Torche, and Gabriel Bester
Institute of Physical Chemistry, University of Hamburg, 22607 Hamburg, Germany

(Received 14 March 2023; accepted 2 June 2023; published 5 July 2023)

In this work, a generalized force-field methodology for the relaxation of large moiré heterostructures is proposed. The force-field parameters are optimized to accurately reproduce the structural degrees of freedom of some computationally manageable cells relaxed using density functional theory. The parameters can then be used to handle large moiré systems. We specialize in the case of 2H-phased twisted transition-metal dichalcogenide homo- and heterobilayers using a combination of the Stillinger-Weber intralayer and the Kolmogorov-Crespi interlayer potential. Force-field parameters are developed for all combinations of MX_2 for $M \in \{\mathrm{Mo}, \mathrm{W}\}$ and $X \in \{\mathrm{S}, \mathrm{Se}, \mathrm{Te}\}$. The results show agreement within 20 meV in terms of band structure between density functional theory and force-field relaxation. Using the relaxed structures, a simplified and systematic scheme for the extraction of the interlayer moiré potential is presented for both R- and H-stacked systems. We show that in-plane and out-of-plane relaxation effects on the moiré potential, which is made both deeper and wider after relaxation, are essential. An interpolation based methodology for the calculation of the interlayer binding energy is also proposed. Finally, we show that atomic reconstruction, which is captured by the force-field method, becomes especially prominent for angles below 4°–5°, when there is no mismatch in lattice constant between layers.

DOI: 10.1103/PhysRevB.108.045402

I. INTRODUCTION

Two dimensional (2D) moiré systems are currently an especially attractive playground for new technological applications [1–4]. Lattice mismatch combined with the twist angle between the constituent layers allows for an ingenious way of external mechanical control of the moiré period and thus the resulting electronic properties. Without a doubt, the pioneering discovery of twisted bilayer graphene and its magic angle of 1.05° [5] was the major driving force toward the study of 2D heterostructures and constituted the basis for the field of twistronics. An interesting and widely studied class of moiré systems is the 2D family of transition metal dichalcogenides (TMDs), featuring strong light-matter interaction and large spin-orbit coupling with a sizable band gap [6]. A fundamental advantage of TMDs is that flat minibands are not only realised at specific angles, but exist in a continuum of small angles [7]. An example of a moiré-structured TMD system can be seen in Fig. 1. Moreover, experimental and theoretical findings of the excited states in type-II aligned heterostructured TMDs show evidence of spatially indirect excitons localized within certain registries of the moiré structure [7–10]. Moiré structured TMDs provide a platform for studying correlated quantum phenomena [11] including hole Mott insulator states at integer and fractional fillings with generalized Wigner crystallization, essentially creating a Fermi-Hubbard system [12–16]. Moiré structured TMD bilayer systems also allows for realization of Bose-Hubbard physics with excitons trapped in a periodic triangular potential and subject to strong Coulomb interactions [17].

Moiré physics in TMDs are largely determined by the shape of the twist-induced moiré potential, which arises from local stacking configurations, lattice corrugation and, for small angles, atomic reconstruction [7,18–25]. As a consequence, relaxation effects are important for numerical simulations that involve moiré structured TMD systems prone to atomic reconstruction, and/or structures with a moiré period large enough to corrugate the individual layers [26,27]. From an *ab initio* standpoint, this presents a large challenge owing to the fact that relaxation is a computational bottleneck in such calculations. In an excellent paper by Naik *et al.* [28], a method to overcome this problem is suggested by using a force-field model based on a combination of the Stillinger-Weber (SW) [29,30] and Kolmogorov-Crespi (KC) [31,32] potentials. The SW force-field accurately describes the intralayer forces, while the KC potential captures van der Waals (vdW) interaction between layers and includes a stacking-dependent term. Previously, this had been parametrized and applied to graphene and hexagonal boron nitride [33–36] but is now also available for MX_2 homobilayers, where $M \in \{\mathrm{Mo}, \mathrm{W}\}$ and $X \in \{\mathrm{S}, \mathrm{Se}\}$ [28,37].

However, the parameters presented in Ref. [28] are somewhat inaccurate when comparing to density functional theory (DFT) calculated results, e.g., for some structures, the band gap is inaccurate by up to 100 meV. Even more importantly, the band curvature and energetic position of, e.g., the lowest

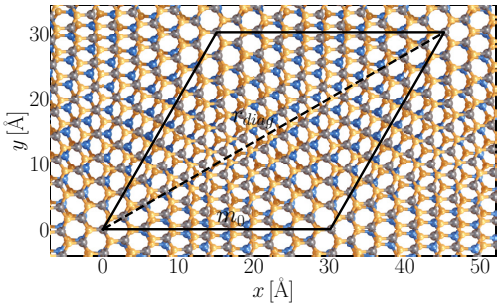

FIG. 1. WS_2 on MoS_2 twisted at an angle of 6.0°. Sulphur atoms are shown in orange, molybdenum in blue, and tungsten in grey. The moiré unit cell is shown with black solid lines and has a moiré period m_0 of 30.1 Å encompassing 546 atoms. The long diagonal r_{diag} is marked with a dashed black line.

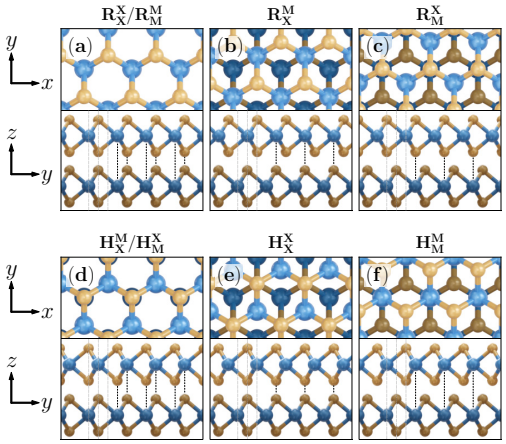

FIG. 2. The six high-symmetry stacking configurations of a bilayer with no lattice mismatch. (a)–(c) [(d)–(f)] belong to the R(H)-stacking group. The stacking R^X_X/R^M_M is also referred to as AA stacking, and H^M_X/H^X_M as AB stacking. The dotted black lines indicate atoms that coincide along z, justifying the naming convention.

conduction band and highest valence band are skewed on similar scales. In Ref. [28], the parameters are developed by fitting to DFT binding energies which will not guaranty the force-field model to reproduce the DFT relaxed structure. In this work, the structural parameters of the DFT optimized structures (i.e., atomic positions and unit cell size) are used directly as target values for the optimization of the force-field parameters. Furthermore, the KC parametrization of Ref. [28] is presented on a *per interaction basis*, meaning that atom-atom interactions are considered the same for different systems, e.g., S-S parameters for MoS_2 and WS_2 bilayers are the same. However, from a fundamental point of view, vdW interaction, being of long-range nature, is known to be sensitive to the surrounding environment. As such, we reparametrize the KC potential on a *per system basis*, which yields more accurate band structures. Furthermore, we expand the set of parameters to include heterobilayers with and without lattice mismatch, essentially covering all bilayer combinations of 2H-phased MX_2 for $M \in \{\text{Mo, W}\}$ and $X \in \{\text{S, Se, Te}\}$. However, the method presented here is, in principle, extendable to any 2D moiré structure and not limited to TMDs. Our force-field parameters, along with a variety of relaxed structures can be found via Ref. [38].

Lastly, we present two interpolation-based schemes to describe the *interlayer exciton moiré potential* of lattice-matched heterostructures with type-II band alignment by using a combination of the force-field method and DFT, which provides easy access to the potential for almost any angle. We extend this analogy to the binding energy, which allows for visualization of atomic reconstruction and the rate at which the reconstructed domains form with decreasing twist angle. Specifically, we see that atomic reconstruction becomes significant for angles below 4°–5° for the TMD heterostructures studied here.

II. METHODOLOGY

The first step is to develop the SW-parameters, which is done by considering the constituting monolayers one at a time. For 2H-phased TMD monolayers, the hexagonal symmetry reduces the structural degrees of freedom into two (target) parameters only, namely, the lattice constant, a_0, and the *intralayer* distance d_{intra}, i.e., the out-of-plane X-X distance. Therefore the SW-parametrization is carried out using a_0 and d_{intra} as targets and reproduces them extremely well. The force-field relaxations are performed using the LAMMPS package [39] and the optimization of parameters is carried out with use of the DAKOTA package [40].

For the optimization of the KC parameters, we are following two strategies, depending on whether the constituting layers are lattice matched or not.

A. Lattice matched bilayers

Bilayers that have the same chalcogen atom have a lattice constant mismatch $\delta \sim 0.1\%$ and are treated as lattice matched. In this case, only one additional structural parameter is considered, namely the *interlayer* spacing, d_{inter} (M-M distance). The KC parameters are obtained by fitting to a_0, d_{intra} and d_{inter} for the six high-symmetry stacking configurations (HSSCs), while keeping the SW parameters fixed. The HSSCs are depicted in Fig. 2 and are divided in two groups, namely, R and H stacking, which differ by a rotation of one of the layers by 60°. This procedure follows the idea that the mechanical properties of the single layer is well described by the SW potential and is not altered by the interlayer interaction (KC potential). It is crucial to derive a force field that is transferable between the different stacking since the twisted bilayers correspond to combinations of three different stacking, as will be demonstrated subsequently.

Moreover, as we will indirectly show in Sec. IV A, every subcell of a lattice-matched moiré unit cell is, to a certain extent, well described by a superposition of the HSSCs. Note, that this is not the case for lattice-mismatched systems where no local HSSCs can be identified. Justification of our methodology becomes trivial for smaller angles, where domains of the HSSCs make up a large fraction of the moiré unit cell.

TABLE I. Angles chosen for fitting lattice-mismatched structures accompanied by the lattice mismatch (δ, found using DFT), number of atoms (n_{atom}), and the moiré lattice constant m_0 (moiré period).

X^1	X^2	θ (°)	δ (%)	n_{atom}	m_0 (nm)
S	Se	5.68	4.1 ± 0.1	525	3.0
Se	Te	5.07	7.0 ± 0.1	471	3.0
S	Te	0.00	11.3 ± 0.1	543	3.2

Finally, the small unit cells constructed with merely six atoms, makes both DFT calculations and the optimization schemes of DAKOTA and LAMMPS relatively fast.

B. Lattice-mismatched bilayers

In Table I, we show the lattice mismatch δ for the different combinations of chalcogen atoms (the metal atom is nearly irrelevant for the lattice constant). The lattice mismatch of the systems investigated here (X = S, Se, and Te) is so large that the construction of small six atom unit cells as done in the lattice matched case is not meaningful. The in-plane strain will radically change the electronic properties [41].

To circumvent this problem, we use relatively small (about 500 atoms) moiré structures as targets for lattice-mismatched systems (see Table I). Due to the reduced symmetry of lattice-mismatched systems, the only valid targets are the coordinates of all atoms of the moiré unit cell combined with the lattice constant. However, using all atomic coordinates, i.e., three spatial dimensions for each atom, renders the mesh adaptive search scheme for optimizing the KC parameters infeasible, as the number of target values greatly exceeds the number of fitting parameters (Fig. 3, dashdotted green curve). As such, it is necessary to reduce the number of target values. However, considering only the three spatial coordinates of the metal atoms, thus reducing the target space by one third, also yields suboptimal KC parameters (Fig. 3, dotted blue curve). Lastly, optimizing only for the z coordinates of the metal atoms, which further reduces the target space by one third, results in a much better fit (Fig. 3, dashed red curve). As such, we ultimately choose the z coordinates of the metal atoms and the lattice constant as target values for lattice-mismatched systems, which yields satisfactory KC parameters, as discussed in Sec. III.

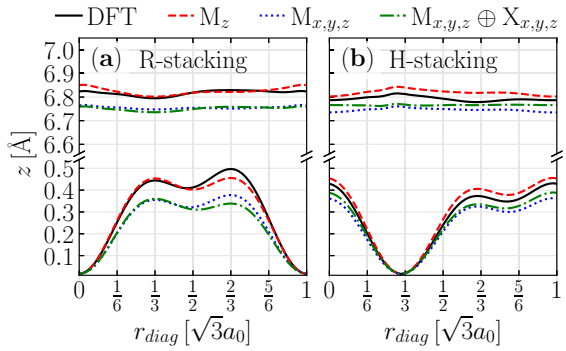

FIG. 3. z-coordinates of the metal atom in a 5.68° twisted WS_2-$MoSe_2$ bilayer along the long diagonal of the moiré unit cell, r_{diag}. The bottom curvy layer corresponds to WS_2, and the top more rigid layer corresponds to $MoSe_2$. The solid black curve is the DFT relaxed structure. The dashed red, dotted blue, and dashdotted green curves are force-field relaxed with KC parameters (see text). (a) and (b) show R and H stacking, respectively.

C. Kolmogorov-Crespi potential

As mentioned previously, the KC potential V_{ij} is intended to model interlayer effects between atom i in one layer and atom j in another, and is given by

$$
\begin{aligned}
V_{ij} &= e^{-\lambda(r_{ij}-z_0)}[C + f(\rho_{ij}) + f(\rho_{ji})] - A\left(\frac{r_{ij}}{z_0}\right)^{-6}, \\
\rho_{ij}^2 &= r_{ij}^2 - (\boldsymbol{n}_i \boldsymbol{r}_{ij})^2, \\
\rho_{ji}^2 &= r_{ij}^2 - (\boldsymbol{n}_j \boldsymbol{r}_{ij})^2, \\
f(\rho) &= e^{-(\rho/\delta)^2} \sum_{n=0}^{2} C_{2n} (\rho/\delta)^{2n}.
\end{aligned} \tag{1}
$$

$\boldsymbol{n}_i$ and $\boldsymbol{n}_j$ are the surface normals of the atom site i and j in each layer. The choice of neighbors used to determine the surface normals are the six nearest atoms in the respective strata (sublayer of the monolayer). The last term of V_{ij} contains the r^{-6} vdW dependence, and the first term has an exponentially decaying repulsion reflecting interlayer wave-function overlap. The square bracket functions contain a stacking dependent term, in contrast to, e.g., the Lennard-Jones potential [31]. As seen, V_{ij} leaves in total eight parameters to be fitted. As mentioned in Ref. [28], it is possible to approximate $\boldsymbol{n}_{i,j} = \hat{z}$ corresponding to completely rigid layers, however, we do not make use of this approximation in order to capture more accurately the corrugation caused by the relaxation.

D. Computational details

We parametrize the potentials with different combinations of exchange correlation plus vdW correction. We find that using PBE [42] from PSEUDODOJO [43,44] with Grimme's DFT-D3 vdW correction [45] plus Becke-Johnson damping [46] is best suited for parametrization. The structures are relaxed with QUANTUM ESPRESSO [47,48] using a k-space density of 15×15 (1×1) for high-symmetry (moiré) unit cells. DFT computations of moiré systems are performed without spin-orbit coupling (SOC) to save computational resources, since they are only used for comparing DFT to SW+KC relaxed structures. We find that the lattice constant only converges at a cutoff energy of 40 Ha in all cases. More importantly, the chosen cutoff energy should be consistent between monolayers, untwisted bilayers and moiré structured bilayers, when comparing DFT to SW+KC. We use the modified SW implementation in LAMMPS for ease of use. For optimization in DAKOTA, we apply a mesh adaptive direct search algorithm starting from the parameters presented in Ref. [28].

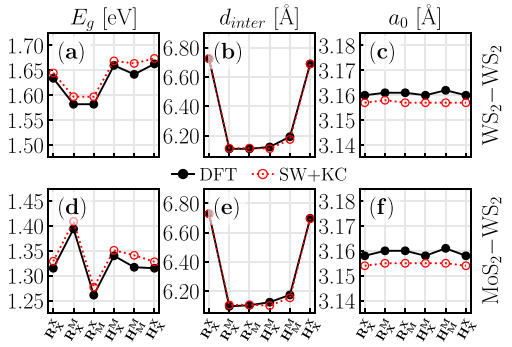

FIG. 4. Comparison of E_g at $\boldsymbol{K}_\pm$ in (a) and (d), interlayer spacing (d_{inter}) in (b) and (e), and lattice constant a_0 in (c) and (f) for the six HSSCs of a WS_2 homobilayer and a MoS_2-WS_2 heterobilayer in (a)–(c) (top) and (d)–(f) (bottom), respectively. DFT is marked with black and SW+KC with red.

III. RESULTS

For lattice-matched systems, i.e., homobilayers and heterobilayers having identical chalgogen sites in both layers, which are developed by use of the HSSCs, it is of high importance that the resulting structures can accurately reproduce the electronic properties. In Fig. 4, a comparison between purely DFT calculated parameters and SW+KC can be seen. Note that E_g shown in Figs. 4(a) and 4(d) is the energetically lowest momentum-conserving transition between the highest-lying valence band and the lowest-lying conduction band, which occurs at the $\boldsymbol{K}_\pm$ points for all stacking configurations and materials considered here. LAMMPS does not provide E_g, instead this is calculated using DFT with the relaxed structures generated by our SW+KC force-field method. Note, that for the purpose of consistency, we adopt the notation that MoS_2-WS_2 implies that WS_2 lies above MoS_2 with respect to z.

In the case of homobilayers, the maximum deviation of E_g is 22 meV, and occurs in the H_M^M stacking configuration. A similar maximum deviation of 25 meV is seen for the heterobilayer, which occurs in the H_M^M stacking configuration as well. For the remaining lattice-matched structures, the deviations are of similar magnitude. Figure 4 also demonstrates the high sensitivity of the band gap with respect to changes in the structural degrees of freedom.

Having established the SW+KC parameters of lattice-matched systems using the HSSCs, we now tackle some larger moiré structures. As such, we use some medium-scale moiré structures as benchmarks. Figure 5 shows comparisons between DFT- and SW+KC-relaxed band structures and interlayer spacing profiles for different material cases. Greek indices denote the corners of the mini Brillouin zone (BZ) associated with a moiré structured bilayer. The interlayer spacing is plotted along the long diagonal of the unit cell (see Fig. 1), which has a length of $\sqrt{3}m_0$, where m_0 denotes the moiré cell lattice constant. Figures 5(a)–5(d) displays the case of a WS_2-WS_2 homobilayer twisted at 6.0°. For R stacking [(a) and (b)], the bands are well represented using our SW+KC relaxed structure with only a 13 meV decrease of the band gap, likely due to the slight interlayer spacing profile discrepancy. In the case of H stacking [(c) and (d)], the same applies except the band gap is a mere 5 meV larger compared to the DFT relaxed structure results. In Figs. 5(e)–5(h), the case of a MoS_2-WS_2 heterobilayer with a twist angle of 6.0° is shown. For both R and H stacking [(e), (f) and (g), (h) respectively], an excellent agreement is obtained between DFT- and SW+KC-relaxed structures in terms of band character. For the higher lying conduction bands around the $\boldsymbol{\gamma}$ point, there is only a 10 meV discrepancy. We again attribute this to the slightly decreased interlayer spacing profiles of SW+KC in both cases, as seen in Figs. 5(f) and 5(h).

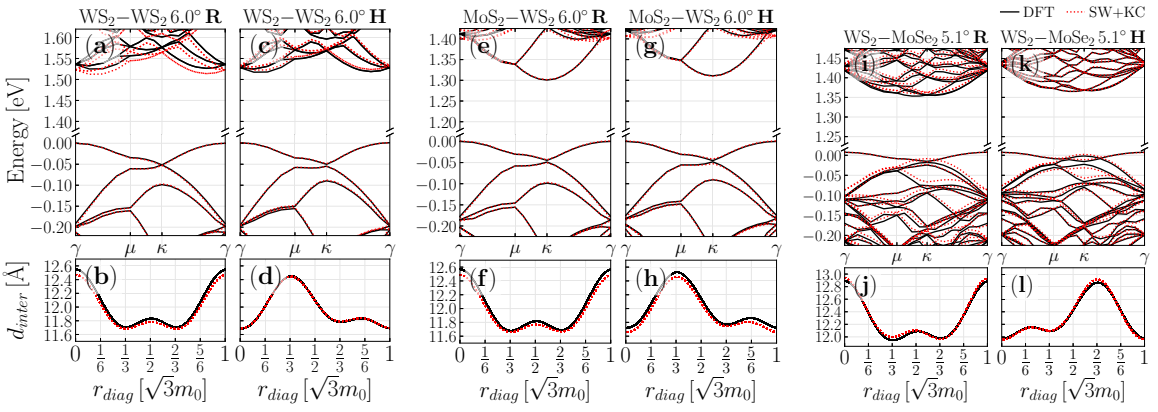

FIG. 5. Comparison of band structures and interlayer spacing profiles between DFT in solid black and SW+KC in dotted red. WS_2-WS_2 homobilayer with $\theta = 6.0°$ ($n_{\text{atom}} = 546$) in (a), (b) and (c), (d) for R and H stacking, respectively. MoS_2-WS_2 heterobilayer with $\theta = 6.0°$ ($n_{\text{atom}} = 546$) in (e), (f) and (g), (h) for R- and H stacking, respectively. WS_2-$MoSe_2$ lattice-mismatched heterobilayer with $\theta = 5.1°$ ($n_{\text{atom}} = 642$) in (i), (j) and (k), (l) for R and H stacking, respectively. The band structures have the valence band maximum shifted to 0 in all cases, and the Greek indices (γ, μ and κ) denote the high-symmetry points of the moiré (mini) BZ (usually denoted Γ, M and K in the BZ of the monolayer/untwisted bilayer). The interlayer spacing is interpolated and plotted along the long diagonal of the unit cell.

For lattice-mismatched systems, the optimization of the KC parameters was performed for all possible combinations of metal and chalcogen atoms, as explained in the methodology section (see Table I). A good agreement is obtained between the DFT- and SW+KC-relaxed structures for all lattice-mismatched cases. For the sake of brevity, only the case of a WS_2-$MoSe_2$ heterobilayer rotated at 5.1° is shown in Figs. 5(i)–5(l). For R stacking [(i) and (j)], the highest lying valence band is only 7 meV higher than the DFT value at the κ point. The lowest-lying conduction band is only 6 meV above the DFT one. In general, we see small discrepancies between the valence and conduction bands for the DFT and SW+KC-relaxed structures below 20 meV. For H stacking [(k) and (l)], the valence bands are well described except for a 4 meV discrepancy of the highest-lying valence band near the κ point.

In general, we note that the slight difference in band gap and band curvature between DFT and our SW+KC-relaxed moiré structures arise from small inaccuracies in the interlayer spacing profiles. Note, that this is not always the case with the KC parameters presented by Ref. [28], where the binding energy was the target property. We also find that the accuracy of our lattice-matched SW+KC parameters reduce with growing twist angle. This is expected, since we fit to the untwisted HSSCs, which are not well represented in moiré structures with such low periodicity. Conversely, the parameters are expected to have better accuracy with decreasing twist angle. For angles below 3°, where large-scale atomic reconstruction starts to appear, the accuracy of methodology is still maintained and most properties are well captured, including the atomic reconstructions, as discussed in Sec. V.

IV. APPROXIMATING MOIRÉ POTENTIALS

A defining feature of two-dimensional lattice-matched moiré structures is the spatial variation of local stacking order across the structure, leading to variation of local properties. Many combinations of TMDs possess type-II band alignment [49,50], and as such, the variation of the local band gap at $\boldsymbol{K}_\pm$ across the structure will, for many purposes, describe the *interlayer moiré potential* [17,27,51]. However, it is worth mentioning, that in the case of a large lattice mismatch between the constituting layers, developing such a potential becomes nontrivial.

We propose two interpolation-based methods for calculating the interlayer moiré potential of lattice-matched systems. Moreover, any electronic property that can be identified locally, can be accessed in the moiré structure directly with these two methods, e.g., variation of the VBM, CBM, etc. In both methods, the moiré supercell is subdivided into small units the size of the monolayer unit cell, for which local properties can be calculated. The first method, which we call the high-symmetry interpolation method (HSIM), is based on the *local high-symmetry stacking character*—a geometrical quantity that measures the similarity between the local stacking configuration within the moiré cell and the HSSCs. Being based only on the six HSSCs, computing the DFT properties is fast and allows for high-throughput computations. It also allows for easy visualization of reconstructed domains. The second method, which we call the grid based interpolation method (GBIM), relies on computing the local properties using DFT not only for the HSSCs but also every local stacking configuration in between, which can then be interpolated over the moiré supercell. In principle, this scheme is more precise, since it relies less on interpolation and more on *ab initio* calculations. However, it is time consuming, as many DFT computations using different in-plane displacements and interlayer spacing are needed. In what follows, both methods are explained in detail and case studies are shown.

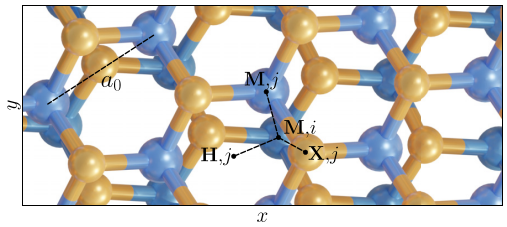

FIG. 6. Close-up of an R-stacked lattice-matched moiré structure for $\theta = 6.0°$. For a metal site i in one layer, the nearest transverse metal site, M, j, chalcogen site, X, j, and hexagonal center, H, j, in the adjacent layer is seen.

A. High-symmetry interpolation method (HSIM)

For every metal site in one layer, $\boldsymbol{\rho}_{M,i} = (x_{M,i}, y_{M,i})$, we find the transverse distance to the closest metal site in the adjacent layer, e.g., $d^M_{M,i} = \min(|\boldsymbol{\rho}_{M,i} - \boldsymbol{\rho}_{M,j}|)$, where j runs through every metal site in the adjacent layer (see Fig. 6). The largest distance possible is $a_0/\sqrt{3}$.

As such, we can define the parameter $c^M_{M,i} = 1 - \sqrt{3}d^M_{M,i}/a_0$, which is unity for perfectly aligned metal atoms, e.g., R^X_X- and H^M_M stacking, and zero for the remaining HSSCs. Eight analogous parameters can be developed, e.g.,

$$\left\{c^{\mathrm{S}_2}_{\mathrm{S}_1,i}(\boldsymbol{\rho}_{\mathrm{S}_1,i}) \quad \text{for} \quad \mathrm{S}_1, \mathrm{S}_2 \in \{M, X, \mathrm{H}\}\right\},$$

where X and H denote chalcogen sites and hexagonal centers, respectively. For the purpose of consistency, it is assumed that S_2 lies above S_1 with respect to z. $\{c^{\mathrm{S}_2}_{\mathrm{S}_1,i}\}$ is then interpolated on a skewed grid that spans the moiré unit cell. Stacking coefficients are now found as

$$\begin{aligned} C_{\mathrm{R}^X_X} &= c^M_M c^X_X c^{\mathrm{H}}_{\mathrm{H}}, \quad C_{\mathrm{H}^M_X} = c^M_X c^X_M c^{\mathrm{H}}_{\mathrm{H}}, \\ C_{\mathrm{R}^M_X} &= c^M_X c^X_{\mathrm{H}} c^{\mathrm{H}}_M, \quad C_{\mathrm{H}^X_X} = c^M_{\mathrm{H}} c^X_X c^{\mathrm{H}}_M, \\ C_{\mathrm{R}^X_M} &= c^M_{\mathrm{H}} c^X_M c^{\mathrm{H}}_X, \quad C_{\mathrm{H}^M_M} = c^M_M c^X_{\mathrm{H}} c^{\mathrm{H}}_X. \end{aligned}$$

Finally, the stacking coefficients are normalized such that $\sum_n C_n(\boldsymbol{\rho}) = 1$, where n spans the HSSCs. C_n is seen in Fig. 7 for R stacking. The C_n with $n \in \{\mathrm{H}^M_X, \mathrm{H}^X_X, \mathrm{H}^M_M\}$ are all 0 in this case. The next step is finding the interlayer spacing profile, $d_{\mathrm{inter}}(\boldsymbol{\rho})$, where $\boldsymbol{\rho} = (x, y)$. Using the variation of E_g, $E_g(\boldsymbol{\rho})$, as an example, it can be seen that

$$E_g(\boldsymbol{\rho}) = \sum_n C_n(\boldsymbol{\rho}) E_g(n, d_{\mathrm{inter}}(\boldsymbol{\rho})), \tag{2}$$

assuming the variation of E_g with d_{inter} is known for all HSSCs. Assuming that every subcell of the moiré structure

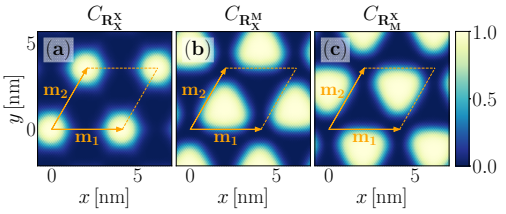

FIG. 7. Variation of $C_{R_X^X}$, $C_{R_X^M}$, and $C_{R_M^X}$ across an R-stacked MoS_2-WS_2 bilayer with $\theta = 4.41^\circ$ in (a), (b) and (c), respectively. The remaining coefficients are 0. The structure was relaxed using LAMMPS.

can be described by a superposition of HSSCs is an approximation, but has the benefit of easy visualization of domains, as seen in Fig. 7. It shows great accuracy and $E_g(n, d_{\text{inter}})$ can be extracted within few calculations, making it quite fast to implement for all lattice-matched systems.

B. Grid based interpolation method (GBIM)

A more general implementation can be developed by using the untwisted bilayer with a transverse shift $\boldsymbol{\rho}_s = (x_s, y_s)$ between the layers, where $\boldsymbol{\rho}_s = 0$ corresponds to either R_X^X- or H_M^M stacking. We calculate $E_g^{\text{BL}}(\boldsymbol{\rho}_s, d_{\text{inter}})$, where $\boldsymbol{\rho}_s$ is the transverse distance between metal sites in each layer. Then, for a given lattice-matched moiré system, for metal site i in one layer, we can find the vector $\boldsymbol{\rho}_i = \boldsymbol{\rho}_{M,j} - \boldsymbol{\rho}_{M,i}$, where j denotes the index of the nearest metal site in the adjacent layer. Then, the value of E_g at metal site i is simply

$$E_g(\boldsymbol{\rho}_{M,i}) = E_g^{\text{BL}}(\boldsymbol{\rho}_i, d_{\text{inter}}(\boldsymbol{\rho}_{M,i})). \tag{3}$$

Note, that $\boldsymbol{\rho}_i$ should be adjusted relative to the rotation of the individual layers, since the layers will likely be slightly angled compared to the systems used in computing $E_g^{\text{BL}}(\boldsymbol{\rho}_s, d_{\text{inter}})$. Finally, E_g is interpolated over the entire moiré unit cell.

In principle, the GBIM should be more accurate than the HSIM, but is also computationally more expensive. We use twelve steps for x_s and y_s combined with sixteen increments for d_{inter} when tabulating $E_g^{\text{BL}}(\boldsymbol{\rho}_s, d_{\text{inter}})$. This translates to 4608 separate DFT calculations to cover R and H stacking for one material, whereas the HSIM needs only 96. In Fig. 8, a comparison between the HSIM and the GBIM can be seen

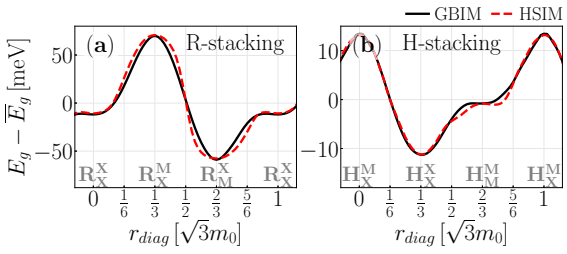

FIG. 8. Variation of E_g along the long diagonal of an R- and H-stacked MoS_2-WS_2 bilayer with $\theta = 4.41^\circ$ in (a) and (b), respectively. The solid black and dashed red curves represent band-gap variation found using the GBIM and HSIM, respectively.

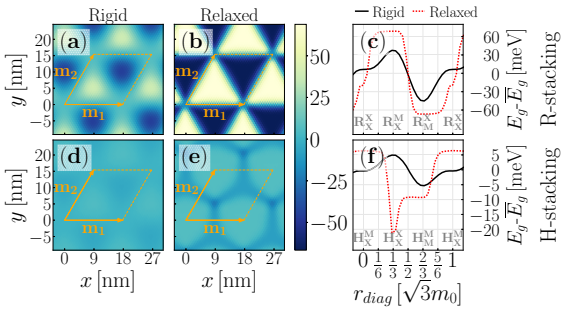

FIG. 9. Variation of E_g at $\boldsymbol{K}_\pm$ across a 1.01° twisted R-stacked MoS_2-WS_2 bilayer without and with relaxation effects in the (a), (d) and (b), e), respectively. Comparison between the two cases along the long diagonal of the moiré unit cells in (c) and (f). (a)–(c) and (d)–(e) represent R and H stacking, respectively.

for the variation of E_g in MoS_2-WS_2 with $\theta = 4.41^\circ$. At the high-symmetry points, both methods yield the same value as expected, but the HSIM is slightly inaccurate in between.

V. ATOMIC RECONSTRUCTION AND ENERGETIC LANDSCAPE

As mentioned, the energetic landscape of 2D moiré structures is constituted by three codependent factors: the local stacking arrangement, the associated interlayer spacing, and the atomic reconstruction. Often, the latter two, being relaxation effects, are not considered in simulations [11,15,17,51–62], but can be managed with SW+KC force-field relaxation.

For MoS_2-WS_2, which possesses type-II band alignment [49,50], the interlayer moiré potential is often described as the spatial variation of the local band gap at $\boldsymbol{K}_\pm$. In Fig. 9, the variation of $E_g - \overline{E}_g$ across an R- and H-stacked MoS_2-WS_2 bilayer with $\theta = 1.01^\circ$ is seen, where $\overline{E}_g$ is the mean value across the unit cell. In the rigidly twisted case, the average interlayer spacing of the three R- or H-stacked HSSCs are used as interlayer spacing for Figs. 9(a) and 9(d), respectively. The discrepancy between modeling the potential with- and without relaxation effects is apparent. In the case of R stacking, which has larger potential depth than H stacking, the depth with- and without relaxation effects are here estimated to be 80 and 135 meV, respectively. For H stacking, these numbers are much lower, namely 10 and 28 meV for rigid and relaxed, respectively. As a consequence, phenomena such as exciton trapping may be realized more easily in R-stacked systems than H-stacked analogs. Interestingly, for H stacking, the minimum of the potential resides in the H_X^X-domain postrelaxation as opposed to the H_M^M-domain prerelaxation. Finally, the effect of atomic reconstruction also greatly changes the relative widths of the potential wells, resulting in a sharper and more well-defined potential. We conclude that atomic reconstruction significantly alters the range of θ in which exciton trapping occurs.

In Table II, the *interlayer binding energy per atom*, E_b, found as $E_b = (E_{\text{MoS}_2\text{-WS}_2} - E_{\text{MoS}_2} - E_{\text{WS}_2})/6$ is shown, where $E_{\text{MoS}_2\text{-WS}_2}$ is the total energy of the untwisted bilayer system, and E_{MoS_2} and E_{WS_2} denote the total energies of

TABLE II. Binding energy of MoS_2-WS_2 in the six high-symmetry stacking configurations from DFT and from SW+KC.

E_b (meV)	R_X^X	R_M^X	R_X^M	H_X^M	H_X^X	H_M^M
DFT	−21.8	−34.3	−34.5	−34.6	−22.4	−31.6
SW+KC	−25.4	−44.4	−44.6	−44.7	−28.9	−38.4

constituting monolayers found separately. As mentioned, the discrepancy in E_b between DFT and SW+KC is expected, since this was not the target property during development of our KC parameters.

For R stacking, the nearly identical E_b of the R_M^X and R_X^M configurations facilitates a simultaneous growth of these domains with decreasing θ (i.e., large moiré unit cells), while the opposite is true for R_X^X, explaining the formation of a mesh of triangular domains, as seen in Fig. 9(b). For H stacking, the H_X^M configuration is energetically favorable, resulting in hexagonal domains with decreasing θ. The H_M^M-like domains shrink slower than those associated with H_X^X, as seen from the associated E_b (see also Ref. [63]).

Lastly, $E_b(\theta)$ can be considered in order to access the formation rate of domains. Using the HSIM, the variation of the local E_b across a moiré unit cell can be approximated, and the mean can be used to approximate E_b of the moiré unit cell, albeit neglecting the effects of strain imposed by atomic reconstruction and corrugation from the varying interlayer spacing. In the case of pure DFT, E_b, is found directly as

$$E_b = E_{\text{moiré}} - (E_{\text{MoS}_2} + E_{\text{WS}_2})/2, \tag{4}$$

where all energies are divided by the number of atoms, and $E_{\text{moiré}}$ denotes the total energy per atom of the moiré structure. However, E_b has contributions from the strain imposed by layer corrugation and atomic reconstruction. The energy associated with these effects is denoted E_{corr} and is not captured by the HSIM. Instead, the E_b found by the HSIM should be compared to

$$E_b - E_{\text{corr}} = E_{\text{moiré}} - (E_{\text{MoS}_2,\text{moiré}} + E_{\text{WS}_2,\text{moiré}})/2, \tag{5}$$

where $E_{\text{MoS}_2,\text{moiré}}$ and $E_{\text{WS}_2,\text{moiré}}$ denote the total energy per atom for the corrugated and reconstructed constituting monolayers. This is computed in separate DFT calculations having half the number of atoms as the moiré structure they constitute.

With SW+KC, E_b is found analogously to Eq. (4), but E_{corr} is found directly by comparing the energy of the SW potential in the two layers to that of the constituting rigid monolayers. The variation of these quantities with θ is seen in Fig. 10.

A common feature for all energy scales in Fig. 10 is the tendency towards the value of the stable configurations for $\theta \to 0$. For vanishing θ, the relative size of the domain walls becomes negligible. As such, E_{corr} should vanish in the limit of vanishing θ. The faster convergence towards the E_b of R_X^M/R_M^X for R stacking indicates that the triangular domains form more rapidly with decreasing θ compared to the hexagonal H_X^M domains of H stacking. Although the values of $E_b^{\text{SW+KC}}$ and $E_{\text{corr}}^{\text{SW+KC}}$ may appear off scale, they illustrate the tendencies faithfully. Additionally, the graph of $E_b^{\text{DFT}} - E_{\text{corr}}^{\text{DFT}}$ serves as a benchmark, showing that the HSIM has accuracy within

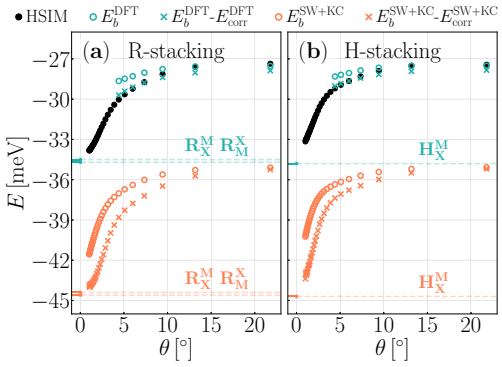

FIG. 10. $E_b(\theta)$ for MoS_2-WS_2. (a) and (b) are for R and H stacking, respectively. Black points are found using the HSIM on the SW+KC-relaxed structures, but with DFT-based parametrization of the HSIM as seen in Eq. (2).

the 0.5 meV range, and further that E_b of SW+KC relaxed structures can be recovered to agree with DFT.

Figure 11 shows the mean of the stacking coefficients C_n over the moiré unit cell of MoS_2-WS_2, which can be computed using the HSIM as described in Sec. IV A. C_n represents the normalized contributions of the different stacking configurations to the fully relaxed (reconstructed) moiré structure. For R stacking (H stacking), the three possible domains are: R_M^X (green), R_X^X (red), R_X^M (blue) [H_M^M (green), H_X^X (red), H_X^M (blue)]. For larger angles, the fraction of the unit cell area occupied by each of the three domains is about 1/3 for both R and H stacking. At an angle of 1°, the structure for R stacking [Fig. 11(a)] is already reconstructed in such a way that the energetically less favorable R_X^X (red) domains represent only 2,5% of the structure. Both R_M^X (green) and R_X^M (blue) domains are energetically equivalent, and hence, occupy roughly 50% of the structure in the limit of small θ. For H stacking [Fig. 11(b)], at the same angle of 1°, the less favorable H_X^X and H_M^M domains have significantly reduced contributions compared to the favorable H_X^M region, but H_M^M still represents 20% of overall structure.

Figure 11 allows us to draw quantitative conclusions on the angle dependence of the reconstruction effect. Indeed, neglecting reconstructions would lead to a constant equal proportion of all three coexisting stacking (dotted lines in

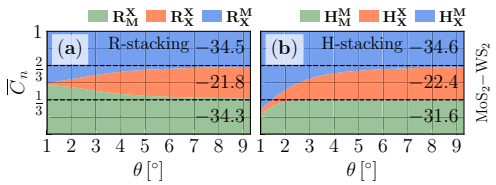

FIG. 11. The mean of C_n over the unit cell with respect to the twist angle θ of MoS_2-WS_2 found using SW+KC and the HSIM. (a) correspond to R stacking such that only R_X^X, R_M^X, and R_X^M are nonzero and vice versa for (b). For each stacking configuration, the corresponding E_b of untwisted MoS_2-WS_2 is shown in meV.

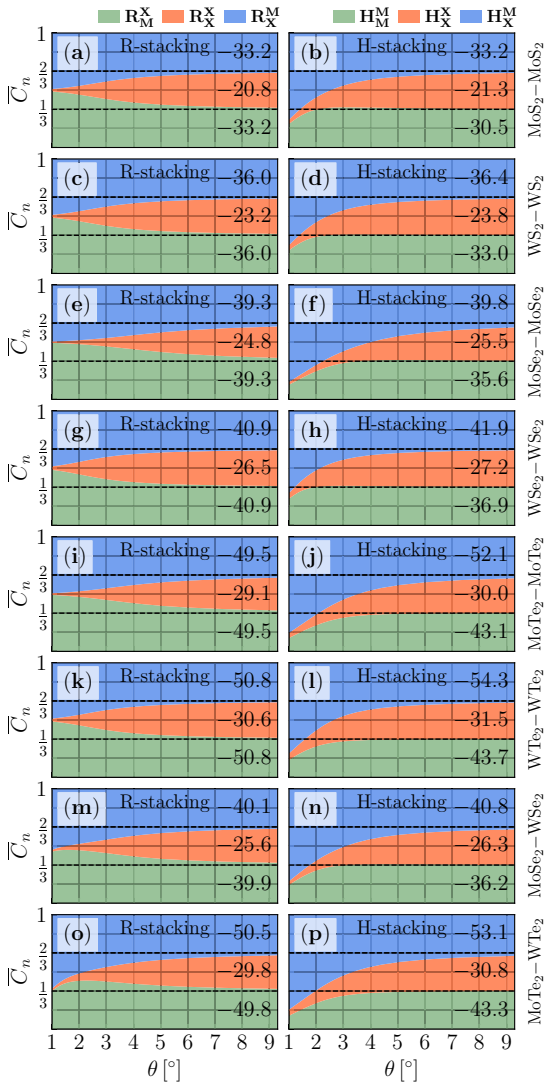

FIG. 12. The mean of C_n over the unit cell with respect to the twist angle θ of eight lattice-matched bilayers found using SW+KC and the HSIM. Left panels correspond to R stacking such that only R^X_X, R^X_M, and R^M_X are nonzero and vice versa for right panels. For each material and stacking configuration, the corresponding E_b of the untwisted bilayer is shown in meV.

Fig. 11). In the case of R stacking the reconstruction is nearly complete at an angle of 1°, i.e., the moire structure is made of basically two type of low energy domains [R^X_M (green), R^M_X (blue)] separated by a very narrow R^X_X(red) energetically unfavorable domain. For H stacking at 1°, the less favorable H^M_M (green) domain still covers 15%–20% of the area.

Figure 12 shows the same graph as Fig. 11 for the remaining eight lattice-matched materials. Generally, all R-stacked materials (left panels of Fig. 12) display a simultaneous growth of R^X_M and R^M_X with decreasing θ except for $MoTe_2$-WTe_2, which can be attributed to the discrepancy in E_b for these stacking configurations. We conclude that for both stacking and all materials considered here, except for $MoSe_2$-$MoSe_2$, that atomic reconstruction becomes especially prominent below an angle of 4°–5°. For $MoSe_2$-$MoSe_2$, atomic reconstruction occurs for angles below 6°–7°.

VI. CONCLUSION

In conclusion, we have shown the dramatic consequences of incorporating relaxation effects on the *interlayer moiré potential* of MoS2-WS_2. For R stacking, this becomes about twice as deep at about 135 meV, and, for small angles, much wider. For H stacking, the potential depth is nearly tripled, however, the width of the potential minima is still narrow, since it corresponds to the energetically unfavorable H^X_X configuration. Moreover, we have quantified the formation rate of domains due to atomic reconstruction for nine lattice-matched TMD moiré systems, and conclude that, in general, atomic reconstruction becomes prominent for θ smaller than 4°–5°, but does so in a continuous manner.

Furthermore, we have presented a methodology for developing KC parameters for lattice-matched and -mismatched systems, and have developed such parameters for TMD moiré heterostructures. The method shows excellent agreement between DFT-calculated structural parameters and SW+KC-relaxed ones, which is further reflected in the bandstructure and the *interlayer binding energy* with twist angle dependence. The force-field parameters along with a variety of relaxed structures can be found via Ref. [38]. We have further shown two methods for capturing moiré induced fluctuations of local properties in lattice-matched systems that do not require extensive *ab initio* treatment. These methods allow for visualization of the importance of relaxation effects and further serve as a first step in developing accurate moiré potentials. However, further investigation is required to develop analogous tools for lattice-mismatched moiré structures.

In summary, starting from the force-field model, it is now possible to tackle excited state physics incorporating relaxation effects i.e., layer corrugation and atomic reconstruction. For models such as tight binding, this was not possible before, and for *ab initio* studies, the cumbersome first step of relaxation can be skipped, thus saving computational resources and time. Furthermore, a thorough dissection of the formation rate of domains with decreasing angle is required to gain quantitative insight into the mechanisms behind it.

ACKNOWLEDGMENTS

The project is supported by the Deutsche Forschungsgemeinschaft (DFG) within the Priority Program SPP2244 2DMP and by the Cluster of Excellence "Advanced Imaging of Matter" of the Deutsche Forschungsgemeinschaft (DFG) – EXC 2056 – project ID 390715994.

[1] Y. Liu, N. O. Weiss, X. Duan, H.-C. Cheng, Y. Huang, and X. Duan, Nat. Rev. Mater. **1**, 16042 (2016).

[2] K. S. Novoselov, A. Mishchenko, A. Carvalho, and A. H. C. Neto, Science **353**, aac9439 (2016).

[3] M. Gibertini, M. Koperski, A. F. Morpurgo, and K. S. Novoselov, Nat. Nanotechnol. **14**, 408 (2019).

[4] X. Yao, Y. Wang, and S. Dong, Int. J. Mod. Phys. B **35**, 2130004 (2021).

[5] R. Bistritzer and A. H. MacDonald, Proc. Natl. Acad. Sci. USA **108**, 12233 (2011).

[6] I. A. M. Al-Ani, K. As'ham, O. Klochan, H. T. Hattori, L. Huang, and A. E. Miroshnichenko, J. Opt. **24**, 053001 (2022).

[7] M. H. Naik and M. Jain, Phys. Rev. Lett. **121**, 266401 (2018).

[8] J. Choi, W.-T. Hsu, L.-S. Lu, L. Sun, H.-Y. Cheng, M.-H. Lee, J. Quan, K. Tran, C.-Y. Wang, M. Staab, K. Jones, T. Taniguchi, K. Watanabe, M.-W. Chu, S. Gwo, S. Kim, C.-K. Shih, X. Li, and W.-H. Chang, Sci. Adv. **6**, eaba8866 (2020).

[9] H. Baek, M. Brotons-Gisbert, Z. X. Koong, A. Campbell, M. Rambach, K. Watanabe, T. Taniguchi, and B. D. Gerardot, Sci. Adv. **6**, eaba8526 (2020).

[10] H. Guo, X. Zhang, and G. Lu, Sci. Adv. **6**, eabc5638 (2020).

[11] F. Wu, T. Lovorn, E. Tutuc, and A. H. MacDonald, Phys. Rev. LDowett. **121**, 026402 (2018).

[12] Y. Tang, L. Li, T. Li, Y. Xu, S. Liu, K. Barmak, K. Watanabe, T. Taniguchi, A. H. MacDonald, J. Shan, and K. F. Mak, Nature **579**, 353 (2020).

[13] H. Pan, F. Wu, and S. Das Sarma, Phys. Rev. B **102**, 201104(R) (2020).

[14] K. Slagle and L. Fu, Phys. Rev. B **102**, 235423 (2020).

[15] H. Pan, F. Wu, and S. Das Sarma, Phys. Rev. Res. **2**, 033087 (2020).

[16] E. C. Regan, D. Wang, C. Jin, M. I. Bakti Utama, B. Gao, X. Wei, S. Zhao, W. Zhao, Z. Zhang, K. Yumigeta, M. Blei, J. D. Carlström, K. Watanabe, T. Taniguchi, S. Tongay, M. Crommie, A. Zettl, and F. Wang, Nature **579**, 359 (2020).

[17] N. Götting, F. Lohof, and C. Gies, Phys. Rev. B **105**, 165419 (2022).

[18] M. R. Rosenberger, H.-J. Chuang, M. Phillips, V. P. Oleshko, K. M. McCreary, S. V. Sivaram, C. S. Hellberg, and B. T. Jonker, ACS Nano **14**, 4550 (2020).

[19] S. Carr, D. Massatt, S. B. Torrisi, P. Cazeaux, M. Luskin, and E. Kaxiras, Phys. Rev. B **98**, 224102 (2018).

[20] I. Maity, P. K. Maiti, H. R. Krishnamurthy, and M. Jain, Phys. Rev. B **103**, L121102 (2021).

[21] V. V. Enaldiev, V. Zólyomi, C. Yelgel, S. J. Magorrian, and V. I. Fal'ko, Phys. Rev. Lett. **124**, 206101 (2020).

[22] H. Li, S. Li, M. H. Naik, J. Xie, X. Li, J. Wang, E. Regan, D. Wang, W. Zhao, S. Zhao, S. Kahn, K. Yumigeta, M. Blei, T. Taniguchi, K. Watanabe, S. Tongay, A. Zettl, S. G. Louie, F. Wang, and M. F. Crommie, Nat. Mater. **20**, 945 (2021).

[23] A. Weston, Y. Zou, V. Enaldiev, A. Summerfield, N. Clark, V. Zólyomi, A. Graham, C. Yelgel, S. Magorrian, M. Zhou, J. Zultak, D. Hopkinson, A. Barinov, T. H. Bointon, A. Kretinin, N. R. Wilson, P. H. Beton, V. I. Fal'ko, S. J. Haigh, and R. Gorbachev, Nat. Nanotechnol. **15**, 592 (2020).

[24] S. Shabani, D. Halbertal, W. Wu, M. Chen, S. Liu, J. Hone, W. Yao, D. N. Basov, X. Zhu, and A. N. Pasupathy, Nat. Phys. **17**, 720 (2021).

[25] J. Sung, Y. Zhou, G. Scuri, V. Zólyomi, T. I. Andersen, H. Yoo, D. S. Wild, A. Y. Joe, R. J. Gelly, H. Heo, S. J. Magorrian, D. Bérubé, A. M. M. Valdivia, T. Taniguchi, K. Watanabe, M. D. Lukin, P. Kim, V. I. Fal'ko, and H. Park, Nat. Nanotechnol. **15**, 750 (2020).

[26] Y. Liu, C. Zeng, J. Yu, J. Zhong, B. Li, Z. Zhang, Z. Liu, Z. M. Wang, A. Pan, and X. Duan, Chem. Soc. Rev. **50**, 6401 (2021).

[27] W. T. Geng, V. Wang, Y. C. Liu, T. Ohno, and J. Nara, J. Phys. Chem. Lett. **11**, 2637 (2020).

[28] M. H. Naik, I. Maity, P. K. Maiti, and M. Jain, J. Phys. Chem. C **123**, 9770 (2019).

[29] F. H. Stillinger and T. A. Weber, Phys. Rev. B **31**, 5262 (1985).

[30] J.-W. Jiang and Y.-P. Zhou, *Handbook of Stillinger-Weber Potential Parameters for Two-Dimensional Atomic Crystals* (IntechOpen, Rijeka, 2017), Chap. 1.

[31] A. N. Kolmogorov and V. H. Crespi, Phys. Rev. B **71**, 235415 (2005).

[32] A. N. Kolmogorov and V. H. Crespi, Phys. Rev. Lett. **85**, 4727 (2000).

[33] T. Maaravi, I. Leven, I. Azuri, L. Kronik, and O. Hod, J. Phys. Chem. C **121**, 22826 (2017).

[34] I. Leven, T. Maaravi, I. Azuri, L. Kronik, and O. Hod, J. Chem. Theory Comput. **12**, 2896 (2016).

[35] I. Leven, I. Azuri, L. Kronik, and O. Hod, J. Chem. Phys. **140**, 104106 (2014).

[36] W. Ouyang, D. Mandelli, M. Urbakh, and O. Hod, Nano Lett. **18**, 6009 (2018).

[37] W. Ouyang, R. Sofer, X. Gao, J. Hermann, A. Tkatchenko, L. Kronik, M. Urbakh, and O. Hod, J. Chem. Theory Comput. **17**, 7237 (2021).

[38] Force-field parameters, https://www.chemie.uni-hamburg.de/en/institute/pc/arbeitsgruppen/bester/downloads.html.

[39] A. P. Thompson, H. M. Aktulga, R. Berger, D. S. Bolintineanu, W. M. Brown, P. S. Crozier, P. J. in 't Veld, A. Kohlmeyer, S. G. Moore, T. D. Nguyen, R. Shan, M. J. Stevens, J. Tranchida, C. Trott, and S. J. Plimpton, Comput. Phys. Commun. **271**, 108171 (2022).

[40] M. Eldred, K. Dalbey, W. Bohnhoff, B. Adams, L. Swiler, P. Hough, D. Gay, J. Eddy, and K. Haskell, DAKOTA: A multilevel parallel object-oriented framework for design optimization, parameter estimation, uncertainty quantification, and sensitivity analysis, Version 5.0, User's manual, Technical Report No. SAND2010-2183 (OSTI, USA, 2010), https://www.osti.gov/biblio/991842/.

[41] H. Shi, H. Pan, Y.-W. Zhang, and B. I. Yakobson, Phys. Rev. B **87**, 155304 (2013).

[42] J. P. Perdew, K. Burke, and M. Ernzerhof, Phys. Rev. Lett. **77**, 3865 (1996).

[43] M. van Setten, M. Giantomassi, E. Bousquet, M. Verstraete, D. Hamann, X. Gonze, and G.-M. Rignanese, Comput. Phys. Commun. **226**, 39 (2018).

[44] D. R. Hamann, Phys. Rev. B **88**, 085117 (2013).

[45] S. Grimme, J. Antony, S. Ehrlich, and H. Krieg, J. Chem. Phys. **132**, 154104 (2010).

[46] A. D. Becke and E. R. Johnson, J. Chem. Phys. **124**, 221101 (2006).

[47] P. Giannozzi, S. Baroni, N. Bonini, M. Calandra, R. Car, C. Cavazzoni, D. Ceresoli, G. L. Chiarotti, M. Cococcioni, I. Dabo, A. D. Corso, S. de Gironcoli, S. Fabris, G. Fratesi, R. Gebauer, U. Gerstmann, C. Gougoussis, A. Kokalj, M. Lazzeri, L. Martin-Samos *et al.* J. Phys.: Condens. Matter **21**, 395502 (2009).

[48] P. Giannozzi, O. Andreussi, T. Brumme, O. Bunau, M. B. Nardelli, M. Calandra, R. Car, C. Cavazzoni, D. Ceresoli, M. Cococcioni, N. Colonna, I. Carnimeo, A. D. Corso, S. de Gironcoli, P. Delugas, R. A. DiStasio Jr, A. Ferretti, A. Floris, G. Fratesi, G. Fugallo *et al.*, J. Phys.: Condens. Matter **29**, 465901 (2017).
[49] V. O. Özçelik, J. G. Azadani, C. Yang, S. J. Koester, and T. Low, Phys. Rev. B **94**, 035125 (2016).
[50] C. Zhang, C. Gong, Y. Nie, K.-A. Min, C. Liang, Y. J. Oh, H. Zhang, W. Wang, S. Hong, L. Colombo, R. M. Wallace, and K. Cho, 2D Mater. **4**, 015026 (2016).
[51] F. Wu, T. Lovorn, and A. H. MacDonald, Phys. Rev. B **97**, 035306 (2018).
[52] F. Wu, T. Lovorn, and A. H. MacDonald, Phys. Rev. Lett. **118**, 147401 (2017).
[53] L. Rademaker, Phys. Rev. B **105**, 195428 (2022).
[54] H. Yu, G.-B. Liu, J. Tang, X. Xu, and W. Yao, Sci. Adv. **3**, e1701696 (2017).
[55] A. Hichri, T. Amand, and S. Jaziri, Phys. Rev. Mater. **5**, 114002 (2021).
[56] C. Lagoin and F. Dubin, Phys. Rev. B **103**, L041406 (2021).
[57] K. Tran, G. Moody, F. Wu, X. Lu, J. Choi, K. Kim, A. Rai, D. A. Sanchez, J. Quan, A. Singh, J. Embley, A. Zepeda, M. Campbell, T. Autry, T. Taniguchi, K. Watanabe, N. Lu, S. K. Banerjee, K. L. Silverman, S. Kim *et al.*, Nature **567**, 71 (2019).
[58] Z. Li, X. Lu, D. F. Cordovilla Leon, Z. Lyu, H. Xie, J. Hou, Y. Lu, X. Guo, A. Kaczmarek, T. Taniguchi, K. Watanabe, L. Zhao, L. Yang, and P. B. Deotare, ACS Nano **15**, 1539 (2021).
[59] H. Zheng, D. Zhai, and W. Yao, 2D Mater. **8**, 044016 (2021).
[60] D. Zhai and W. Yao, Phys. Rev. Mater. **4**, 094002 (2020).
[61] S. Brem, C. Linderälv, P. Erhart, and E. Malic, Nano Lett. **20**, 8534 (2020).
[62] F. Wu, T. Lovorn, E. Tutuc, I. Martin, and A. H. MacDonald, Phys. Rev. Lett. **122**, 086402 (2019).
[63] D. Halbertal, N. R. Finney, S. S. Sunku, A. Kerelsky, C. Rubio-Verdú, S. Shabani, L. Xian, S. Carr, S. Chen, C. Zhang, L. Wang, D. Gonzalez-Acevedo, A. S. McLeod, D. Rhodes, K. Watanabe, T. Taniguchi, E. Kaxiras, C. R. Dean, J. C. Hone, A. N. Pasupathy *et al.*, Nat. Commun. **12**, 242 (2021).

5
Conclusion & Outlook

In this thesis, an advanced *ab initio* many-body methodology was developed and utilized to deepen the understanding of excited state phenomena in two-dimensional TMDs and their heterostructures. By integrating a CI approach with DFT and sophisticated screening effects, highly accurate predictions of excited-state properties have been achieved, including binding energies, fine-structure splittings and optical oscillator strengths.

Our analysis of the excited states in monolayer WSe_2 demonstrated excellent agreement with experimental findings for many-body composites with all carriers located in the **K**-valley. Building on this validated foundation, we then predicted energetically more favorable negatively charged trions involving the **Q**-valley. This insight provides a deeper understanding of valley-dependent excitonic states and highlights their potential for external manipulation in optoelectronic applications.

Furthermore, in vertical TMD Janus heterostructures such as MoSSe–WSSe and WSSe–WSSe, it was demonstrated that intrinsic asymmetry and interface-induced polarization can dramatically alter the band structure, enabling bright excitonic ground states not found in conventional TMD bilayers. These findings show that by tuning stacking configurations and applying external strain, it is possible to manipulate and optimize the optical properties of these materials, paving the way for the design of highly efficient, tunable light-emitting and detecting devices.

Lastly, for moiré structured TMD bilayers, a powerful toolset for capturing the complex relaxation effects associated with such systems was developed. The significant role of in-plane atomic reconstructions was quantified, and, consequentially, it was shown how the potential landscape is impacted. It was demonstrated how this effect became increasingly prominent with smaller twist angles, which in turn will influence the localization of excitonic compounds. Therefore, these results lay the groundwork for future research into many-body complexes in moiré heterostructures.

This work provides a comprehensive framework for understanding and engineering many-body effects in 2D materials through structural and external parameters. The methodologies developed here build the foundation for future explorations into more complex heterostructures, such as moiré structured TMDs,

lateral heterostructures and many more. Additionally, extending the work to include excitonic interactions under external stimuli, such as magnetic fields or dynamic strain, could open new avenues for actively controlling quantum states. Overall, this research not only advances fundamental insights into many-body physics in 2D systems but also provides practical strategies for the design of next-generation optoelectronic, quantum, and valleytronic devices based on layered 2D materials.

Appendices

A
The MX-package

Contents

In the Methodology (Chapter 3), the implementation of the CI procedure was described in detail. However, the procedure itself is implemented in a FORTRAN-based code package with several features, which is documented here in slightly more detail. The code itself is called the MX-package and is constituted of three main programs that should be executed sequentially. They are summarized in the following:

- MXMAT builds the configurational space and computes the non-zero CI matrix elements featured in the Hamiltonian of Eq. (2.43).
- MXCI builds and diagonalizes the CI matrix and returns the CI eigenvalues and configurational coefficients (eigenvectors).
- MXPP is a post-processing tool and has several usages, which will be described in more detail in the following.

Both MXMAT, MXCI, and several components of MXPP are built with MPI compatibility and can therefore be executed in parallel.

The general workflow of the calculations described in Chapter 3 is outlined in Fig. A.1. The first step is an SCF calculation, which must be computed within the Quantum Espresso suite, since no other wavefunction readers are yet implemented. This will return the Kohn-Sham eigenvalues and wavefunctions, which are then used in a YAMBO calculation to compute the inverse static dielectric screening function, $\epsilon^{-1}_{GG'}$, and optionally the self-energy corrected GW eigenvalues. From here, all the prerequisite calculations are essentially finished, and the MX-package can be used to its full extent.

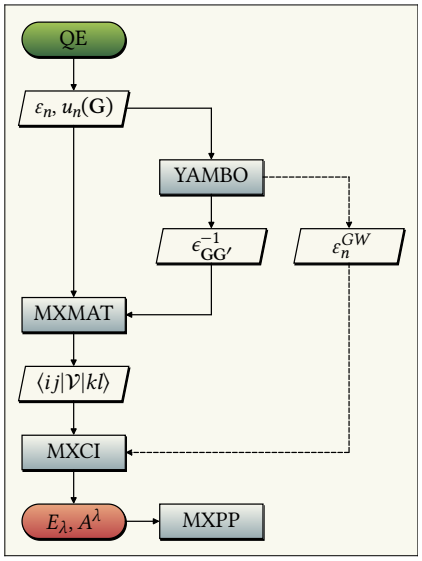

Figure A.1: The general workflow of CI calculation using the MX-package. The $\mathcal{V}$ can denote either the unscreened Coulomb kernel, V, or the screened one, W.

This part of the thesis is meant to serve as a miniature documentation of the MX-package, and in the coming section, a more detailed instruction for the use of the MX-package executable is provided. Currently, the code is not open-source, but is available upon reasonable request. If the reader is not interested in running the code, this appendix can be skipped without loss of coherence.

A.1 MXMAT

The input file for MXMAT will generally be structured as

```
&state_control
    nholes = 1
    nelecs = 2
    val    = -2
    con    = -4
    Q_com  = 0.3333333, -0.3333333, 0.0000000

    k_sphere   = .true.
    k_nspheres = 1
    k_center   = 192
    k_radius   = 0.20
/
&io
    wfc_format = 'qe'
    job_dir    = 'data'
    verbose    = .true.
    overwrite  = .false.

    wfc_path = '/path/to/wfc'
    xml_path = '/path/to/data-file-schema.xml'
    eps_path = '/path/to/ndb.em1s'
/
...
```

The most important parameters are those listed in `&state_control`, which reflect the methods described in Chapter 3. The two most dictating variables, `nholes` and `nelecs` describe the number of excited holes and electrons, respectively, and thus dictate the level of EDs in the truncated CI formalism. The specific choice seen here corresponds to a negatively charged trion calculation. Next, `val` and `con` dictates the window of valence and conduction bands used to build the configurational space. In this case, `val = -2` means that the two energetically highest valence bands are used and vice versa for `con = -4`. Alternatively, specific bands may be chosen for either parameter, which are given as a list of band indices. As described in Eq. (3.34), the variable `Q_com` controls the center-of-mass momentum used to build the configurations, and is given in reduced reciprocal coordinates. The one given here corresponds to the K-point. Lastly, as seen in Fig. 3.5, it can sometimes be advantageous to only use a specific subset of k-points. This can be controlled through the four parameters `k_sphere`, `k_nspheres`, `k_center` and `k_radius`. The first of these, `k_sphere`, turns the option on to only include k-points within a certain distance, `k_radius` (in Bohr^{-}1), to a certain k-point, `k_center`. The index assigned to `k_center` should correspond to the index of the desired k-point in the IBZ as seen in the prerequisite SCF calculation. Multiple spheres around multiple k-points may be used, and the number of spheres is controlled by `k_nspheres`. In this case, `k_center` and `k_radius` should be input as lists. Importantly, when the sphere option is used, the symmetries of the system are still respected, which is also demonstrated in Fig. 3.5.

The remaining options are related to input and output handling, and are more or less self-explanatory. Additionally, there are a few additional option to control the RIM, as seen in Section 3.2.1.

Finally, if the user wishes to quickly generate an input file or be reminded of how the input file is structured, the command `mxmat.x -e` will generate an input file with comments describing the keywords. This can also be done for `MXCI` and `MXPP`.

A.2 MXCI

The most essential input parameters are provided in `MXMAT`, and therefore most of the input handling in `MXCI` relates to diagonalization options. The input file for `MXCI` is structured in a similar way to `MXMAT`, namely

```
&control
    solver = 'slepc'
    neig   = 100
    diag   = 1,1,1,1 !(DEFAULT: 1,1,1,1) Order is jvc,kvc,jvv,jcc
    .
    offd   = 1,1,1,1 !(DEFAULT: 1,1,1,1) Order is jvc,kvc,jvv,jcc
    .
/
&quasiparticles
    qp_opt  = 'ks'
    scissor = 0.0
/
&scalapack
    nblock  = 24
```

```
    nprow    = 8
    npcol    = 8
/
&io
    job_dir = 'data'
    qp_path = '/path/to/ndb.QP'
/
```

The first flag seen in the `&control` namelist, `solver`, determines the solver used to diagonalize the matrix. As mentioned in Section 3.3.2, there are two possible options: ScaLAPACK for dense matrices (excitons) and SLEPc for sparse matrices (any ED level beyond the exciton). When using the ScaLAPACK interface, the number of returned eigenvalues (and eigenvectors) will simply match the number of configurations, since this is nearly always some manageable number for excitons. Otherwise, for SLEPc, the parameter `neig` will control the number of eigenvalues returned, starting from the lowest one. The parameters `diag` and `offd` dictates which matrix elements should be included in the CI matrix. This can be particularly useful for analyzing how different interactions determine the energetic ordering and splitting of excited states. As an example, this was used to study the negative trion species seen in [E1]. Next, the keyword `qp_opt` will determine the theory level of the quasiparticle energies used in the Hamiltonian. The option chosen in this example `'ks'` indicates that the Kohn-Sham eigenvalues of the prerequisite SCF calculation will be used. Other options are `'sci'` for a scissor shift of the conduction band eigenvalues, and `'qp'` for self-energy corrected GW eigenvalues, which then must be computed in advance via YAMBO. Lastly, if ScaLAPACK is chosen as the eigensolver, the product of `nprow` and `npcol` should give the number of tasks used during parallel execution.

A.3 MXPP

As mentioned, MXPP is a post-processing tool, and features several utilities. To decide which tool in the MXPP suite to use, an input file with the following structure can be used:

```
&pp
    pp_mode = 'mx_rho'
/
&mx_rho
    ncells  = 21,21,1
    r_fix   = 3.043038963176635, 1.756899364540146,
    30.78469137855036
    state   = 3
    d_tol   = 0.0001
    typ_fix = 'h'
    typ_plt = 'e'
    rho_suffix   = 'l2'
/
&io
    job_dir   = 'data'
    overwrite = .true.
/
```

The entry `pp_mode` controls which tool is to be used, which is then followed by a corresponding namelist. In the above example, the mode has been set to `mx_rho`, which is the tool associated with computing the many-body density as described in Section 3.4.2, and in the corresponding namelist further variables must then be set. The full range of possibilities for `pp_mode` include:

- `'conv'` Converts the Fortran binary files into `.hdf5`-files, which are easier accessible via higher-level programming languages like Python.
- `'dry'` Will do the initial reading and writing of `MXMAT` without performing any matrix element calculations and creates a file called `dft_base`. This is useful for confirming the correct choice of bands and k-points.
- `'sex'` Computes the spin-expectation value for all bands and k-points of a given DFT calculation, which is generally convenient for post-processing purposes.
- `'ks_rho'` Calculates the one-electron density for a specified Kohn-Sham state.
- `'spec'` Finds the excited state dipole moment for all states found in the preceeding `MXCI` calculation, and further the excited state absorption spectrum as described in Eq. (3.36).
- `'mx_rho'` Evaluates the many-body density as described in Section 3.4.2, where one particle is fixed, one is plotted, and the rest are averaged out. This is typically a computationally intensive calculation, and thus can also be executed in parallel.
- `'wght'` Projects the configurational weight of a specified state(s) onto the single-particle Kohn-Sham states. This can be particularly useful when analyzing the configurational structure of a state.

The individual namelists needed for each instance of `pp_mode` should be more or less self-explanatory, and will not be described in detail in this work.

B

Supplementary Information of Relevant Publications

This chapter provides the Supplementary Information for Ref. [E1] and [E2], respectively. In both cases, a condensed description of theory or methodology associated with the CI procedure is included, which can be skipped by the reader without loss of coherence, since this was covered in detail in Chapters 2 and 3.

Contents

B.1 Supplementary Information Relevant to [E1]

The supplementary information presented within the following documents the underlying calculations that serve as the fundament for the main manuscript [E1]. This includes convergence tests for both k-point sampling, number of bands included, and the radius of the sphere used to limit the number of k-points employed. Furthermore, states not described within the main manuscript are analyzed, and comparisons are made between results computed with unscreened and screened electron-hole exchange coupling for all highlighted states. Lastly, a brief discussion of the energetic relation between the **K**- and **Q**-valley under strain is presented.

Supplementary Information

Beyond the K-Valley: Exploring Unique Trion States in Indirect Band Gap Monolayer WSe_2

Carl Emil Mørch Nielsen,[1] Franz Fischer,[1,2] and Gabriel Bester[1]

[1] *Institute of Physical Chemistry, University of Hamburg, 22607 Hamburg, Germany*
[2] *Max Planck Institute for the Structure and Dynamics of Matter, 22761 Hamburg, Germany*

(Dated: December 22, 2024)

THE MANY-BODY HAMILTONIAN

For a system of N interacting electrons moving in an external potential, V_{ext}, (such as those of atoms, molecules or crystals) the many-body Hamiltonian is (in atomic units)

$$\mathcal{H} = \sum_i \left(-\frac{1}{2}\nabla_i^2 + V_{\text{ext}}(\mathbf{r}_i) \right) + \frac{1}{2}\sum_{i\neq j} \frac{1}{|\mathbf{r}_i - \mathbf{r}_j|}. \quad (1)$$

A mean field potential, $V(\mathbf{r})$, can be introduced such that the single-particle states, $|i\rangle$, satisfy

$$\left(-\frac{1}{2}\nabla_i^2 + V_{\text{ext}}(\mathbf{r}_i) + V(\mathbf{r}_i) \right) |i\rangle = h_i |i\rangle = \epsilon_i |i\rangle , \quad (2)$$

where h_i denote the single-particle Hamiltonian and ϵ_i the corresponding energy. This allows Eq. (1) to be rewritten as

$$\mathcal{H} = \sum_i h_i + \frac{1}{2}\sum_{i\neq j} v(\mathbf{r}_i, \mathbf{r}_j) - \sum_i V(\mathbf{r}_i), \quad (3)$$

where $v(\mathbf{r}_i, \mathbf{r}_j) = 1/|\mathbf{r}_i - \mathbf{r}_j|$. The second-quantized form of Eq. (3) is

$$\begin{aligned}\mathcal{H} = &\sum_i \epsilon_i c_i^\dagger c_i + \frac{1}{2}\sum_{ijkl} \langle ij|\, v\, |kl\rangle\, c_i^\dagger c_j^\dagger c_l c_k \\ &- \sum_{ij} \langle i|\, V\, |j\rangle\, c_i^\dagger c_j,\end{aligned} \quad (4)$$

where $c_i^\dagger$ and c_i are the fermionic creation and annihilation operators, respectively. They satisfy

$$[c_i, c_j^\dagger]_+ = \delta_{ij}, \quad c_i |\Omega\rangle = 0, \quad c_i^\dagger |\Omega\rangle = |i\rangle ,$$

where $[\,]_+$ denotes the anti/fermionic-commutator, while $|\Omega\rangle$ denotes the vacuum state. Moreover, we employ the notation that

$$\langle ij|\, v\, |kl\rangle = \int \psi_i^*(1)\psi_j^*(2) v(1,2) \psi_k(1)\psi_l(2)\, \mathrm{d}1\mathrm{d}2, \quad (5)$$

where $1 = (\mathbf{r}_1, \sigma)$ combines position and spin, while $\int \mathrm{d}1 = \sum_{\sigma=\uparrow,\downarrow} \int \mathrm{d}\mathbf{r}_1$ includes spin summation.

Electron-hole Picture

In the single-particle picture, i.e. neglecting the last two terms of Eq. (4), the ground state will have the lowest N electronic states occupied. Assuming this is a non-degenerate state allows for defining the Fermi level and a corresponding state index n_f. All states below n_f are occupied (hole states) and all above are empty (electron states). Electron states are denoted with Latin indices, and the electron operators are

$$a_i = c_i, \quad a_i^\dagger = c_i^\dagger. \quad (6)$$

Analogously, hole states are denoted with Greek letters. The corresponding hole operators are

$$b_\alpha = c_\alpha^\dagger, \quad b_\alpha^\dagger = c_\alpha. \quad (7)$$

In this picture, the vacuum state is defined as the ground state of the non-interacting picture i.e. the many-body state where states above n_f are empty and occupied below (empty with respect to holes). This implies that

$$a_i |\Omega\rangle = 0, \quad b_\alpha |\Omega\rangle = 0, \quad \alpha \leq n_f < i. \quad (8)$$

The usual fermionic commutation relations hold for both the electron and hole operators in their own subspace, that is

$$[a_i, a_j^\dagger]_+ = \delta_{ij}, \quad [b_\alpha, b_\beta^\dagger]_+ = \delta_{\alpha\beta}. \quad (9)$$

However, the electron and hole operators commute with one another. Formally

$$[a_i, b_\alpha]_+ = [a_i, b_\alpha^\dagger]_+ = [a_i^\dagger, b_\alpha]_+ = [a_i^\dagger, b_\alpha^\dagger]_+ = 0, \quad (10)$$

since the subspaces of α and i are disjoint.

Derivation

The electron-hole picture allows for rewriting Eq. (4) by splitting each sum in two ($> n_f$ and $< n_f$). However, given the abundance of terms involved, we opt to summarize. Assuming that V is the Hartree-Fock potential, i.e. $\langle i|\, V\, |j\rangle = \sum_\alpha \langle i\alpha|\, v\, |j\alpha\rangle - \langle i\alpha|\, v\, |\alpha j\rangle$, the many-body Hamiltonian can be rewritten as

$$\mathcal{H} = E_c + \mathcal{H}_0 + \mathcal{H}_{eh} + \mathcal{H}_{ee} + \mathcal{H}_{hh} + \mathcal{H}_{xx} + \mathcal{H}_{ex} + \mathcal{H}_{hx}, \quad (11)$$

where

$$
\begin{aligned}
E_c &= \sum_{\alpha} \epsilon_\alpha + \frac{1}{2}\sum_{\alpha\gamma} \left[\langle \alpha\gamma | \, v \, | \gamma\alpha \rangle - \langle \alpha\gamma | \, v \, | \alpha\gamma \rangle \right], \\
\mathcal{H}_0 &= \sum_{i} \epsilon_i a_i^\dagger a_i - \sum_{\alpha} \epsilon_\alpha b_\alpha^\dagger b_\alpha, \\
\mathcal{H}_{eh} &= \sum_{ij\alpha\beta} \left[\langle i\alpha | \, v \, | \beta j \rangle - \langle i\alpha | \, v \, | j\beta \rangle \right] a_i^\dagger b_\beta^\dagger b_\alpha a_j, \\
\mathcal{H}_{ee} &= \frac{1}{2}\sum_{ijkl} \langle ij | \, v \, | kl \rangle \, a_i^\dagger a_j^\dagger a_l a_k, \\
\mathcal{H}_{hh} &= \frac{1}{2}\sum_{\alpha\beta\gamma\lambda} \langle \alpha\beta | \, v \, | \gamma\lambda \rangle \, b_\lambda^\dagger b_\gamma^\dagger b_\alpha b_\beta, \\
\mathcal{H}_{xx} &= \frac{1}{2}\sum_{ij\alpha\beta} \Big\{ \langle ij | \, v \, | \alpha\beta \rangle \, a_i^\dagger b_\beta^\dagger b_\alpha^\dagger a_j^\dagger + \text{h.c.} \Big\}, \\
\mathcal{H}_{ex} &= \frac{1}{2}\sum_{ijk\alpha} \Big\{ \langle ij | \, v \, | k\alpha \rangle_{\text{as}} \, a_j^\dagger b_\alpha^\dagger a_i^\dagger a_k + \text{h.c.} \Big\}, \\
\mathcal{H}_{hx} &= \frac{1}{2}\sum_{\alpha\beta\gamma i} \Big\{ \langle \alpha\beta | \, v \, | \gamma i \rangle_{\text{as}} \, b_\gamma^\dagger b_\beta b_\alpha a_i + \text{h.c.} \Big\},
\end{aligned}
$$

and $\langle ij | \, v \, | k\alpha \rangle_{\text{as}} = \langle ij | \, v \, | k\alpha \rangle - \langle ij | \, v \, | \alpha k \rangle$ in the $\mathcal{H}_{ex}$ term (analogous for $\mathcal{H}_{hx}$). The term, E_c, involves no operators, and thus contributes only a constant to the eigenvalues. The interests here are excitation energies, so E_c is disregarded henceforth.

In the configuration interaction (CI) formalism, Eq. (11) essentially represents the full many-body Hamiltonian (full CI). This encompasses all conceivable configurations of electrons and holes within the system and the coupling between these. Excitons are defined as the eigenstates of $\mathcal{H}$ in the subspace of singly excited determinants, i.e. including only configurations of the form $|i\alpha\rangle = a_i^\dagger b_\alpha^\dagger |\Omega\rangle$. Similarly, trions emerge when diagonalizing in the subspace of charged singly excited determinants, and so forth. Hence, for excitons, trions, biexctions etc., we truncate the configurational space to a specific excitation level. Consequently, in these truncated schemes, there is no coupling between configurational subspaces, allowing us to further disregard $\mathcal{H}_{xx}$, $\mathcal{H}_{ex}$, and $\mathcal{H}_{hx}$, as they do not conserve the number of particles.

Furthermore, the matrix elements of the effective GW/Bethe-Salpeter equation (GW/BSE) Hamiltonian [1] in the Tamm-Dancoff approximation take the form

$$
\begin{aligned}
\langle i\alpha | \, \mathcal{H}_{\text{BSE}} \, | j\beta \rangle =& (\epsilon_i^{\text{qp}} - \epsilon_\alpha^{\text{qp}})\delta_{ij}\delta_{\alpha\beta} \\
&+ \langle i\beta | \, v \, | \alpha j \rangle - \langle i\beta | \, W \, | j\alpha \rangle \,,
\end{aligned} \tag{12}
$$

where ϵ_n^{qp} are the quasiparticle energies found by a GW calculation, and $W(\mathbf{r}_1, \mathbf{r}_2)$ is the screened Coulomb interaction defined as $W(\mathbf{r}_1, \mathbf{r}_2) = \int \epsilon^{-1}(\mathbf{r}_1, \mathbf{r}_3) v(\mathbf{r}_3, \mathbf{r}_2) \mathrm{d}\mathbf{r}_3$, where $\epsilon^{-1}(\mathbf{r}_1, \mathbf{r}_3)$ is the inverse dielectric screening. Correspondingly, the matrix elements of $\mathcal{H}$ in Eq. (11) in the basis of singly excited determinants, namely excitons, are as follows

$$
\begin{aligned}
\langle i\alpha | \, \mathcal{H} \, | j\beta \rangle =& (\epsilon_i - \epsilon_\alpha)\delta_{ij}\delta_{\alpha\beta} \\
&+ \langle i\beta | \, v \, | \alpha j \rangle - \langle i\beta | \, v \, | j\alpha \rangle \,.
\end{aligned} \tag{13}
$$

The discrepancy between Eq. (12) and Eq. (13) lies only in the quasiparticle energies and the screened interaction. Building upon the argumentation of, and in accordance with, Deilmann *et al.* [2] and Torche *et al.* [3, 4], we modify the many-body Hamiltonian of Eq. (11) to

$$
\mathcal{H} = \mathcal{H}_0 + \mathcal{H}_{eh} + \mathcal{H}_{ee} + \mathcal{H}_{hh}, \tag{14}
$$

where

$$
\begin{aligned}
\mathcal{H}_0 &= \sum_{i} \epsilon_i^{\text{qp}} a_i^\dagger a_i - \sum_{\alpha} \epsilon_\alpha^{\text{qp}} b_\alpha^\dagger b_\alpha, \\
\mathcal{H}_{eh} &= \sum_{ij\alpha\beta} \left[\langle i\alpha | \, v \, | \beta j \rangle - \langle i\alpha | \, W \, | j\beta \rangle \right] a_i^\dagger b_\beta^\dagger b_\alpha a_j, \\
\mathcal{H}_{ee} &= \frac{1}{2}\sum_{ijkl} \langle ij | \, W \, | kl \rangle \, a_i^\dagger a_j^\dagger a_l a_k, \\
\mathcal{H}_{hh} &= \frac{1}{2}\sum_{\alpha\beta\gamma\lambda} \langle \alpha\beta | \, W \, | \gamma\lambda \rangle \, b_\lambda^\dagger b_\gamma^\dagger b_\alpha b_\beta.
\end{aligned}
$$

The first term, $\mathcal{H}_0$, incorporates the non-interacting part of $\mathcal{H}$, describing the independent motion of each particle. $\mathcal{H}_{ee}$ and $\mathcal{H}_{hh}$ represent the usual Coulomb interaction between fermions. As for $\mathcal{H}_{eh}$, it accounts for the interaction between electrons and holes, consisting of both an attractive direct term (screened) and a repulsive exchange term (bare).

Absorption

The formula for absorption, denoted by α, is derived directly from Fermi's golden rule.. It describes the excitation from an initial (many-body) state, $|\mathrm{X}^{m-1}\rangle$, to all possible final many-body states, $|\mathrm{X}^m_\lambda\rangle$, differing by exactly one electron-hole pair, while maintaining the same total/center-of-mass momentum, $\mathbf{Q}_{\text{COM}}$, through the absorption of a photon. The many-body states are linear combinations of determinants, e.g. $|\mathrm{X}_\lambda\rangle = \sum_{i\alpha} A^\lambda_{i\alpha} a_i^\dagger b_\alpha^\dagger |\Omega\rangle$ for excitons. Formally,

$$
\alpha(\omega) = \sum_{\lambda} |\, \langle \mathrm{X}^{m-1} | \hat{\mathcal{E}} \cdot \mathbf{r} | \mathrm{X}^m_\lambda \rangle \,|^2 \delta(E^m_\lambda - E^{m-1} - \hbar\omega), \tag{15}
$$

where $\hat{\mathcal{E}}$ represents the direction of the perturbing field, E denotes the final/initial state energies, and $\hbar\omega$ is the photon energy. The dipole operator $\mathbf{r}$ is of the form

$$
\mathbf{r} = \sum_{i\alpha} \langle \alpha | \mathbf{r} | i \rangle \, b_\alpha a_i, \tag{16}
$$

which further emphasizes why the initial and final states must differ by exactly one electron-hole pair. Furthermore, due to momentum conservation $\langle \alpha | \mathbf{r} | i \rangle = 0$ if $\mathbf{k}_i \neq \mathbf{k}_\alpha$.

Excitons

As mentioned in the previous section, excitons are the eigenstates of $\mathcal{H}$ in the subspace of singly excited determinants. The configurations of this subspace are of the form $|i\alpha\rangle = a_i^\dagger b_\alpha^\dagger |\Omega\rangle$. In the context of periodic systems, each state is indexed by a band and a $\mathbf{k}$-point i.e. $|i\rangle = |i, \mathbf{k}_i\rangle$. Additionally, we require that the configurations conserve momentum, each having $\mathbf{Q}_{\mathrm{COM}} = \mathbf{k}_i - \mathbf{k}_\alpha$. In this work, all exciton results are calculated with $\mathbf{Q}_{\mathrm{COM}} = 0$. The exciton wavefunctions are of the form

$$|\mathrm{X}_\lambda\rangle = \sum_{i\alpha} A_{i\alpha}^\lambda a_i^\dagger b_\alpha^\dagger |\Omega\rangle\,, \tag{17}$$

where $A_{i\alpha}^\lambda$ are the exciton eigenstates found by diagonalization of Eq. (12). With regards to absorption, the initial state is taken to be $|\Omega\rangle$, and the associated dipole moment is

$$\langle\Omega|\,\mathbf{r}\,|\mathrm{X}_\lambda\rangle = \sum_{i\alpha} A_{i\alpha}^\lambda \langle\alpha|\mathbf{r}|i\rangle\,. \tag{18}$$

Trions

There are two types of trions; negatively- and positively charged, denoted X^- and X^+, respectively. In the case of vanishing doping and low temperature, the additional carriers localize in the energetically lowest state, which is the conduction band minimum (CBM) for electrons and the valence band maximum (VBM) for holes.

Negatively charged trions exist in the basis of configurations of the form $|ij\alpha\rangle = a_i^\dagger a_j^\dagger b_\alpha^\dagger |\Omega\rangle$ with the condition that $i < j$. Furthermore, to conserve momentum of the dopant, we restrict the configurations by requiring that $\mathbf{Q}_{\mathrm{COM}} = \mathbf{k}_i + \mathbf{k}_j - \mathbf{k}_\alpha$ is either $\pm\mathbf{K}$ or $\mathbf{Q}$. Regardless, the matrix elements to be computed for X^- are

$$\begin{aligned}\langle ij\alpha|\,\mathcal{H}\,|kl\beta\rangle = (\epsilon_i^{\mathrm{qp}} + \epsilon_j^{\mathrm{qp}} - \epsilon_\alpha^{\mathrm{qp}})\delta_{ik}\delta_{jl}\delta_{\alpha\beta}\\ + [\langle i\beta|v|\alpha k\rangle - \langle i\beta|W|k\alpha\rangle\,]\delta_{jl}\\ - [\langle i\beta|v|\alpha l\rangle - \langle i\beta|W|l\alpha\rangle\,]\delta_{jk}\\ - [\langle j\beta|v|\alpha k\rangle - \langle j\beta|W|k\alpha\rangle]\delta_{il}\\ + [\langle j\beta|v|\alpha l\rangle - \langle j\beta|W|l\alpha\rangle\,]\delta_{ik}\\ + [\langle ij|W|kl\rangle - \langle ij|W|lk\rangle\,]\delta_{\alpha\beta},\end{aligned} \tag{19}$$

and the associated wavefunctions are of the form

$$|\mathrm{X}_\lambda^-\rangle = \sum_{ij\alpha} A_{ij\alpha}^\lambda a_i^\dagger a_j^\dagger b_\alpha^\dagger |\Omega\rangle\,. \tag{20}$$

When computing absorption for X^-, the initial state, $|c\rangle$, is an electron in the conduction band. The X^- dipole moments are found as

$$\langle c|\,\mathbf{r}\,|\mathrm{X}_\lambda^-\rangle = \sum_{ij\alpha} A_{ij\alpha}^\lambda \big(\mathbf{r}_{\alpha j}\delta_{ci} - \mathbf{r}_{\alpha i}\delta_{cj}\big), \tag{21}$$

where $|c\rangle$ is positioned either at $\mathbf{K}$ or $\mathbf{Q}$ within the lowest conduction band to match the chosen $\mathbf{Q}_{\mathrm{COM}}$. From Eq. (21), it is evident that $|\mathrm{X}_\lambda^-\rangle$ only becomes bright if (some of) the constituting configurations meet three conditions: (i) one of the electrons is in state $|c\rangle$, (ii) the electron-hole pair can recombine in a bright manner (spin- and momentum conserving), and (iii) the associated $A_{ij\alpha}^\lambda$ is relatively large.

For positively charged trions, X^+, the basis is constituted by configurations of the form $|i\alpha\beta\rangle = a_i^\dagger b_\alpha^\dagger b_\beta^\dagger |\Omega\rangle$ with the condition that $\alpha < \beta$ and $\mathbf{Q}_{\mathrm{COM}} = \mathbf{k}_i - \mathbf{k}_\alpha - \mathbf{k}_\beta = -\mathbf{K}$. Analogously to X^+, the matrix elements are computed as

$$\begin{aligned}\langle i\alpha\beta|\,\mathcal{H}\,|j\gamma\lambda\rangle = (\epsilon_i^{\mathrm{qp}} - \epsilon_\alpha^{\mathrm{qp}} - \epsilon_\beta^{\mathrm{qp}})\delta_{ij}\delta_{\alpha\gamma}\delta_{\beta\lambda}\\ + [\langle i\gamma|v|\alpha j\rangle - \langle i\gamma|W|j\alpha\rangle\,]\delta_{\beta\lambda}\\ - [\langle i\lambda|v|\alpha j\rangle - \langle i\lambda|W|j\alpha\rangle\,]\delta_{\beta\gamma}\\ - [\langle i\gamma|v|\beta j\rangle - \langle i\gamma|W|j\beta\rangle\,]\delta_{\alpha\lambda}\\ + [\langle i\lambda|v|\beta j\rangle - \langle i\lambda|W|j\beta\rangle\,]\delta_{\alpha\gamma}\\ + [\langle\gamma\lambda|W|\alpha\beta\rangle - \langle\gamma\lambda|W|\beta\alpha\rangle]\delta_{ij},\end{aligned} \tag{22}$$

where the X^+ wavefunctions are

$$|\mathrm{X}_\lambda^+\rangle = \sum_{i\alpha\beta} A_{i\alpha\beta}^\lambda a_i^\dagger b_\alpha^\dagger b_\beta^\dagger |\Omega\rangle\,. \tag{23}$$

The initial state for absorption, $|\nu\rangle$, is a hole placed at $-\mathbf{K}$ in the uppermost valence band. This leads to dipole moments of the form

$$\langle\nu|\,\mathbf{r}\,|\mathrm{X}_\lambda^+\rangle = \sum_{i\alpha\beta} A_{i\alpha\beta}^\lambda \big(\mathbf{r}_{\alpha i}\delta_{\nu\beta} - \mathbf{r}_{\beta i}\delta_{\nu\alpha}\big). \tag{24}$$

Analogously to X^-, $|\mathrm{X}_\lambda^+\rangle$ only becomes bright if (some of) the constituting configurations meet three conditions: (i) one of the holes is in state $|\nu\rangle$, (ii) the electron-hole pair can recombine in a bright manner (spin- and momentum conserving), and (iii) the associated $A_{i\alpha\beta}^\lambda$ is reasonably large.

Two-body Matrix Elements

Clearly, Eqs. (12), (19) and (22) dictate the computation of numerous two-body matrix elements. The starting point for these are the single-particle Bloch wavefunctions,

$$|i\rangle = u_i(\mathbf{r}, \sigma)e^{i\mathbf{k}_i\mathbf{r}}.$$

where $u_i(\mathbf{r}, \sigma)$ is a spinor, that can be written in terms of its Fourier transform

$$u_i(\mathbf{r}, \sigma) = \frac{1}{\sqrt{\Omega}} \sum_{\mathbf{G}} u_i(\mathbf{G}, \sigma)e^{i\mathbf{G}\mathbf{r}}.$$

Specifically, we obtain $u_i(\mathbf{G},\sigma)$ from a DFT calculation [5, 6]. Furthermore, the bare Coulomb interaction can be written in terms of its Fourier transform as

$$v(\mathbf{r},\mathbf{r}') = \frac{1}{\Omega}\sum_{\mathbf{q},\mathbf{G}} v_{\mathbf{G}}(\mathbf{q}) e^{i(\mathbf{q}+\mathbf{G})(\mathbf{r}-\mathbf{r}')},$$

where we truncate the coulomb potential to 2D, $v_{\mathbf{G}}(\mathbf{q}) = v^{\mathrm{2D}}_{\mathbf{G}}(\mathbf{q})$, as

$$v^{\mathrm{2D}}_{\mathbf{G}}(\mathbf{q}) = \frac{4\pi}{|\mathbf{q}+\mathbf{G}|^2} \times \left[1 - e^{-|\mathbf{q}_\parallel+\mathbf{G}_\parallel|L_z/2}\cos([q_z+G_z]L_z/2)\right],$$

with L_z being the out-of-plane cell length [7]. Utilizing the notation from Eq. (5) results in bare two-body matrix elements of the following form:

$$\begin{aligned}\langle ij|\, v\,|kl\rangle =& \frac{1}{\Omega}\sum_{\mathbf{q},\mathbf{G}} v_{\mathbf{G}}(\mathbf{q}) \\ &\times \frac{1}{\Omega}\int u_i^*(1)u_k(1)e^{i\mathbf{G}\mathbf{r}_1}\,\mathrm{d}1\,\delta_{\mathbf{q},\mathbf{k}_{ik}} \\ &\times \frac{1}{\Omega}\int u_j^*(2)u_l(2)e^{-i\mathbf{G}\mathbf{r}_2}\,\mathrm{d}2\,\delta_{\mathbf{q},\mathbf{k}_{lj}},\end{aligned} \tag{25}$$

where $\mathbf{k}_{ik} = \mathbf{k}_i - \mathbf{k}_k$. The above expression imposes the condition that $\mathbf{k}_{ik} = \mathbf{k}_{lj}$, which is consistently fulfilled as all configurations possess equal $\mathbf{Q}_{\mathrm{COM}}$. Moreover, if we let

$$\rho_{ik}(\mathbf{r}) = \sum_{\sigma=\uparrow,\downarrow} u_i^*(\mathbf{r},\sigma)u_k(\mathbf{r},\sigma),$$

it becomes evident that the integrals in Eq. (25) are simply the Fourier transforms of $\rho_{ik}(\mathbf{r})$ and $\rho^*_{lj}(\mathbf{r})$, respectively, that is

$$\rho_{ik}(\mathbf{G}) = \frac{1}{\Omega}\int u_i^*(1)u_k(1)e^{i\mathbf{G}\mathbf{r}_1}\,d1.$$

As such, bare Coulomb matrix elements can be computed as

$$\langle ij|\, v\,|kl\rangle = \frac{1}{\Omega}\sum_{\mathbf{G}\neq 0}\rho^*_{lj}(\mathbf{G})v_{\mathbf{G}}(\mathbf{k}_{ik})\rho_{ik}(\mathbf{G}), \tag{26}$$

which is simply an element-wise vector product followed by an inner product. Furthermore, it should be mentioned that we have excluded the $\mathbf{G}=0$ term to ensure consistency between our many-body Hamiltonian and the BSE when projected into the exciton subspace [1, 8].

The screened Coulomb interaction can likewise be expressed in terms of its Fourier transform,

$$W(\mathbf{r},\mathbf{r}') = \frac{1}{\Omega}\sum_{\mathbf{q},\mathbf{G},\mathbf{G}'} W_{\mathbf{G}\mathbf{G}'}(\mathbf{q})e^{i(\mathbf{q}+\mathbf{G})\mathbf{r}}e^{-i(\mathbf{q}+\mathbf{G}')\mathbf{r}'},$$

where

$$W_{\mathbf{G}\mathbf{G}'}(\mathbf{q}) = \epsilon^{-1}_{\mathbf{G}\mathbf{G}'}(\mathbf{q},\omega=0)\sqrt{v_{\mathbf{G}}(\mathbf{q})}\sqrt{v_{\mathbf{G}'}(\mathbf{q})}.$$

In the above expression, $\epsilon^{-1}_{\mathbf{G}\mathbf{G}'}(\mathbf{q},\omega=0)$ is the static part of the inverse microscopic dielectric function. Moreover, to enhance numerical stability for small values of $\mathbf{q}+\mathbf{G}$, we employ a random integration method (RIM) when computing $v_{\mathbf{G}}(\mathbf{q})$, similar to that of Ref. [9]. Analogously to Eq. (26), we find

$$\langle ij|\, W\,|kl\rangle = \frac{1}{\Omega}\sum_{\mathbf{G},\mathbf{G}'}\rho^*_{lj}(\mathbf{G}')W_{\mathbf{G}\mathbf{G}'}(\mathbf{k}_{ik})\rho_{ik}(\mathbf{G}) \tag{27}$$

which can be computed as a matrix-vector product followed by an inner product.

COMPUTATIONAL DETAILS

Excited state calculations are typically divided into two steps: computing matrix elements and solving the Hamiltonian. For excitons, fewer elements need evaluation owing to the much smaller configurational space ($\sim 10^4$) compared to that of trions ($> 10^6$). Consequently, all exciton calculations in this work are computed using 2×2 ($n_v\times n_c$) bands, and include all $\mathbf{k}$-points in the first Brillouin zone (BZ). The resulting matrix is dense and should be evaluated using a dense solver [10]. In contrast, the configurational space of trions is massive, but many configurations do not couple (when more than two spin-orbitals differ). This results in extremely sparse matrices (>99% sparsity), which require a sparse solver [11]. To reduce the computational load of trion calculations, we use only 1×2 bands and exclude $\mathbf{k}$-points not relevant to the configurations of the low-energy trions. Supplementary Figure 1 shows the included $\mathbf{k}$-points for trion calculations where $\mathbf{Q}_{\mathrm{COM}} = \pm\mathbf{K}$ ($\mathrm{X}^-_{\mathbf{K}}$ and X^+). The reduced number of bands and $\mathbf{k}$-points lowers the computational resources needed for X^+- and $\mathrm{X}^-_{\mathbf{K}}$-trions nearly to that of excitons. Similarly, $\mathrm{X}^-_{\mathbf{Q}}$-trions are computed on a reduced $\mathbf{k}$-mesh, as depicted in Supplementary Figure 2. $\mathbf{Q}$ is defined as the $\mathbf{k}$-point that houses the conduction band minimum (CBM). Due to the star domain of symmetries for $\mathbf{Q}$, which includes six symmetries in addition to the $\mathbf{K}$ and $\mathbf{K}$' areas, the number of included $\mathbf{k}$-points is about four times larger compared to X^+- and $\mathrm{X}^-_{\mathbf{K}}$-trions. Consequently, the computation of matrix elements is vastly more expensive, while the corresponding Hamiltonian is significantly larger. Additionally, for $\mathbf{k}$-meshes, $n_k\times n_k$, where n_k is even, the CBM, which is usually at $\mathbf{Q}$, appears slightly off-center from the Γ-K-path. Therefore, only $\mathbf{k}$-meshes, where n_k is odd, can realistically be used. Additionally, $\mathbf{Q}$ is not located exactly at $\mathbf{K}/2$, but is slightly offset towards $\mathbf{K}$. Consequently, $\mathbf{Q}$ varies slightly between different $\mathbf{k}$-meshes.

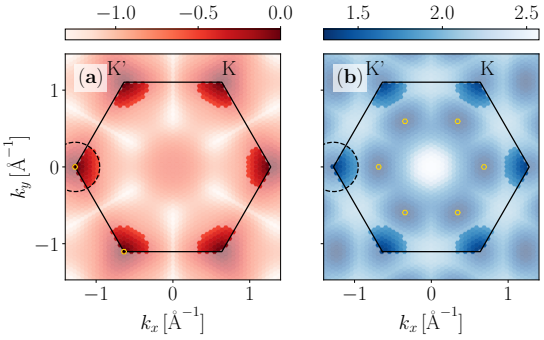

Supplementary Figure 1. Brillouin zone sampling around K. (a) The uppermost valence band of monolayer WSe_2 in reciprocal space in eV highlighting k-points included for a sphere of radius 0.17 Bohr^{-1} centered around **K**. The first Brillouin zone is illustrated in black, and the hollow, golden marker indicates the VBM (K). (b) Analogous plot for the lowermost conduction band, with the CBM (**Q**) highlighted.

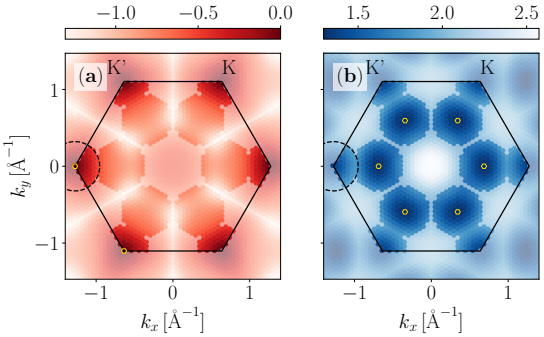

Supplementary Figure 2. Brillouin zone sampling around K and Q. (a,b) Similar to Supplementary Figure 1, but using two spheres, both of radius 0.17 Bohr^{-1}, centered around **K** and **Q**, respectively.

Convergence

To ensure accuracy and reliability of our results, we have performed extensive convergence tests on our calculations. Note, that for all calculations, we shift the spectrum such that the A exciton will land at 1.73 eV. In Supplementary Figure 3, the convergence of excitons with respect to the **k**-mesh can be seen. The D and B excitons converge rapidly with the **k**-mesh, while the A_{2s} state converges more slowly. We find an additional satellite state below A_{2s}, denoted A_{sat}, which closely resembles the A exciton - both in reciprocal and real space. We depict these three states in **??**. Interestingly, the satellite state seems to converge to the same value as A_{2s} when extrapolated to infinitely dense k-sampling. Supplementary

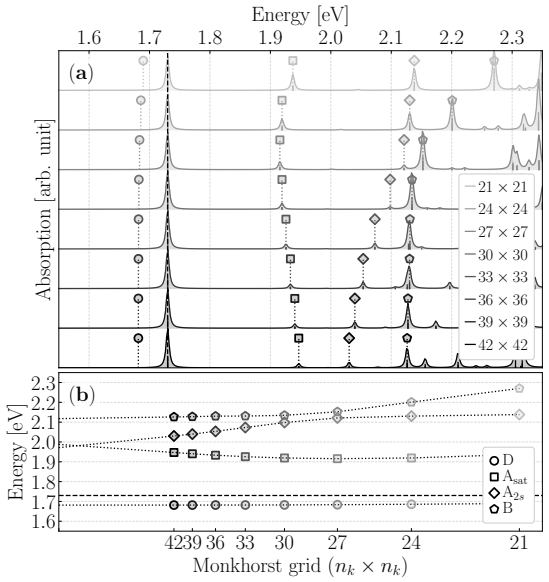

Supplementary Figure 3. Exciton absorption spectrum k-point convergence (a) Absorption spectra for different **k**-meshes, with the lowest (dark) state and the most prominent bright states indicated by a marker. (b) The energetic position of these states extrapolated to an infinitely dense grid. In both plots, the A exciton is indicated by a dashed black line.

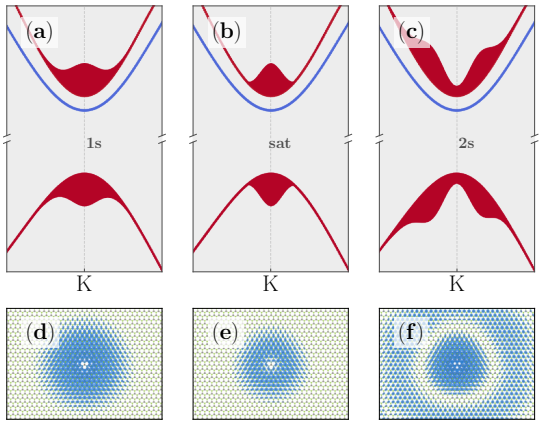

Supplementary Figure 4. Configurations of specific excitonic states (a,b,c) The configurational weights of A, A_{sat}, and A_2a, respectively. (c,d,f) The wavefunction in real space of the electron with the hole fixed in the center for the same three states, respectively. The isosurface value has been set to 0.2×10^{-7}.

Figure 5 shows the convergence of the states of interest for different convergence criteria extrapolated to the ideal

scenario. In the case of trions, the spectra are shifted by the value that makes the A exciton of an exciton calculation on the same **k**-mesh align at 1.73 eV. In all cases of **k**-grid convergence (Supplementary Figure 5(d,f,h)), the low energy states of interest converge rapidly and display the correct ordering even when $n_k = 21$. However, further convergence is, as demonstrated, needed to obtain correct splittings and energetic positions. Moreover, as illustrated in Supplementary Figure 5(b), the choice of 1×2 bands is valid for the low-energy states, since these are mainly constituted by configurations composed of A and/or D exciton-like states with an additional carrier. As mentioned, we employ a reduced **k**-mesh, for ease of computation of trions, by excluding **k**-points that fall outside a certain radius of the expected location of the carries (**K** and **Q**). As such, these radii need to be converged as well. We emphasize from Supplementary Figure 5(a) that even for excitons (localized around $\pm\mathbf{K}$), the entire BZ is not required for accurate results. Based on Supplementary Figure 5(c,e), we consider both X^+- and $X^-_{\mathbf{K}}$-trions converged for a radius of $0.2\,\mathrm{Bohr}^{-1}$, seeing as larger radii change the states of interest by only $\sim$1 meV. For $X^-_{\mathbf{Q}}$-trions, we include additional **k**-points around **K**, since the electron-hole pair mainly localizes there. In Supplementary Figure 5(h), the spheres around **K** are fixed to radii of $0.17\,\mathrm{Bohr}^{-1}$, while the spheres around **Q** vary in radius. We see slower convergence with radius of $X^-_{\mathbf{Q}}$-trions compared to that of $X^-_{\mathbf{K}}$-trions, likely due to the slightly larger effective mass in the **Q**-valley. We regard a radius of $0.17\,\mathrm{Bohr}^{-1}$ around **Q** converged, seeing as larger radii changes the energetic position by only ~ 1 meV. In summary, we emphasize the importance of especially **k**-point convergence for the low energy trion states of interest and the fact that extrapolation is required for reliable results within the presented method.

Screening of Electron-Hole Exchange Coupling

Whether the electron-hole exchange coupling, denoted as K^{eh}, should be screened is in itself a topic of debate. We explored both scenarios on a 42×42 Monkhorst grid, summarized in Table 1. Consistent with Torche *et al.* [3], we found discrepancies to be are relatively small. However, as shown in the main paper, the binding energies obtained using the unscreened K^{eh} align more closely with experimental measurements.

Effect of strain on the lowest conduction band

We note that the energetic difference in the lowest conduction band between the **K** and **Q** valley is highly sensitive to strain. To estimate the effects of strain we have varied both the in-plane lattice constant a, as well as the Se-Se distance d within the interval of $[-1, 1]\,\%$, respectively. The results are displayed in Supplementary Figure 6. We observe that for compressive strain, i.e. a smaller in-plane lattice constant and a larger Se-Se distance, the **Q**-valley shifts energetically even further below the **K**-valley. Qualitatively speaking, this would lead to an enhanced red-shift of the $X^-_{\mathbf{Q}}$ compared to $X^-_{\mathbf{K}}$. Contrastingly, employing tensile in-plane strain and corresponding smaller Se-Se distances, the **K**-**Q**-splitting is reversed, resulting in a direct band gap at **K**. Here, it may be assumed that at some level of strain $X^-_{\mathbf{K}}$ would be lower in energy than $X^-_{\mathbf{Q}}$. All would need to be confirmed by a deeper investigation on energetic ordering, splittings and brightness of the trions which is outside the scope of the current paper. We can foresee that strain would be an interesting tuning knob to influence the trionic spectral features. Finally, we note that there was a recent publication on the effects of strain on positive trions in WSe_2 [12].

Supplementary Table 1. Comparison of binding energies for excitons and trions with and without screening of K^{eh}. The binding energies are relative to A, except for $D^{\pm}_i$, which is relative to D. The binding energy of A is relative to the band gap at **K**. All values in units of meV.

	D^+	D^-	D	$A^-_{\mathbf{K},\mathrm{S}}$	$A^-_{\mathbf{K},\mathrm{T}}$	A^+	D
$\langle ij\vert\, v\,\vert kl\rangle$	22	22	43	45	40	31	559
$\langle ij\vert\, W\,\vert kl\rangle$	12	12	49	41	35	29	554

[1] G. Onida, L. Reining, and A. Rubio, Electronic excitations: density-functional versus many-body green's-function approaches, Rev. Mod. Phys. **74**, 601 (2002).

[2] T. Deilmann, M. Drüppel, and M. Rohlfing, Three-particle correlation from a many-body perspective: Trions in a carbon nanotube, Phys. Rev. Lett. **116**, 196804 (2016).

[3] A. Torche and G. Bester, First-principles many-body theory for charged and neutral excitations: Trion fine structure splitting in transition metal dichalcogenides, Phys. Rev. B **100**, 201403 (2019).

[4] A. Torche and G. Bester, Biexcitons fine structure and non-equilibrium effects in transition metal dichalcogenides monolayers from first principles, Communications Physics **4**, 67 (2021).

[5] P. Giannozzi *et al.*, Quantum espresso: a modular and open-source software project for quantum simulations of materials, Journal of Physics: Condensed Matter **21**, 395502 (19pp) (2009).

[6] P. Giannozzi *et al.*, Advanced capabilities for materials modelling with quantum espresso, Journal of Physics: Condensed Matter **29**, 465901 (2017).

[7] C. A. Rozzi, D. Varsano, A. Marini, E. K. U. Gross, and A. Rubio, Exact coulomb cutoff technique for supercell calculations, Phys. Rev. B **73**, 205119 (2006).

[8] G. Strinati, Application of the green's functions method to the study of the optical properties of semiconductors,

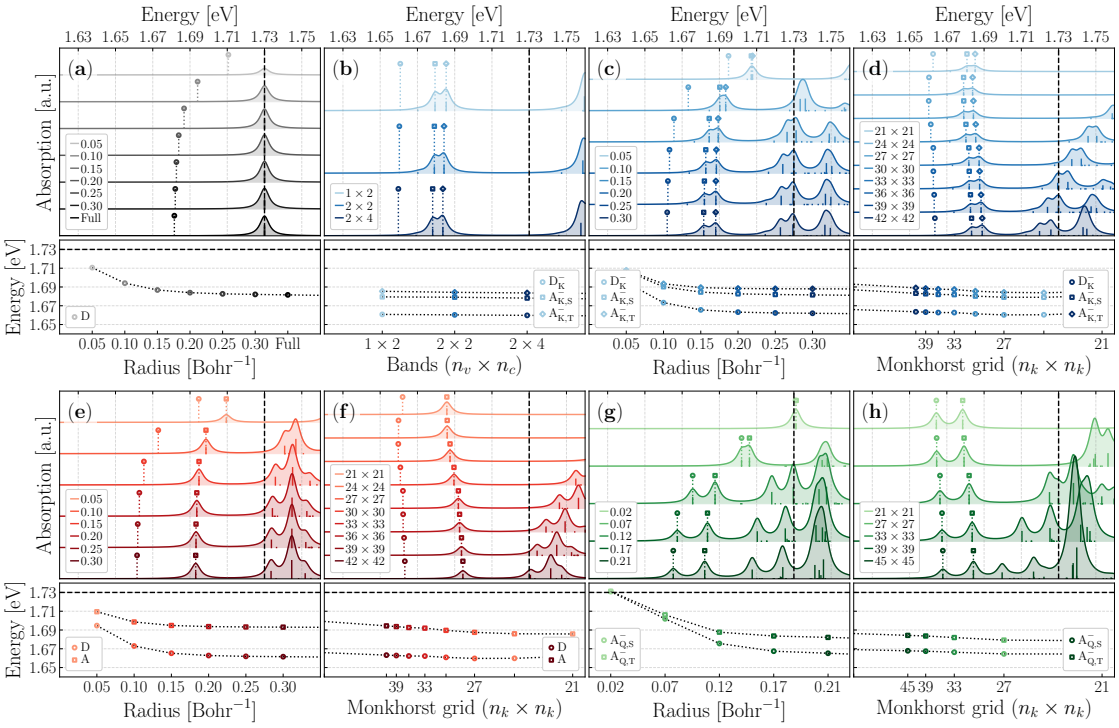

Supplementary Figure 5. **Convergence of excited many-body states** (a,c,e) Convergence with respect to radius of sphere centered around **K** for X (grey), $X^-_{\mathbf{K}}$ (blue) and X^+ (red), respectively. (g) Convergence with respect to radius of sphere centered around **Q** for $X^-_{\mathbf{Q}}$ (green), with the additional sphere at **K** fixed to a radius of 0.17 Bohr^{-1}. For all convergence tests with respect to radius a **k**-grid of 39×39 has been used. (b) Convergence of $X^-_{\mathbf{K}}$ (blue) with respect to number of bands included. (d,f) Convergence with respect to **k**-grid for $X^-_{\mathbf{K}}$ (blue) and X^+ (red), respectively, using a sphere of radius 0.2 Bohr^{-1}. (h) Convergence with respect to **k**-grid for $X^-_{\mathbf{Q}}$ (green) using spheres of radii 0.17 Bohr^{-1}.

La Rivista del Nuovo Cimento **11**, 1–86 (1988).

[9] A. Marini, C. Hogan, M. Grüning, and D. Varsano, yambo: An ab initio tool for excited state calculations, Computer Physics Communications **180**, 1392–1403 (2009).

[10] L. S. Blackford *et al.*, *ScaLAPACK Users' Guide* (Society for Industrial and Applied Mathematics, Philadelphia, PA, 1997).

[11] V. Hernandez, J. E. Roman, and V. Vidal, SLEPc: A scalable and flexible toolkit for the solution of eigenvalue problems, ACM Trans. Math. Software **31**, 351 (2005).

[12] A. M. Kumar *et al.*, Strain fingerprinting of exciton valley character in 2D semiconductors, Nat Commun **15**, 7546 (2024).

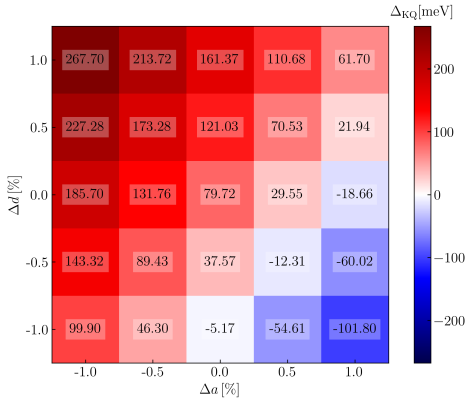

Supplementary Figure 6. Strain dependence of the K-Q energy difference in the lowest conduction band. The in-plane lattice constant a and the Se-Se-distance d has been varied within the interval of $[-1, 1]$ %. The color denotes the sign of the energetic K-Q-ordering. Red (blue) color denotes $\epsilon_c^{\mathrm{K}} > \epsilon_c^{\mathrm{Q}}$ ($\epsilon_c^{\mathrm{K}} < \epsilon_c^{\mathrm{Q}}$). The K-Q-splitting is displayed on each tile.

B.2 Supplementary Information Relevant to [E2]

The following pages are the supplementary information for Ref. [E2]. Here, results computed for the Janus structured WSSe-WSSe are presented for both exciton and trions, which are akin to those of MoSSe-WSSe, due to the similar atomic composition and structure. Beyond that, a more detailed description of the second exciton state, D_{II}, is given in order to understand the unexpected brightness it displays. Lastly, convergence tests with respect to the k-point sampling are included, and the data is extrapolated to obtain binding energies for infinitely dense sampling.

Supplementary Material

From Dark to Bright: First-Principles Prediction of Ground State Excitons and Trions in Janus Transition Metal Dichalcogenide Bilayers

Carl Emil Mørch Nielsen,[1] Franz Fischer,[1,2] Marta Prada,[1,3] and Gabriel Bester[1,4]

[1] *Institute of Physical Chemistry, University of Hamburg, Luruper Chaussee 149, 22607 Hamburg, Germany*
[2] *Max Planck Institute for the Structure and Dynamics of Matter, Luruper Chausse 149, 22761 Hamburg, Germany*
[3] *I. Institute for Theoretical Physics, University of Hamburg, 22761 Hamburg, Germany*
[4] *The Hamburg Centre for Ultrafast Imaging, Luruper Chaussee 149, 22761 Hamburg, Germany*

(Dated: August 5, 2025)

COMPUTATIONAL DETAILS

Our many-body calculations are ultimately based on a density functional theory (DFT) calculation computed in the `Quantum Espresso` framework [1, 2]. Kohn-Sham wavefunctions are computed within the generalized gradient approximation (GGA) with PBE parametrization [3], where we employ fully relativistic norm-conserving pseudopotentials [4] and as such include spin-orbit coupling effects. Furthermore, to simulate the effects of interlayer van der Waals coupling during structural relaxation, we utilize an *ab initio* DFT-D3-BJ parameterization [5], while using out-of-plane unit cell dimension of 50 Bohr - ensuring sufficient vacuum for suppressing interaction of periodic images. For Se-S interfaced WSSe-WSSe we achieve a lattice constant of 3.22 Å and an interlayer metal-metal z-distance of 6.29 Å during structural optimization. All DFT calculations are performed with a energy cutoff of 60 Ry. The static inverse dielectric screening function, $\epsilon^{-1}_{\mathbf{G}\mathbf{G}'}(\omega = 0, \mathbf{q})$, used to construct the screened interaction, W, is computed within the random phase approximation (RPA) via `YAMBO` [6, 7]. Here, we find that using 20 times more conduction bands than valence bands combined with an response function energy cut-off of 10 Ry yields converged results.

The theory of our many-body calculations is well described in previous works [8], and will not be explained in detail here. For the calculation of excitons, we included 4 valence bands and 8 conduction bands, which yields converged results. However, for the negatively charged trion states we found that using 1 valence band and 4 conduction bands was sufficient to converge the interlayer states, which were the states of interest. Similarly, the positively charged trion states converged after using 3 valence bands and 2 conduction bands. Moreover, for the computation of trions we only include k-points that lie within a distance of 0.2 Bohr^{-1} to $\mathbf{K}$ and $\mathbf{K}'$ [8], which is also a parameter that must be converged. Lastly, in order to achieve well-converged results for any level of excitation, we extrapolate the energetic levels during k-grid convergence to an infinitely dense grid, which can be seen in Supplementary Figures **5** to **10**.

REAL-SPACE WAVEFUNCTION COMPUTATIONS

The wavefunction for exciton state λ is of the form

$$|X_\lambda\rangle = \sum_{i\alpha} A^\lambda_{i\alpha} \psi_i(\mathbf{r}_{e_1}) \psi^*_\alpha(\mathbf{r}_{h_1}), \tag{1}$$

where $A^\lambda_{i\alpha}$ are the exciton wavefunction coefficient obtained by diagonalizing the many-body Hamiltonian, while $\psi_i(\mathbf{r}_{e_1})$ and $\psi^*_\alpha(\mathbf{r}_{h_1})$ are single-particle electron and hole wavefunctions, respectively. As such, the exciton wavefunction is multicoordinate function depending on both $\mathbf{r}_{e_1}$ and $\mathbf{r}_{h_1}$, which is difficult to plot in any meaningful way. We can however employ a density operator that puts the electron at position $\mathbf{r}_1$ and the hole at position $\mathbf{r}_2$, namely

$$\hat{\rho} = \delta(\mathbf{r}_{e_1} - \mathbf{r}_1)\delta(\mathbf{r}_{h_1} - \mathbf{r}_2). \tag{2}$$

This gives us an exciton density of

$$\rho_e(\mathbf{r}_1, \mathbf{r}_2) = \langle X_\lambda | \hat{\rho} | X_\lambda \rangle = \Big| \sum_{i\alpha} A^\lambda_{i\alpha} \psi_i(\mathbf{r}_1) \psi^*_\alpha(\mathbf{r}_2) \Big|^2. \tag{3}$$

Then, we either fix $\mathbf{r}_2$ and plot $\mathbf{r}_1$ to see the electronic part of the exciton density or vice versa. In practice, and throughout this work, we compute the electronic part of the density by averaging over two cases of the hole position; the metal atom in the lower layer ($\mathbf{r}_{\mathrm{M}_1}$), and the metal atom in the upper layer ($\mathbf{r}_{\mathrm{M}_2}$), which is to say that

$$\rho_e(\mathbf{r}_1) = \frac{1}{2}\Big[\rho_e(\mathbf{r}_1, \mathbf{r}_2 = \mathbf{r}_{\mathrm{M}_1}) + \rho_e(\mathbf{r}_1, \mathbf{r}_2 = \mathbf{r}_{\mathrm{M}_2})\Big], \tag{4}$$

and the same holds true for hole part of the density. Similarly to Eq. (1), but using Slater determinants to respect the anti-symmetric indistinguishably of fermions, the negatively-charged trion wavefunction for state λ is of the form

$$|X^-_\lambda\rangle = \frac{1}{\sqrt{2}} \sum_{ij\alpha} A^\lambda_{ij\alpha} \big\{\psi_i(\mathbf{r}_{e_1})\psi_j(\mathbf{r}_{e_2}) - \psi_j(\mathbf{r}_{e_1})\psi_i(\mathbf{r}_{e_2})\big\}\psi^*_\alpha(\mathbf{r}_{h_1}) \tag{5}$$

$$= \frac{1}{\sqrt{2}} \sum_{ij\alpha} \big\{A^\lambda_{ij\alpha} - A^\lambda_{ji\alpha}\big\}\psi_i(\mathbf{r}_{e_1})\psi_j(\mathbf{r}_{e_2})\psi^*_\alpha(\mathbf{r}_{h_1}). \tag{6}$$

In Eq. (5), the summation is restricted to $i < j$, which is not the case for Eq. (6). Here, the coefficients are instead restricted, meaning that electron index 2 (e_2) must be larger than electron index 1 (e_1), independently for holes and electrons. We again employ a density operator that puts one of the electrons at position $\mathbf{r}_1$ and the hole at position $\mathbf{r}_2$ and. It is of the form

$$\hat{\rho} = \delta(\mathbf{r}_{e_1} - \mathbf{r}_1)\delta(\mathbf{r}_{h_1} - \mathbf{r}_2), \tag{7}$$

which gives us the electronic part of the trion density with respect to the hole, as

$$\rho_e(\mathbf{r}_1) = \langle X^-_\lambda | \, \hat{\rho} \, |X^-_\lambda\rangle = \sum_j \Big| \sum_{i\alpha} \big\{A^\lambda_{ij\alpha} - A^\lambda_{ji\alpha}\big\}\psi_i(\mathbf{r}_1)\psi^*_\alpha(\mathbf{r}_2)\Big|^2. \tag{8}$$

Again, we average over the two cases of the hole position for an unbiased guess at which layer the particles distribute in.

WSSE RESULTS

Here, we show results for Se-S interfaced bilayer WSSe-WSSe, analogous to the main paper. The band structure can be seen in Supplementary Figure 1, which looks similar to that of MoSSe-WSSe, albeit with the valence band maximum at **K**. Exciton results are shown in Supplementary Figure 2. We note, that the state D_{IL} is completely dark here, which was not the case for MoSSe-WSSe. Furthermore, we show the trion results in Supplementary Figure 3, and note that also here, the spin-forbidden states are truly dark. A description of the unexpected bright character of D_{IL} in MoSSe-WSSe can, however, be found in Supplementary Figure 4, in which it can be seen how the electronic part of D_{IL} distributes between the two layers due to the hybridized nature of of the lower most conduction bands when going from K to Q (halfway between K and Γ).

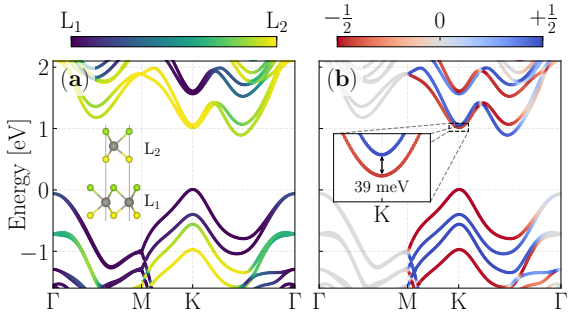

Supplementary Figure 1. (a) Layer-projected band structure of Se-S interfaced WSSe-WSSe, where purple denotes the lower layer (L_1) and yellow the upper oner (L_2), and (b) $\langle \hat{s}_z \rangle$-projected band structure where red denotes spin-up and blue spin-down. The inset shows the SOC induced conduction band splitting of 39 meV.

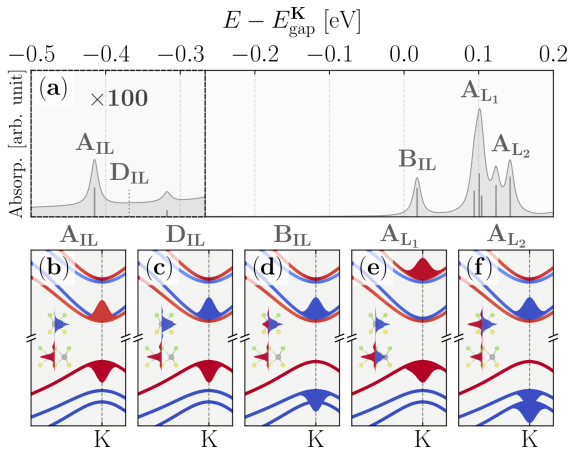

Supplementary Figure 2. (a) Exciton absorption spectrum of bilayer WSSe-WSSe relative to the interlayer bandgap at **K**. To increase the visibility of interlayer states the first portion of the spectrum is magnified by a factor of 100. Prominent states are highlighted by name. (b,c,d,e,f) The configurational weight of the excitonic states of interest displayed on the bands near **K** with color matching the spin-character of the constituting bands. The inset shows the real-space excitonic density along z for the hole (red) and the electron (blue).

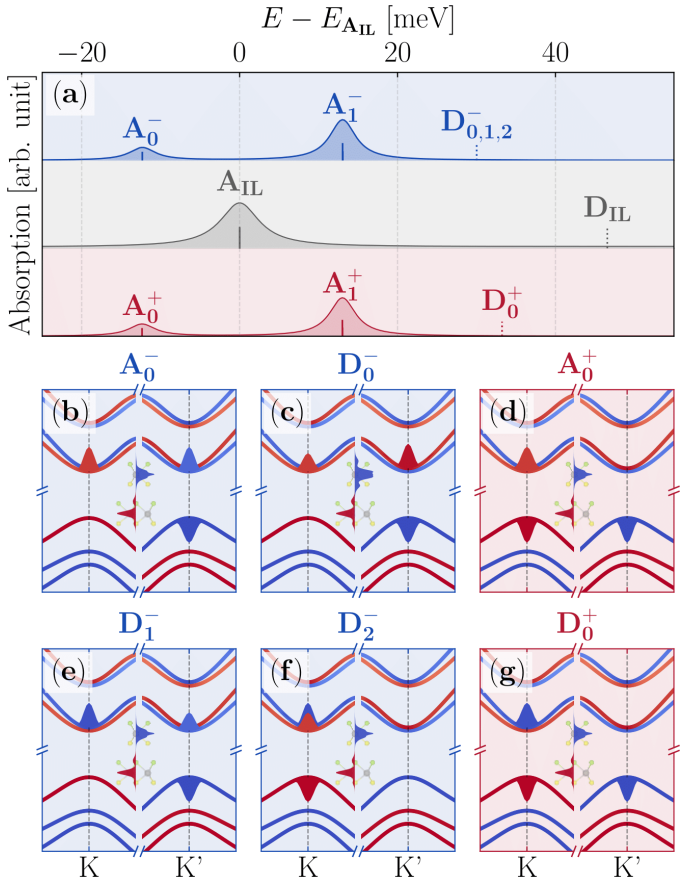

Supplementary Figure 3. (a) Trion and exciton absorption spectra of bilayer WSSe-WSSe relative to A_{IL}. Negatively charged trions in upper, blue panel, excitons in middle, grey panel and positvely charged trions in lower, red panel. (b,c,d,e,f,g) The configurational weight of the states of interest displayed on the bands near **K** and **K′** with color matching the spin-character of the constituting bands. The inset shows the real-space density along z for hole (red) and electron (blue).

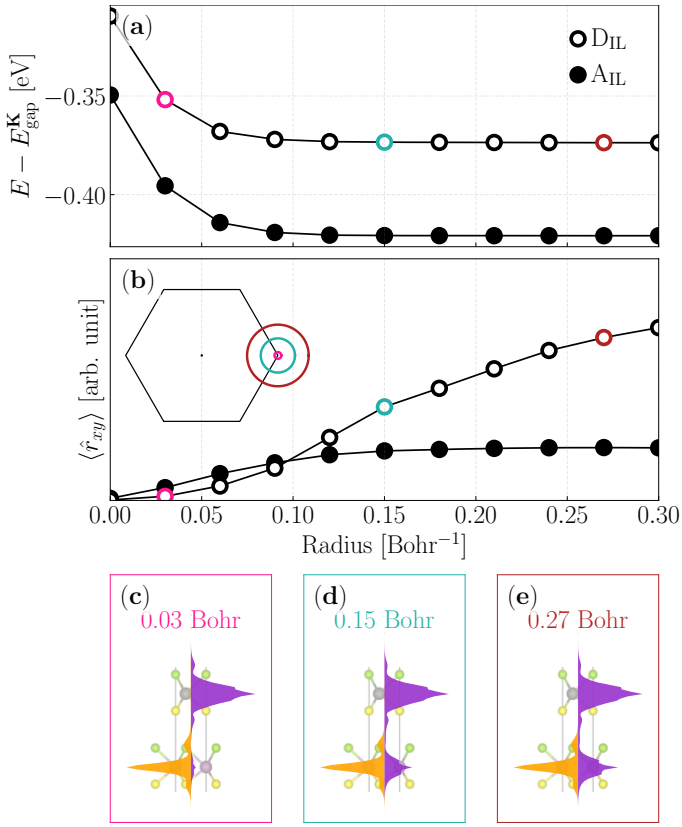

Supplementary Figure 4. In this figure, we employ only k-points within a certain radius of the K and K' points as described in previous works [8]. (a) The exciton energy of A_{IL} and D_{IL} with respect to the radius. (b) The in-plane dipole moment (brightness) with respect to the radius of the aforementioned states. The inset visualized three selected highlighted with colored markers in the plot. (c-e) The exciton wavefunction of D_{IL} for three distinct radii (0.03, 0.15 and 0.27 Bohr^{-1}), depicting how the state only hybridizes between the two layers (and as such becomes bright), when including single-particle states that are further from the K/K'-point.

EXCITON CONVERGENCE

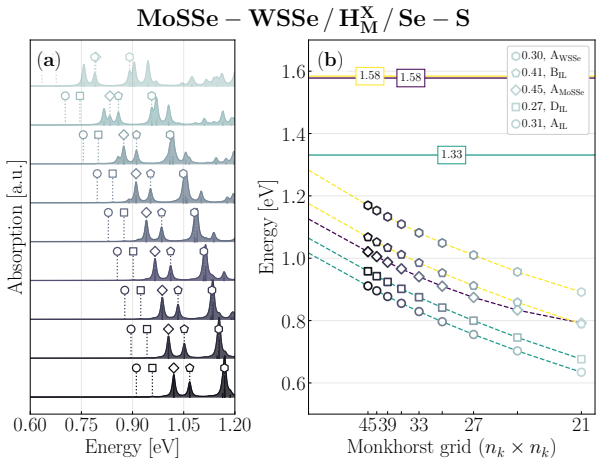

Supplementary Figure 5. (a) Exciton convergence with respect to k-grid of MoSSe-WSSe, where states of interest are marked (see legend in (b)). (b) Extrapolated exciton energies. Bandgap at **K** is marked by a solid line for interlayer transition (cyan), lower MoSSe layer (purple) and upper WSSe layer (yellow). Binding energies are given with respect to the transition matching the color of the dashed line.

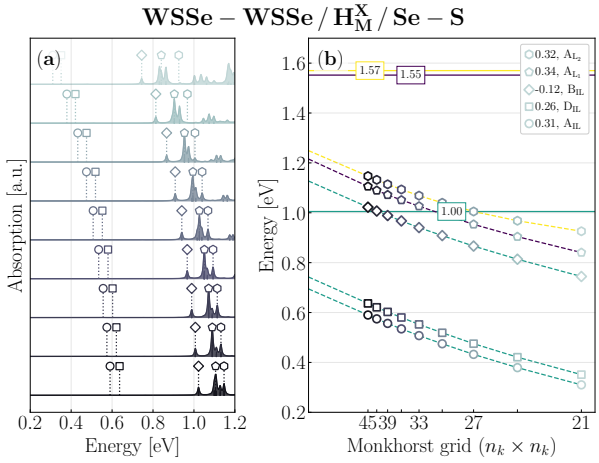

Supplementary Figure 6. (a) Exciton convergence with respect to k-grid of WSSe-WSSe, where states of interest are marked (see legend in (b)). (b) Extrapolated exciton energies. Bandgap at **K** is marked by a solid line for interlayer transition (cyan), lower WSSe layer (purple) and upper WSSe layer (yellow). Binding energies are given with respect to the transition matching the color of the dashed line.

NEGATIVELY CHARGED TRION CONVERGENCE

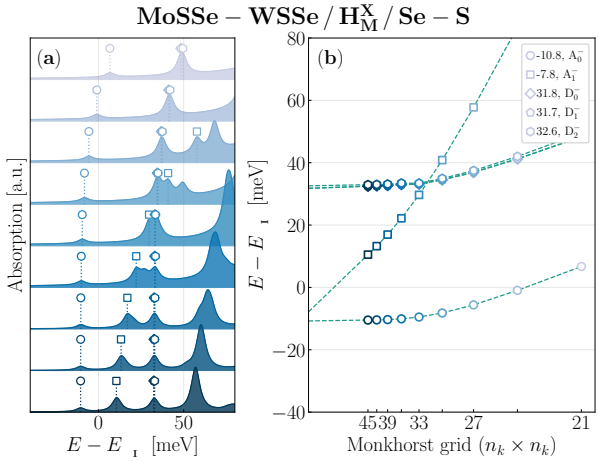

Supplementary Figure 7. (a) Negative trion convergence with respect to k-grid of MoSSe-WSSe, where states of interest are marked (see legend in (b)). (b) Extrapolated trion energies. All trion binding energies are given with respect to A_{IL}.

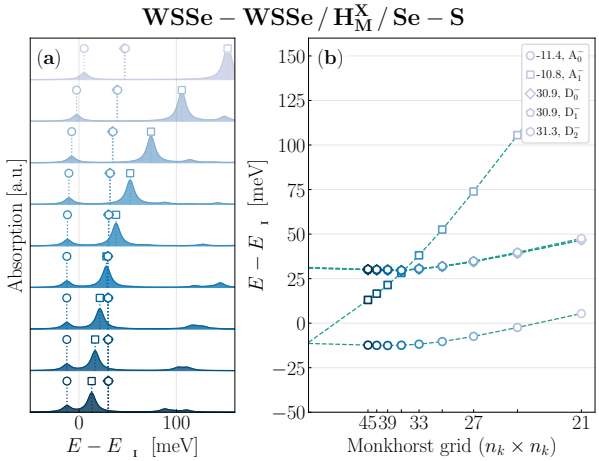

Supplementary Figure 8. (a) Negative trion convergence with respect to k-grid of WSSe-WSSe, where states of interest are marked (see legend in (b)). (b) Extrapolated trion energies. All trion binding energies are given with respect to A_{IL}.

POSITIVELY CHARGED TRION CONVERGENCE

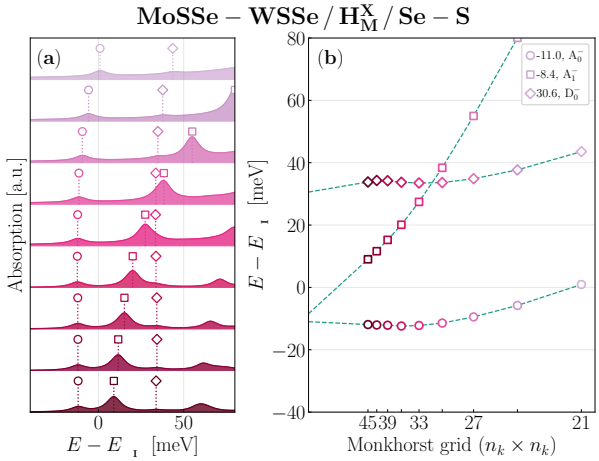

Supplementary Figure 9. (a) Positive trion convergence with respect to k-grid of MoSSe-WSSe, where states of interest are marked (see legend in (b)). (b) Extrapolated trion energies. All trion binding energies are given with respect to A_{IL}.

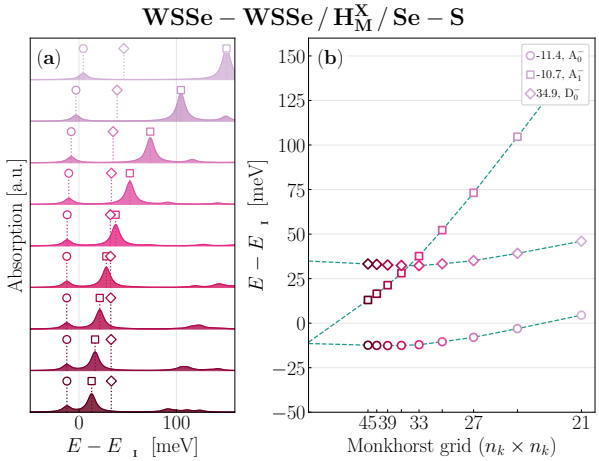

Supplementary Figure 10. (a) Positive trion convergence with respect to k-grid of WSSe-WSSe, where states of interest are marked (see legend in (b)). (b) Extrapolated trion energies. All trion binding energies are given with respect to A_{IL}.

[1] P. Giannozzi *et al.*, QUANTUM ESPRESSO: a modular and open-source software project for quantum simulations of materials, J. Phys.: Condens. Matter **21**, 395502 (2009).
[2] P. Giannozzi *et al.*, Advanced capabilities for materials modelling with QUANTUM ESPRESSO, J. Phys.: Condens. Matter **29**, 465901 (2017).
[3] J. P. Perdew, K. Burke, and M. Ernzerhof, Generalized Gradient Approximation Made Simple, Phys. Rev. Lett. **77**, 3865–3868 (1996).
[4] M. van Setten *et al.*, The PseudoDojo: Training and grading a 85 element optimized norm-conserving pseudopotential table, Comput. Phys. Comm. **226**, 39–54 (2018).
[5] S. Grimme, J. Antony, S. Ehrlich, and H. Krieg, A consistent and accurate *ab initio* parametrization of density functional dispersion correction (DFT-D) for the 94 elements H-Pu, J. Chem. Phys. **132**, 154104 (2010).
[6] A. Marini, C. Hogan, M. Grüning, and D. Varsano, yambo: An *ab initio* tool for excited state calculations, Comput. Phys. Comm. **180**, 1392–1403 (2009).
[7] D. Sangalli *et al.*, Many-body perturbation theory calculations using the yambo code, J. Phys.: Condens. Matter **31**, 325902 (2019).
[8] C. E. Mørch Nielsen, F. Fischer, and G. Bester, Beyond the K-valley: exploring unique trion states in indirect band gap monolayer WSe_2, npj 2D Mater Appl **9**, 11 (2025).

References

[1] **K. S. Novoselov et al.** Electric Field Effect in Atomically Thin Carbon Films. *Science* **306**, 666–669 (2004).

[2] **K. F. Mak, C. Lee, J. Hone, J. Shan, and T. F. Heinz** Atomically Thin MoS_2: A New Direct-Gap Semiconductor. *Phys. Rev. Lett.* **105**, 136805 (2010).

[3] **T. Li and G. Galli** Electronic Properties of MoS_2 Nanoparticles. *J. Phys. Chem. C* **111**, 16192–16196 (2007).

[4] **S. Lebègue and O. Eriksson** Electronic structure of two-dimensional crystals from ab initio theory. *Phys. Rev. B* **79**, 115409 (2009).

[5] **D. Jiang et al.** Flexible electronics based on 2D transition metal dichalcogenides. *J. Mater. Chem. A* **10**, 89–121 (2022).

[6] **J. Shang et al.** Observation of Excitonic Fine Structure in a 2D Transition-Metal Dichalcogenide Semiconductor. *ACS Nano* **9**, 647–655 (2015).

[7] **G. Wang et al.** Colloquium: Excitons in atomically thin transition metal dichalcogenides. *Rev. Mod. Phys.* **90**, 021001 (2018).

[8] **J. R. Schaibley et al.** Valleytronics in 2D materials. *Nat Rev Mater* **1**, 16055 (2016).

[9] **S. A. Vitale et al.** Valleytronics: Opportunities, Challenges, and Paths Forward. *Small* **14**, 1801483 (2018).

[10] **K. F. Mak, D. Xiao, and J. Shan** Light–valley interactions in 2D semiconductors. *Nature Photon* **12**, 451–460 (2018).

[11] **V. Podzorov, M. E. Gershenson, C. Kloc, R. Zeis, and E. Bucher** High-mobility field-effect transistors based on transition metal dichalcogenides. *Appl. Phys. Lett.* **84**, 3301–3303 (2004).

[12] **S. Das, A. Prakash, R. Salazar, and J. Appenzeller** Toward Low-Power Electronics: Tunneling Phenomena in Transition Metal Dichalcogenides. *ACS Nano* **8**, 1681–1689 (2014).

[13] **J. Y. Lim et al.** Van der Waals junction field effect transistors with both n- and p-channel transition metal dichalcogenides. *npj 2D Mater Appl* **2**, 37 (2018).

[14] **W. Mortelmans et al.** Gate Oxide Module Development for Scaled GAA 2D FETs Enabling SS<75mV/d and Record Idmax>900μA/μm at Lg<50nm, *2024 IEEE International Electron Devices Meeting (IEDM)* 1–4 (2024).

[15] **J. Ping, Z. Fan, M. Sindoro, Y. Ying, and H. Zhang** Recent Advances in Sensing Applications of Two-Dimensional Transition Metal Dichalcogenide Nanosheets and Their Composites. *Adv. Funct. Mater.* **27**, 1605817 (2017).

[16] **E. Lee, Y. S. Yoon, and D.-J. Kim** Two-Dimensional Transition Metal Dichalcogenides and Metal Oxide Hybrids for Gas Sensing. *ACS Sens.* **3**, 2045–2060 (2018).

[17] **A. Mirzaei, J.-Y. Kim, H. W. Kim, and S. S. Kim** Resistive Gas Sensors Based on 2D TMDs and MXenes. *Accounts of Chemical Research* **57**, 2395–2413 (2024).

[18] **E. Bergmann, G. Melet, C. Müller, and A. Simon-Vermot** Friction properties of sputtered dichalcogenide layers. *Tribol. Int.* **14**, 329–332 (1981).

[19] **T. Polcar and A. Cavaleiro** Review on self-lubricant transition metal dichalcogenide nanocomposite coatings alloyed with carbon. *Surf. Coat. Technol.* **206**, 686–695 (2011).

[20] **F. H. L. Koppens et al.** Photodetectors based on graphene, other two-dimensional materials and hybrid systems. *Nature Nanotech* **9**, 780–793 (2014).

[21] **D.-H. Kang et al.** An Ultrahigh-Performance Photodetector based on a Perovskite-Transition-Metal-Dichalcogenide Hybrid Structure. *Adv. Mater.* **28**, 7799–7806 (2016).

[22] **D.-S. Liu, J. Wu, H. Xu, and Z. Wang** Emerging Light-Emitting Materials for Photonic Integration. *Adv. Mater.* **33**, 2003733 (2021).

[23] **O. Ávalos-Ovando, D. Mastrogiuseppe, and S. E. Ulloa** Lateral heterostructures and one-dimensional interfaces in 2D transition metal dichalcogenides. *J. Phys.: Condens. Matter* **31**, 213001 (2019).

[24] **D. Beret et al.** Exciton spectroscopy and unidirectional transport in $MoSe_2$-WSe_2 lateral heterostructures encapsulated in hexagonal boron nitride. *npj 2D Mater Appl* **6**, 84 (2022).

[25] **R. Rosati et al.** Interface engineering of charge-transfer excitons in 2D lateral heterostructures. *Nat Commun* **14**, 2438 (2023).

[26] **B. Kundu et al.** Electrically Controlled Excitons, Charge Transfer Induced Trions, and Narrowband Emitters in $MoSe_2$–WSe_2 Lateral Heterostructure. *Nano Lett.* **24**, 14615–14624 (2024).

[27] **M. Liu et al.** 2D TMD-Based Lateral Heterostructures: Preparation, Property, and Application. *Adv. Funct. Mater.* **n/a**, 2500876 (2025).

[28] **D. Deng et al.** Catalysis with two-dimensional materials and their heterostructures. *Nature Nanotech* **11**, 218–230 (2016).

[29] **R. Wu et al.** Synthesis, Modulation, and Application of Two-Dimensional TMD Heterostructures. *Chem. Rev.* **124**, 10112–10191 (2024).

[30] **Y. Chen et al.** Tunable Band Gap Photoluminescence from Atomically Thin Transition-Metal Dichalcogenide Alloys. *ACS Nano* **7**, 4610–4616 (2013).

[31] **T. Chu, H. Ilatikhameneh, G. Klimeck, R. Rahman, and Z. Chen** Electrically Tunable Bandgaps in Bilayer MoS_2. *Nano Lett.* **15**, 8000–8007 (2015).

[32] **H. Bhunia and A. J. Pal** Band-edges and band-gap in few-layered transition metal dichalcogenides. *J. Phys. D: Appl. Phys.* **51**, 215102 (2018).

[33] **M. Palummo, M. Bernardi, and J. C. Grossman** Exciton Radiative Lifetimes in Two-Dimensional Transition Metal Dichalcogenides. *Nano Lett.* **15**, 2794–2800 (2015).

[34] **J. Choi et al.** Twist Angle-Dependent Interlayer Exciton Lifetimes in van der Waals Heterostructures. *Phys. Rev. Lett.* **126**, 047401 (2021).

[35] **R. Wu et al.** Bilayer tungsten diselenide transistors with on-state currents exceeding 1.5 milliamperes per micrometre. *Nat Electron* **5**, 497–504 (2022).

[36] **H. Guo, X. Zhang, and G. Lu** Shedding light on moiré excitons: A first-principles perspective. *Sci. Adv.* **6**, eabc5638 (2020).

[37] **Z. Zhang et al.** Flat bands in twisted bilayer transition metal dichalcogenides. *Nature Phys* **16**, 1093–1096 (2020).

[38] **E. Li et al.** Lattice reconstruction induced multiple ultra-flat bands in twisted bilayer WSe_2. *Nat Commun* **12**, 5601 (2021).

[39] **F. Wu, T. Lovorn, E. Tutuc, and A. H. MacDonald** Hubbard Model Physics in Transition Metal Dichalcogenide Moiré Bands. *Phys. Rev. Lett.* **121**, 026402 (2018).

[40] **M. M. Scherer, D. M. Kennes, and L. Classen** Chiral superconductivity with enhanced quantized Hall responses in moiré transition metal dichalcogenides. *npj Quantum Mater.* **7**, 100 (2022).

[41] **Y. Xia et al.** Superconductivity in twisted bilayer WSe_2. *Nature* **637**, 833–838 (2025).

[42] **S. Bertolazzi, J. Brivio, and A. Kis** Stretching and Breaking of Ultrathin MoS_2. *ACS Nano* **5**, 9703–9709 (2011).

[43] **C. Zhang et al.** Probing Critical Point Energies of Transition Metal Dichalcogenides: Surprising Indirect Gap of Single Layer WSe_2. *Nano Lett.* **15**, 6494–6500 (2015).

[44] **H. Liu et al.** Observation of intervalley quantum interference in epitaxial monolayer tungsten diselenide. *Nat Commun* **6**, 8180 (2015).

[45] **A. Franceschetti, H. Fu, L. W. Wang, and A. Zunger** Many-body pseudopotential theory of excitons in InP and CdSe quantum dots. *Phys. Rev. B* **60**, 1819–1829 (1999).

[46] **G. Bester** Electronic excitations in nanostructures: an empirical pseudopotential based approach. *J. Phys.: Condens. Matter* **21**, 023202 (2008).

[47] **A. Torche and G. Bester** First-principles many-body theory for charged and neutral excitations: Trion fine structure splitting in transition metal dichalcogenides. *Phys. Rev. B* **100**, 201403 (2019).

[E1] **C. E. Mørch Nielsen, F. Fischer, and G. Bester** Beyond the K-valley: exploring unique trion states in indirect band gap monolayer WSe_2. *npj 2D Mater Appl* **9**, 11 (2025).

[E2] **C. E. Mørch Nielsen, F. Fischer, M. Prada, and G. Bester** From dark to bright: first-principles prediction of ground state excitons and trions in Janus transition metal dichalcogenide bilayers. *2D Mater* **12**, 045015 (2025).

[E3] **C. E. M. Nielsen, M. da Cruz, A. Torche, and G. Bester** Accurate force-field methodology capturing atomic reconstructions in transition metal dichalcogenide moiré system. *Phys. Rev. B* **108**, 045402 (2023).

[48] **F. H. Stillinger and T. A. Weber** Computer simulation of local order in condensed phases of silicon. *Phys. Rev. B* **31**, 5262–5271 (1985).

[49] **A. N. Kolmogorov and V. H. Crespi** Smoothest Bearings: Interlayer Sliding in Multiwalled Carbon Nanotubes. *Phys. Rev. Lett.* **85**, 4727–4730 (2000).

[50] **A. N. Kolmogorov and V. H. Crespi** Registry-dependent interlayer potential for graphitic systems. *Phys. Rev. B* **71**, 235415 (2005).

[51] **J.-W. Jiang and Y.-P. Zhou** Handbook of Stillinger-Weber Potential Parameters for Two-Dimensional Atomic Crystals. *IntechOpen* (2017).

[52] **M. Born and R. Oppenheimer** Zur Quantentheorie der Molekeln. *Ann. Phys.* **389**, 457–484 (1927).

[53] **P. Hohenberg and W. Kohn** Inhomogeneous Electron Gas. *Phys. Rev.* **136**, B864–B871 (1964).

[54] **J. P. Dahl** Introduction to the Quantum World of Atoms and Molecules. *World Scientific* (2001).

[55] **W. Kohn and L. J. Sham** Self-Consistent Equations Including Exchange and Correlation Effects. *Phys. Rev.* **140**, A1133–A1138 (1965).

[56] **D. R. Hartree** The Wave Mechanics of an Atom with a Non-Coulomb Central Field. Part II. Some Results and Discussion. *Math. Proc. Camb. Philos. Soc.* **24**, 111–132 (1928).

[57] **V. Fock** Näherungsmethode zur Lösung des quantenmechanischen Mehrkörperproblems. *Zeitschrift für Physik* **61**, 126–148 (1930).

[58] **D. R. Hartree and W. Hartree** Self-consistent field, with exchange, for beryllium. *Proc. R. Soc. Lond. A* **150**, 9–33 (1935).

[59] **J. P. Perdew et al.** Atoms, molecules, solids, and surfaces: Applications of the generalized gradient approximation for exchange and correlation. *Phys. Rev. B* **46**, 6671–6687 (1992).

[60] **J. P. Perdew, K. Burke, and M. Ernzerhof** Generalized Gradient Approximation Made Simple. *Phys. Rev. Lett.* **77**, 3865–3868 (1996).

[61] **P. L. Altick and A. E. Glassgold** Correlation Effects in Atomic Structure Using the Random-Phase Approximation. *Phys. Rev.* **133**, A632–A646 (1964).

[62] **P. R. Surján** Second Quantized Approach to Quantum Chemistry: An Elementary Introduction. 1st ed. *Springer Berlin, Heidelberg* (1989).

[63] **J. C. Slater** The Theory of Complex Spectra. *Phys. Rev.* **34**, 1293–1322 (1929).

[64] **E. U. Condon** The Theory of Complex Spectra. *Phys. Rev.* **36**, 1121–1133 (1930).

[65] **A. Szabo and N. S. Ostlund** Modern quantum chemistry: introduction to advanced electronic structure theory. *Courier Corporation* (1996).

[66] **G. Onida, L. Reining, and A. Rubio** Electronic excitations: density-functional versus many-body Green's-function approaches. *Rev. Mod. Phys.* **74**, 601–659 (2002).

[67] **L. Hedin** New Method for Calculating the One-Particle Green's Function with Application to the Electron-Gas Problem. *Phys. Rev.* **139**, A796–A823 (1965).

[68] **P. Giannozzi et al.** QUANTUM ESPRESSO: a modular and open-source software project for quantum simulations of materials. *J. Phys.: Condens. Matter* **21**, 395502 (2009).

[69] **P. Giannozzi et al.** Advanced capabilities for materials modelling with QUANTUM ESPRESSO. *J. Phys.: Condens. Matter* **29**, 465901 (2017).

[70] **A. Marini, C. Hogan, M. Grüning, and D. Varsano** yambo: An *ab initio* tool for excited state calculations. *Comput. Phys. Comm.* **180**, 1392–1403 (2009).

[71] **D. Sangalli et al.** Many-body perturbation theory calculations using the yambo code. *J. Phys.: Condens. Matter* **31**, 325902 (2019).

[72] **C. A. Rozzi, D. Varsano, A. Marini, E. K. U. Gross, and A. Rubio** Exact Coulomb cutoff technique for supercell calculations. *Phys. Rev. B* **73**, 205119 (2006).

[73] **D. Y. Qiu, F. H. da Jornada, and S. G. Louie** Screening and many-body effects in two-dimensional crystals: Monolayer MoS_2. *Phys. Rev. B* **93**, 235435 (2016).

[74] **M. Rohlfing and S. G. Louie** Electron-hole excitations and optical spectra from first principles. *Phys. Rev. B* **62**, 4927–4944 (2000).

[75] **G. Strinati** Application of the Green's functions method to the study of the optical properties of semiconductors. *Riv. Nuovo Cimento* **11**, 1–86 (1988).

[76] **L. S. Blackford et al.** ScaLAPAC Users' Guide. *Society for Industrial and Applied Mathematics* (1997).

[77] **S. Balay et al.** PETSc Web page. (2025).

[78] **S. Balay et al.** PETSc/TAO Users Manual. *ANL-21/39 - Revision 3.23* (2025).

[79] **S. Balay, W. D. Gropp, L. C. McInnes, and B. F. Smith** Efficient Management of Parallelism in Object-Oriented Numerical Software Libraries. *Birkhäuser Boston* 163–202 (1997).

[80] **V. Hernandez, J. E. Roman, and V. Vidal** SLEPc: A scalable and flexible toolkit for the solution of eigenvalue problems. *ACM Trans. Math. Software* **31**, 351–362 (2005).

[81] **M. Drüppel, T. Deilmann, P. Krüger, and M. Rohlfing** Diversity of trion states and substrate effects in the optical properties of an MoS_2 monolayer. *Nat Commun* **8**, 2117 (2017).

[82] **T. Deilmann and K. S. Thygesen** Dark excitations in monolayer transition metal dichalcogenides. *Phys. Rev. B* **96**, 201113 (2017).

[83] **E. Courtade et al.** Charged excitons in monolayer WSe_2: Experiment and theory. *Phys. Rev. B* **96**, 085302 (2017).

[84] **A. M. Jones et al.** Excitonic luminescence upconversion in a two-dimensional semiconductor. *Nature Phys* **12**, 323–327 (2016).

[85] **Y. Ma, Q. Wang, S. Han, F. Qu, and J. Fu** Fine structure mediated magnetic response of trion valley polarization in monolayer WSe_2. *Phys. Rev. B* **104**, 195424 (2021).

[86] **Z. Li et al.** Revealing the biexciton and trion-exciton complexes in BN encapsulated WSe_2. *Nat Commun* **9**, 3719 (2018).

[87] **E. Liu et al.** Gate Tunable Dark Trions in Monolayer WSe_2. *Phys. Rev. Lett.* **123**, 027401 (2019).

[88] **T. P. Lyons et al.** The valley Zeeman effect in inter- and intra-valley trions in monolayer WSe_2. *Nat Commun* **10**, 2330 (2019).

[89] **L. Ren et al.** Measurement of the conduction band spin-orbit splitting in WSe_2 and WS_2 monolayers. *Phys. Rev. B* **107**, 245407 (2023).

[90] **A. K. Geim and I. V. Grigorieva** Van der Waals heterostructures. *Nature* **499**, 419–425 (2013).

[91] **C. Gong et al.** Band alignment of two-dimensional transition metal dichalcogenides: Application in tunnel field effect transistors. *Appl. Phys. Lett.* **103**, 053513 (2013).

[92] **J. Kang, S. Tongay, J. Zhou, J. Li, and J. Wu** Band offsets and heterostructures of two-dimensional semiconductors. *Appl. Phys. Lett.* **102**, 012111 (2013).

[93] **H.-P. Komsa and A. V. Krasheninnikov** Electronic structures and optical properties of realistic transition metal dichalcogenide heterostructures from first principles. *Phys. Rev. B* **88**, 085318 (2013).

[94] **A. Kormányos et al.** k·p theory for two-dimensional transition metal dichalcogenide semiconductors. *2D Mater.* **2**, 022001 (2015).

[95] **L. Debbichi, O. Eriksson, and S. Lebègue** Electronic structure of two-dimensional transition metal dichalcogenide bilayers from ab initio theory. *Phys. Rev. B* **89**, 205311 (2014).

[96] **R. Gillen and J. Maultzsch** Interlayer excitons in $MoSe_2$/WSe_2 heterostructures from first principles. *Phys. Rev. B* **97**, 165306 (2018).

[97] **M. Masseroni et al.** Gate-Tunable Band Edge in Few-Layer MoS_2. *Nano Lett.* **25**, 10472–10477 (2025).

[98] **J. Zhang et al.** Janus Monolayer Transition-Metal Dichalcogenides. *ACS Nano* **11**, 8192–8198 (2017).

[99] **A.-Y. Lu et al.** Janus monolayers of transition metal dichalcogenides. *Nature Nanotech* **12**, 744–749 (2017).

[100] **A. C. Riis-Jensen, T. Deilmann, T. Olsen, and K. S. Thygesen** Classifying the Electronic and Optical Properties of Janus Monolayers. *ACS Nano* **13**, 13354–13364 (2019).

[101] **Y.-C. Lin et al.** Low Energy Implantation into Transition-Metal Dichalcogenide Monolayers to Form Janus Structures. *ACS Nano* **14**, 3896–3906 (2020).

[102] **Y. Wang, W. Wei, B. Huang, and Y. Dai** The mirror asymmetry induced nontrivial properties of polar WSSe/MoSSe heterostructures. *J. Phys.: Condens. Matter* **31**, 125003 (2019).

[103] **A. Weston et al.** Atomic reconstruction in twisted bilayers of transition metal dichalcogenides. *Nature Nanotech* **15**, 592–597 (2020).

[104] **M. R. Rosenberger et al.** Twist Angle-Dependent Atomic Reconstruction and Moiré Patterns in Transition Metal Dichalcogenide Heterostructures. *ACS Nano* **14**, 4550–4558 (2020).

[105] **I. Maity, P. K. Maiti, H. R. Krishnamurthy, and M. Jain** Reconstruction of moiré lattices in twisted transition metal dichalcogenide bilayers. *Phys. Rev. B* **103**, L121102 (2021).

[106] **F. M. Arnold, A. Ghasemifard, A. Kuc, J. Kunstmann, and T. Heine** Relaxation effects in twisted bilayer molybdenum disulfide: structure, stability, and electronic properties. *2D Mater.* **10**, 045010 (2023).

[107] **W. Li, T. Brumme, and T. Heine** Relaxation effects in transition metal dichalcogenide bilayer heterostructures. *npj 2D Mater Appl* **8**, 43 (2024).

[108] **T. I. Andersen et al.** Excitons in a reconstructed moiré potential in twisted WSe_2/WSe_2 homobilayers. *Nat. Mater.* **20**, 480–487 (2021).

[109] **S. Kundu, T. Amit, H. R. Krishnamurthy, M. Jain, and S. Refaely-Abramson** Exciton fine structure in twisted transition metal dichalcogenide heterostructures. *npj Comput Mater* **9**, 186 (2023).

[110] **J. Hagel, S. Brem, J. A. Pineiro, and E. Malic** Impact of atomic reconstruction on optical spectra of twisted TMD homobilayers. *Phys. Rev. Mater.* **8**, 034001 (2024).